CHEMICAL REVIEWS

REVIEW

pubs.acs.org/CR

Hydrogen Storage in Metal−Organic Frameworks

Myunghyun Paik Suh,* Hye Jeong Park, Thazhe Kootteri Prasad, and Dae-Woon Lim

Department of Chemistry, Seoul National University, Republic of Korea

CONTENTS

1. INTRODUCTION

The decreasing fossil fuel supply and climate change caused by carbon dioxide emission have spurred an initiative to develop alternative fuels. Hydrogen is one of the most promising candidates for the replacement of current carbon-based energy sources. Hydrogen has an energy density much greater than gasoline and emits no carbon dioxide after burning. On a weight basis, hydrogen has nearly three times higher energy content than gasoline: lower heating values are 33.3 kWh kg^{-1} (123 MJ kg^{-1}) for hydrogen and 11.1 kWh kg^{-1} (47.2 MJ kg^{-1}) for gasoline, although on a volume basis the situation is reversed (8 MJ L^{-1} for liquid hydrogen versus 32 MJ L^{-1} for gasoline).

Free hydrogen does not occur naturally in quantity, and it should be generated from some other energy source by steam reformation of natural gas or other methods. Hydrogen is therefore an energy carrier (like electricity), not a primary energy source (like coal). For the advancement of hydrogen and fuel cell power technologies in transportation, stationary, and portable application, the research on hydrogen production, delivery, storage, and fuel cell technologies should be fully developed. Hydrogen storage is considered to be a key enabling technology.

In the case in which H_2 is used as a fuel in automobiles, 5−13 kg of H_2 would be consumed daily per ca. 300 miles driven. This implies a necessity to store a very large liquid or pressurized H_2 gas tank on board the vehicle. It would also require refilling everyday, which is neither safe nor practical. Therefore, the automobile and fuel cell industries have been searching for an efficient method to store and transport H_2. The U.S. Department of Energy (DOE) has set up the targets for on-board H_2 storage systems with the concept that higher efficiency fuel-cell power sources will replace current carbon-based energy source in future vehicles. The 2017 H_2 storage targets are 5.5 wt % in gravimetric capacity, 40 g L^{-1} of volumetric capacity at an operating temperature of −40−60 °C under a maximum delivery pressure of 100 atm. The targets are for a complete system, including tank, material, valves, regulators, piping, mounting brackets, insulation, added cooling capacity, and/or other balance-of-plant components.[1] None of the candidate materials developed so far has satisfied the DOE target yet.

Special Issue: 2012 Metal-Organic Frameworks

Received: July 22, 2011
Published: December 22, 2011

Wide ranges of materials have been tested as H_2 gas storage materials, which include metal hydrides,[2] complex hydrides,[3−6] chemical hydrides,[7−9] carbohydrates,[10] clathrates,[11] inorganic nanotubes,[12] organic materials,[13] sorbents such as metal-organic frameworks (MOFs) and carbon materials,[14−16] etc. There have been numerous reviews on the H_2 storage materials.[17−24] The main goal has been to find materials that adsorb hydrogen with H_2 density greater than the density of liquid H_2. The weight density of liquid hydrogen is as little as 70.8 kg m^{-3} at 20 K and atmospheric pressure, and 5 kg of H_2 occupies a fairly large volume of 56 m^3 under standard conditions.

There are various hydrogen storage materials. They can be divided into three categories based on the relative strength of the interaction of a storage material with hydrogen, which greatly affects the kinetics and thermodynamics of the hydrogen uptake and release: "physisorption materials", "on-board reversible hydrides", and "off-board regenerable hydrides" materials. In physisorbed hydrogen storage materials, H_2 molecules are adsorbed on the surface of the pores of the materials. According to IUPAC, physisorption (physical adsorption) is the adsorption in which the forces involved are intermolecular forces (van der Waals forces) of the same kind as those responsible for the imperfection of real gases and the condensation of vapors and which do not involve a significant change in the electronic orbital patterns of the species involved.[25,26] Physisorption processes are reversible since no activation energy is involved and the interaction energy is very low. In materials such as metal−organic frameworks, porous carbons, zeolites, clathrates, and organic polymers, H_2 is physisorbed on the surface of the pores. In these classes of materials, the H_2 storage capacity mainly depends on the surface area and pore volume. The main limitation of use of these sorbents as H_2 storage materials is weak van der Waals interaction energy between H_2 and the surface of the sorbents. Therefore, many of the physisorption based materials have high storage capacities at liquid nitrogen temperature and high pressures, but their capacities become very low at ambient temperature and pressure. Research is being directed toward the synthesis of highly porous materials that would have enhanced interaction energies with gaseous H_2. The positive side of these materials is the fast adsorption and desorption kinetics.

In chemisorption-based materials, hydrogen is chemically bonded to the storage medium. According the IUPAC, chemisorption (chemical adsorption) is the adsorption that results from chemical bond formation (strong interaction) between the adsorbent and the adsorbate in a monolayer on the surface.[27] The formation and stability of such materials highly depend on the pressure and temperature. Chemisorption process may not be reversible as relatively high activation energy exists in the adsorption and desorption process. On-board hydride materials and off-board regenerable hydride materials belong to this class.

On-board reversible hydride materials include interstitial metal hydrides, covalently bound metal hydrides, metal amides, borohydrides, etc. These store dissociated hydrogen either covalently or as interstitially bound hydrogen, and release hydrogen endothermically. The storage materials can be directly recharged with hydrogen in situ on a vehicle, since endothermic release allows for exothermic rehydrogenation during on-board recharging of the hydrogen storage materials under reasonable temperature and pressure (below 300 °C and below 200 bar). Interstitial metal hydrides are materials such as $LaNi_5H_x$. Covalent metal hydrides are discrete compounds such as MgH_2 and AlH_3, which have high gravimetric storage capacities, but the binding energies of these compounds are too weak or too strong to use as H_2 storage materials. Complex covalent hydrides are metal borohydrides and metal amides such as $LiBH_4$, $NaBH_4$, $Mg(BH_4)_2$, $LiNH_2$, and $Mg(NH_2)_2$. These have high gravimetric H_2 storage capacities but have the problem of high dehydrogenation temperature and irreversibility, and many catalysts are being tested for the use of such materials in reversible and moderate conditions.

Off-board regenerable hydride materials store dissociated hydrogen as covalently bound hydrogen materials, and they release hydrogen exothermically and/or involve complex off-board chemical processes for regeneration that cannot be performed on board a vehicle. Materials in this class are the hydrocarbons, ammonia borane, and alane. The hydrocarbons and alane release hydrogen endothermically, but high hydrogen pressures or the complexity of their rehydrogenation most likely will require an off-board process. Ammonia borane releases also a large amount of hydrogen rather exothermically, but it cannot be rehydrogenated readily at common pressures and temperatures.

As one of the promising hydrogen storage materials, MOFs have been extensively studied for the past decade. MOFs are crystalline materials consisting of metal ions linked together by organic ligands which generate micropores (<2 nm) and channels. Since MOFs are synthesized from metal ions and organic building blocks, the framework topology, pore size, and surface area can be readily tuned by the selection of molecular building blocks. MOFs generally have defined structures, permanent porosity, and high specific surface areas. Numerous MOFs with relatively small to very large surface areas have been reported. The highest excess H_2 storage capacity reported so far for MOFs is 99.5 mg g^{-1} at 56 bar and 77 K in NU-100 (NU = Northwestern University), which has a total capacity of 164 mg g^{-1} at 77 K and 70 bar.[28] The highest total H_2 storage capacity reported is 176 mg g^{-1} (excess 86 mg g^{-1}) in MOF-210 at 77 K and 80 bar.[29] These values are symbolic to the tremendous advancement in research on MOFs as H_2 storage materials. In 2003, the initial H_2 storage data were reported for MOF-5 (4.5 wt % at 77 K and 1 atm), which were prepared from benzene-1,4-dicarboxylate (BDC) and Zn(II) salt,[30] although it was found later that the maximum H_2 uptake varies from 1.3 to 5.2 excess wt % at 77 K depending on the preparation and handling conditions: Preparation and handling under N_2 atmosphere lead to H_2 uptake of excess 7.1 wt % at 77 K and 40 bar with total capacities of 10 wt % at 77 K and 100 bar, and 11.5 wt % at 77 K and 170 bar.[31] Since MOF-5 was reported, there have been numerous reports of porous MOFs, many of which have different framework topologies, and they showed relatively high H_2 storage capacities. Many researchers have employed various metal ions such as Zn(II), Cu(II), Mn(II), Cr(III), and lanthanides(III), and diverse types of ligands such as carboxylates, imidazolates, triazolates, tetrazolates for the construction of the MOFs. In recent years, researchers have modified the MOFs to increase the H_2 storage capacities.

Despite significant progresses in design and modification strategies for MOFs, we still encounter many problems in the development of practically applicable MOFs. Here, we review the representative MOFs that have been developed for H_2 storage and discuss the problems and prospects of MOFs as a H_2 storage material. Since there have been many review papers already published on hydrogen storage in MOFs, readers can find information from them also.[32−39]

dx.doi.org/10.1021/cr200274s |Chem. Rev. 2012, 112, 782–835

2. DEFINITIONS AND TERMINOLOGIES USED FOR HYDROGEN STORAGE

2.1. Sorption and Desorption

Sorption is the nonspecific term that describes both adsorption and absorption. It is most often used when it is difficult or impossible to differentiate between adsorption and absorption or when both processes occur simultaneously. The reverse process of sorption is desorption. The sorption and desorption of the sorbate by the sorbent is a dynamic process.

2.2. Adsorption and Absorption

Adsorption is the enrichment or depletion of one or more components in an interfacial layer. Absorption occurs when the adsorbates are incorporated into the internal structure of the adsorbent. In absorption, the structure and/or the chemical nature of the absorbate and absorbent may be modified. Adsorption and absorption refer to the location of the sorbed species with respect to the sorbent, that is, surface and bulk, respectively.

2.3. Chemisorption and Physisorption

Chemisorption is a surface-specific phenomenon and occurs when the interaction force between a surface and an adsorbate is similar to that of chemical bonding in bulk compounds. Physisorption is restricted to adsorption and occurs when the forces involved are weak intermolecular forces of the same kind as those responsible for the nonideality of gases and the condensation of vapors. Weak intermolecular forces are also known as van der Waals forces. Physisorption does not involve a significant change in the electronic structure of the species involved. For a molecular adsorbate where no bond dissociation occurs, it is often difficult to draw a boundary in the energy landscape between strong physisorption and weak chemisorption. It is useful to make a distinction between molecular physisorption, in which the H−H bond in the gas phase is preserved in the sorbed state, and chemisorption, in which the H−H bond is broken during the sorption process. Chemisorption may occur only in a monolayer on a surface, whereas physisorption is usually accompanied by multilayer adsorption depending upon the temperature.

2.4. Langmuir Surface Area and BET Surface Area

According to IUPAC, the porous materials are classified by their pore sizes. Macroporous materials have a pore size larger than 500 Å, mesoporous materials have pore size in the range 20−500 Å, and microporous materials have a pore size less than 20 Å. The microporous materials can be classified into two classes, ultramicroporous (smaller than 7 Å) and supermicroporous (7−20 Å) materials. The adsorption of gases on these materials has different mechanisms. Most MOFs reported so far fall in the category of microporous materials. The ultramicropores are filled at very low relative pressure (P/P_0), directed by gas−solid interactions and the rates of adsorption highly depend on temperature. In supermicropores, in addition to gas−solid interactions, a cooperation effect exists. Because of the cooperation effect, pore filling occurs at relatively lower relative pressure. Pore filling occurs when it is energetically as favorable for a gas molecule to exist between the monolayers of gas in the center of the pore as it is to complete monolayer coverage.[40,41]

The Langmuir equation is generally applied to materials having uniform surfaces that form only a monolayer with the adsorbates. Most MOFs have different types of atomic surfaces, and the interactions with gases highly depend on the metal atoms as well as organic linkers. At a very low pressure region, the initial adsorption takes place at the strongest sites of the surface, and as the pressure increases the adsorption takes place at weaker sites. In materials with multiple pores, the narrow pores are filled first and the larger pores are filled at slightly higher pressure. Because of the localized adsorption in ultramicroporous MOFs, and multilayer adsorption in supermicroporous MOFs, which is attributed to pore filling effect at very low relative pressure, the use of the Langmuir equation in the estimation of the surface area of MOFs may not provide accurate results.

BET theory takes into account multilayer adsorption. The BET equation is used universally for the calculation of surface area as a standard method because of its simplicity. Recently, it has been shown that BET surface area calculated from the N_2 adsorption isotherm obtained by the Grand Canonical Monte Carlo (GCMC) simulation is very similar to the experimental BET surface area.[42] Care must be taken in using the BET equation to determine the surface area of the MOFs since the calculated surface area of the framework depends on the pressure range used in the calculation.[43]

The specific surface areas of MOFs are generally determined from the N_2 adsorption isotherms at 77 K. It is common to use the Langmuir or BET equation to calculate the surface area of MOFs. In almost all cases, the surface area calculated by the Langmuir equation is much larger than that by the BET equation. The Langmuir surface area reported for MOF-200 is 10400 $m^2 g^{-1}$ and the corresponding BET surface area is 4530 $m^2 g^{-1}$.[29] MOF-210 has a Langmuir surface area of 10400 $m^2 g^{-1}$ and BET surface of 6240 $m^2 g^{-1}$. MOF-205 has a Langmuir surface area of 6170 $m^2 g^{-1}$ and BET surface area of 4460 $m^2 g^{-1}$.[29] For MOF-200 and MOF-210, the reported crystal density was 0.25 g cm^{-3}, which is one of the lowest for MOFs. MOF-205 has a crystal density of 0.38 g cm^{-3}. It has been found that the MOFs with a larger crystal density show a smaller difference between the Langmuir and BET surface areas. The results suggest that as the void volume increases, the difference in the Langmuir and BET surface areas increases.

2.5. Excess and Total Adsorptions of Hydrogen

The high pressure H_2 uptakes are generally represented as excess and total adsorption amount. The excess adsorption, which is also known as the Gibbs excess, is the difference in the amounts of gas phase H_2 that would be present in the equivalent volume of the adsorbed phase in the presence and absence of adsorption.[44] The excess adsorption reaches saturation at high pressure and then decreases as the hydrogen gas density increases further, due to the incompressibility of H_2 gas in the pores. In general, for the H_2 adsorption capacity up to 1 bar, the excess and total adsorption amounts are nearly identical. However, for H_2 adsorption capacity at high pressure, the absolute amount of H_2 gas per unit volume of MOF also contains pressurized gas in the pores of MOFs, which are not adsorbed on the surface. The total amount can be derived from the excess adsorption isotherms and the total skeletal volume of the framework, which can be obtained from the He gas sorption isotherm.[31]

The total amount of adsorbed gas is expressed as follows.[45−47]

$$N_{tot} = N_{ex} + d_{gas} V_{pore} \quad (1)$$

where N_{tot} is the total adsorption in mg g^{-1}, N_{ex} is the excess adsorption in mg g^{-1} that is the quantity being measured, d_{gas} is

dx.doi.org/10.1021/cr200274s |Chem. Rev. 2012, 112, 782–835

the compressed gas at a given temperature and pressure in g cm^{-3},

$$V_{\text{pore}} = \frac{1}{d_{\text{bulk}}} - \frac{1}{d_{\text{skeletal}}} \quad (2)$$

where V_{pore} is the pore volume in cm^3 g^{-1}, d_{bulk} is the crystallographic density of the sample, and d_{skeletal} is the skeletal density of the material.

$$d_{\text{skeletal}} = m/V_{\text{skeletal}} \quad (3)$$

where m is the sample mass expressed in g, and V_{skeletal} is the sample volume in cm^3, which is determined by using He expansion measured at 298 K up to 100 bar.

Generally, H_2 adsorption capacities in MOFs are represented in wt %, which can be expressed as (mass of H_2)/(mass of sample + mass of H_2). However, many researchers have omitted the term (mass of H_2) in the denominator, which should be avoided. For MOFs with low adsorption capacities, the omission of the term in the denominator may not make a difference, but as the H_2 adsorption capacity increases, it leads to overestimated wt %. Therefore, it is safe to use mg g^{-1} (mass in mg of H_2 adsorbed per gram of MOF) as a unit for the H_2 uptake capacity, and we encourage the use of mg g^{-1} instead of wt %.

2.6. Isosteric Heat of the Hydrogen Adsorption

The interaction enthalpy between a MOF and H_2 molecule, the isosteric heat (Q_{st}) of hydrogen adsorption, can be calculated from the H_2 adsorption isotherms measured at two independent temperatures, usually 77 and 87 K by fitting the data to virial equation or the Langmuir−Freundlich equation. The calculation provides the isosteric heat of H_2 adsorption depending on the adsorbed amounts of H_2, even though it cannot give information about the position and the number of H_2 adsorption sites. The zero-coverage isosteric heat corresponds to the interaction energy between the H_2 molecule and the strongest interaction site of the MOF.

Three different methods have been used for estimating the isosteric heat of the H_2 adsorption.

Method 1. The virial-type equation (eq 4) is used to fit the gas sorption data, which is composed of parameters a_i and b_i that are independent of temperature.[48,49] In eq 4, P is pressure, N is the amount adsorbed H_2 gas, T is temperature, and m and n represent the number of coefficients required to adequately describe the isotherms. Adsorption isotherms measured at two different temperatures are fit to the equation by using the statistical programs such as R statistical software package.[50] To estimate the values of the isosteric heat of H_2 adsorption, eq 5 is applied, where R is the universal gas constant.

$$\ln P = \ln N + \frac{1}{T}\sum_{i=0}^{m} a_i N^i + \sum_{i=0}^{m} b_i N^i \quad (4)$$

$$Q_{\text{st}} = -R\sum_{i=0}^{m} a_i N^i \quad (5)$$

Method 2. The following virial-type equation[51] (eq 6) is used to fit the adsorption data at a fixed temperature.

$$\ln(N/P) = A_0 + A_1 N + A_2 N^2 + A_3 N^3 + \cdots \quad (6)$$

In eq 6, P is pressure, N is amount of adsorbed gas, and A_0, A_1, etc. are virial coefficients. A_0 is related to the adsorbate−adsorbent interactions, whereas A_1 describes adsorbate−adsorbate interactions. Q_{st} for H_2 adsorption is calculated as a function of surface coverage by using Clausius−Clapeyron equation (eq 7), where R is the gas constant.

$$Q_{\text{st}} = R\ln\left(\frac{P_1}{P_2}\right)\frac{T_1 T_2}{T_2 - T_1} \quad (7)$$

Method 3. Langmuir−Freundlich equation[52] (eq 8) is used to fit the adsorption data at a fixed temperature. In eq 8, N is amount of adsorbed gas, N_m is amount of adsorbed gas at saturation, P is pressure, and B and t are the constants.

$$\frac{N}{N_m} = \frac{BP^{(1/t)}}{1 + BP^{(1/t)}} \quad (8)$$

The Langmuir−Freundlich equation can be rearranged to eq 9, and the isosteric heat of H_2 adsorption is obtained by using eq 7.

$$P = \left(\frac{N/N_m}{B + BN/N_m}\right) \quad (9)$$

We have to note that there are potential pitfalls in using each of the different types of fitting routines for deriving the isosteric heat of H_2 adsorption. Methods 1 and 2 allow a series of Q_{st} values to be obtained as a function of n. Minimal deviations are observed for all experimental points measured over a wide range of pressure. The most salient feature of these virial equations is that they would allow extrapolation to zero coverage of H_2, therefore allowing the determination of this value at zero coverage. However, the Langmuir−Freundlich (or other semiempirical routines) method results in gross overestimation of the adsorption enthalpy if extrapolation is made down to zero coverage, since this approach does not reduce to Henry's Law and leads to the largest error at zero coverage. This overestimation is in fact responsible for many high adsorption enthalpy values reported in the literature. On the other hand, fits using the virial equation can be overinterpreted if polynomials of too high order are used indiscriminately. The important value in that case is that of the lowest order polynomial coefficient. If a standard deviation in that fit is too large, the fit value is meaningless. However, this fact is unfortunately often disregarded by researchers in the field. Despite this, virial analysis is better and more mathematically consistent since it reduces to Henry's Law, although it gives lower values of the heat of adsorption.

3. DESIGN AND SYNTHESIS OF METAL−ORGANIC FRAMEWORKS FOR HYDROGEN STORAGE

MOFs have been successfully synthesized from solvothermal reactions with metal and organic building blocks in organic solvents, in particular, those that have high boiling points such as DMF and DEF, generally at 80−130 °C. In general, the high temperature reaction conditions of solvothermal syntheses eliminate the solubility restrictions for the reagents. Mixed solvents are sometimes used to control the solution polarity, solvent−ligand exchange kinetics, and rate of product crystallization. For example, to aid crystallization during synthesis, low boiling solvents such as ethanol and acetonitrile can be added.

MOFs can be constructed by various combinations of metal ions and ligands. Sometimes two different metal ions and a ligand are reacted to obtain new MOFs that contain two kinds of metal ions.[53,54] A metal ion can also be reacted with two different ligands.[29,55−57] Although the framework structure of a MOF mainly depends on the metal and organic building blocks, it can

dx.doi.org/10.1021/cr200274s |Chem. Rev. 2012, 112, 782–835

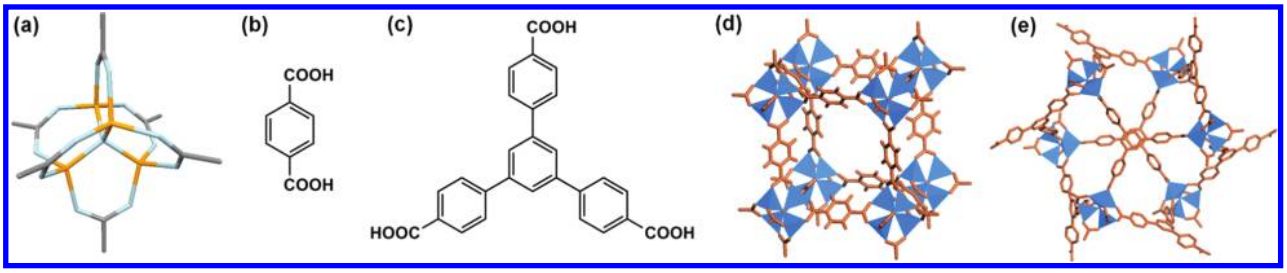

Figure 1. (a) $[Zn_4O]$ SBU. The carboxylic acid used in the synthesis of (b) MOF-5 and (c) MOF-177. The structures of (d) MOF-5 and (e) MOF-177.

also depend on the type of solvent, reaction temperature, and rate of crystal growth. If a solvent is included in the pores or coordinated at the metal ion of the framework, the type of solvent can completely change the framework structure. Subsequently, the properties of a MOF, such as gas sorption and guest recognition, depend on its structure, in particular, the size and shape of the pores and the chemical environment of the pore surface.

The most common metal ions used in the synthesis of MOFs are Zn(II) and Cu(II), but other transition metal ions such as those in the first transition series may be employed as metal building blocks. Various carboxylic acids as well as heterocyclic compounds containing nitrogen donors are used as the organic building blocks for the construction of MOFs. The excellent review by O'Keeffe and Yaghi has shown various possible topologies of MOFs that are constructed from metal and organic building blocks.[58]

3.1. Carboxylate-Based MOFs

MOFs can be synthesized by the solvothermal reaction of metal ions and various carboxylic acids. The network topology is established by the metal-carboxylate subunits as nodes and the organic linkers as struts. The great variety of organic ligands and metal ions that are employed in the synthesis provides a wide range of networks with various pore sizes and metal centers. The use of rigid organic carboxylates ligands in the synthesis of MOFs often leads to porous frameworks with exceptional robustness, and many of these MOFs do not collapse even after the removal of the guest solvent molecules that are incorporated during the synthesis. Various metal sources have been utilized in the synthesis of MOFs, such as Zn, Cu, Mn, Co, Cr, Ni, lanthanide metals, alkali metals, Mg, and Al, and the structures and properties of those MOFs have been reported. The hydrogen adsorption capacity slightly depends on the type of metal ion but is more generally correlated with the surface area and pore volume of the framework. The chemical or electronic environment of the pore surface is also important, modified by the presence of functional groups in the ligand and/or at the vacant coordination sites on metal ions. Some MOFs, in particular, Zn-carboxylate based MOFs, are known to be air-sensitive, with hydrogen gas sorption capacities decreasing upon exposure to air. This is most likely due to the degradation of the frameworks, and thus proper handling of the Zn-MOFs is required.[31]

MOFs synthesized from carboxylate ligands are among most commonly reported. Dicarboxylic acids, especially, have been extensively used in various syntheses. Since MOF-5 was synthesized from the solvothermal reaction of a Zn^{II} salt and 1,4-benzenedicarboxylic acid (BDC) in DEF,[59] a series of isoreticular MOFs (IRMOF) were prepared using various dicarboxylic acids.[60−62] The IRMOF series have cubic framework structures that generate varying size 3D channels. In their structures, $[Zn_4O]$ clusters were formed as the octahedral secondary building units (SBUs), which are connected with six carboxylate linkers to form a cubic network. The pore size and the surface area in the series were efficiently controlled by adjusting the length of the dicarboxylic acid and by the introduction of functional groups on the aromatic ring. Most of the IRMOFs showed high surface areas and large pore volumes. MOF-5 (IRMOF-1) has a BET surface area of 3800 $m^2\ g^{-1}$ and adsorbs excess 7.1 wt % of H_2 at 40 bar and 77 K, and is still considered to be one of the best hydrogen storage materials.[31] Because of the high surface area and large pore volume of MOF-5, many studies have been done on MOF-5, such as incorporation of various metal nanoparticles,[63−66] chromatography with a single crystal of MOF-5,[67] utilization as a template for porous carbon synthesis,[68] hydrogen spillover study,[69] etc. For example, in such a study, $Cr(CO)_3$ species were attached to the BDC rings of MOF-5 via postsynthetic modification. After the formation of piano stool complexes, the framework was still stable, crystalline, and microporous.[70]

MOFs constructed from $[Zn_4O]$ SBUs and tricarboxylate ligands are also very common and possess very high surface areas and large pore volumes. The well-known MOF-177 is constructed from $[Zn_4O]$ clusters and 4,4′,4″-benzene-1,3,5-triyl-tribenzoate (BTB), where each $[Zn_4O]$ unit is connected to six carboxylate groups and each tricarboxylate ligand connects to three $[Zn_4O]$ units to form a (6,3) connected net (Figure 1). MOF-177 has a BET surface area of 4750 $m^2\ g^{-1}$ and a pore volume of 1.59 $cm^3\ g^{-1}$, making it one of the most porous MOFs.[62,71] The compound adsorbs 7.5 wt % of H_2 at 77 K and 70 bar.[62] After the discovery of MOF-177, many highly porous MOFs having (6,3) net structures have been reported, and most of them show high surface areas. For example, MOF-200, which was constructed from $[Zn_4O]$ cluster and 4,4′,4″-[benzene-1,3,5-triyl-tris(benzene-4,1-diyl)]tribenzoate (BBC) has a BET surface area of 4530 $m^2\ g^{-1}$.[29]

Many other MOFs that are constructed of $[Zn_4O]$ octahedral SBUs and polycarboxylates were also reported, such as UMCM-2, MOF-205, and MOF-210, which are mesoporous materials.[29,72] These mesoporous materials might be useful for hydrogen storage after modification of the pores to enhance the interaction between hydrogen and the framework.

MOFs synthesized from copper and carboxylic acids are an interesting class of MOFs since they generally consist of a paddle-wheel type $[Cu_2(OOC)_4]$ SBU and a carboxylate linker (Figure 2). The typical MOF formed from a Cu(II) paddle-wheel SBU and BTC is HKUST-1, which shows a Langmuir surface of 917.6 $m^2\ g^{-1}$.[73] In paddle-wheel type SBUs, the axial positions are normally occupied by coordinated solvent molecules, which can be easily removed by heating and/or evacuation without destroying

dx.doi.org/10.1021/cr200274s |*Chem. Rev.* 2012, 112, 782–835

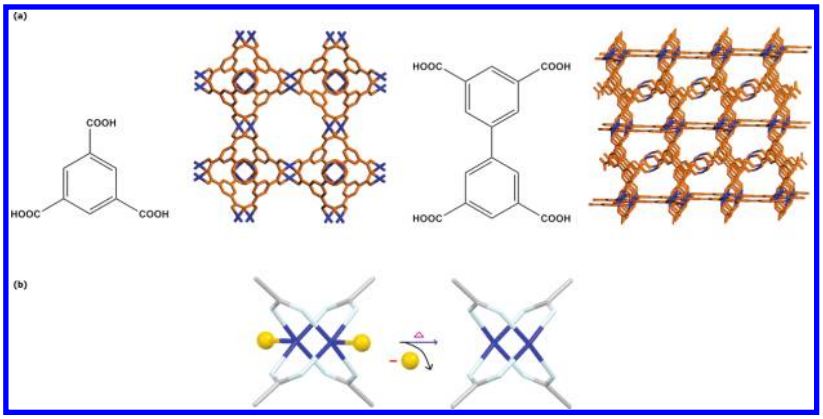

Figure 2. (a) The carboxylic acids employed in the synthesis of porous MOFs with open metal sites and respective networks. (b) Creation of open metal sites at the paddle-wheel SBU in a MOF by removal of coordinated solvent molecules.

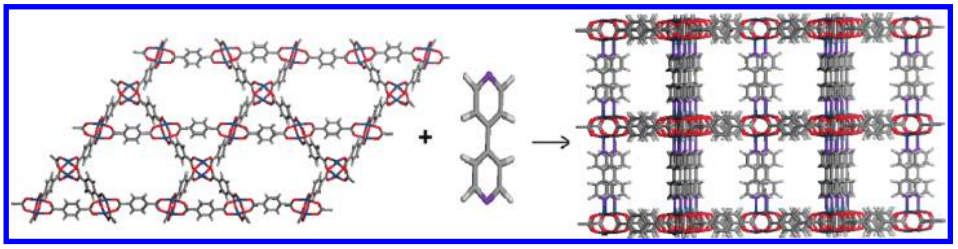

Figure 3. Schematic diagram showing the construction of a 3D MOF from the 2D layer formed of paddle-wheel SBUs and the second pillaring ligand. Color scheme: Zn, blue; O, red; N, violet; C, gray; H, light gray.

the framework structure, thus leading to the formation of open metal sites. MOFs with open metal sites generally provide high surface areas due to the reduction of framework mass as well as the stronger interaction between the metal sites and gas molecules, and thus generally adsorb higher amounts of H_2 gas.[74,75] A comparison of the H_2 gas sorption properties of MOFs having the same framework structures, in the presence and absence of the open metal sites, has also been reported.[76] In the presence of open metal sites, the MOF showed higher H_2 gas uptake capacities, mainly due to the mass reduction effect, but the H_2 gas capacities per volume of MOF samples were also higher (10−20%) than those without open metal sites.

As previously mentioned, MOFs made from $[Zn_2(OOC)_4]$ paddle-wheel SBUs often coordinate solvent molecules at the axial sites of the Zn ion, which can be removed by activation to generate open metal sites.[76] Furthermore, when two-dimensional (2D) networks constructed of dicarboxylate and square paddle-wheel units are connected with a second ligand, such as 4,4′-bipyridine (4,4′-bpy) or 3,6-di(4-pyridyl)-1,2,4,5-tetrazine (bpta), a 3D network can be constructed (Figure 3).[56,57,77−81] Many of these frameworks are interpenetrated and often show selectivity toward adsorption of the gases due to the molecular sieving effect of their pore sizes.

The representative MIL (MIL: material from Institute Lavoisier) series are constructed of trimeric chromium(III) octahedral cluster units and di- or tricarboxylates.[82−84] Many of the MIL frameworks are highly porous, and show high thermal and chemical stability. For example, MIL-101 adsorbs 6.1 wt % of H_2 at 77 K and 80 bar. The isosteric heat of H_2 adsorption is 10 kJ mol^{-1} at low H_2 loading. Many other highly porous materials have also been prepared from other metal ions such as In(III),[85−87] Co(II),[88,89] Mg(II),[90−92] Ni(II)[93] and have different structures and relatively high H_2 uptake capacities.

It must be emphasized that in the synthesis of carboxylate MOFs, the solvent system often greatly affects the structure of the MOF, which consequently affects the gas sorption properties. For example, Suh et al. prepared a porous MOF, $[Zn_4O(NTB)_2]_n \cdot 3nDEF\cdot n$EtOH, by using $Zn(NO_3)_2 \cdot 6H_2O$ and H_3NTB (4,4′,4″-nitrilotrisbenzoic acid) in a DEF, EtOH, and H_2O mixture.[94] In the structure, the $Zn_4O(CO_2)_6$ octahedral SBUs are linked by the NTB^{3-} units to form PdF_2 type (3,6)-connected nets, which are doubly interpenetrated to generate curved 3D channels (Figure 4). The compound maintained the single crystal nature even after removal of guest solvent molecules, and the desolvated framework $[Zn_4O(NTB)_2]_n$ exhibited permanent porosity, high thermal stability, blue luminescence, and high N_2, H_2, CO_2, and CH_4 gas storage capacities. In particular, it showed H_2 uptake capacity of 1.9 wt % at 77 K and 1 atm. When a similar solvothermal synthesis was carried out at 110 °C in a different solvent system consisting only of EtOH, a 3D network $[Zn_3(NTB)_2(EtOH)_2]_n \cdot 4n$EtOH was produced, which generated one-dimensional (1D) channels of honeycomb aperture.[95] On activation, the compound released the coordinating EtOH as well as guest EtOH molecules to result in the desolvated sample $[Zn_3(NTB)_2]_n$, which maintained the single crystallinity and showed H_2 uptake capacity of 1.0 wt % at 77 K and 1 atm.

3.2. Azolate-Based MOFs

Heterocyclic ligands such as imidazole, pyrazole, triazole, and tetrazole have been used in the synthesis of porous MOFs. The pK_a values of imidazole, pyrazole, triazole, and tetrazole are about 14.5, 14.2, 9.3, and 4.9, respectively.

Zeolitic imidazole frameworks (ZIFs) form neutral networks from the tetrahedrally coordinated zinc or cobalt centers and imidazolate linkers (Figure 5). The bridging angle of M−IM−M (IM = imidazolate) is similar to that of Si−O−Si angle in zeolites. These classes of compounds having zeolitic topology

dx.doi.org/10.1021/cr200274s |*Chem. Rev.* 2012, 112, 782–835

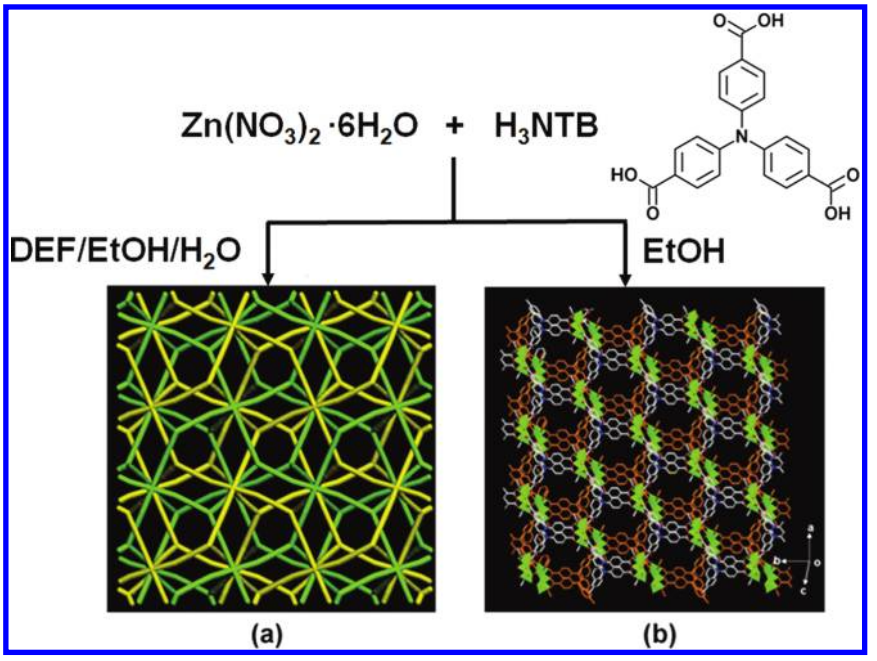

Figure 4. Two different frameworks formed from Zn(II) and NTB^{3-} in the different solvent systems. (a) A doubly interpenetrated PdF_2 structure of $[Zn_4O(NTB)_2]_n \cdot 3nDEF\cdot n$EtOH produced from DEF/EtOH/H_2O (5:3:2, v/v) mixture.[94] (b) The framework structure of $[Zn_3(NTB)_2(EtOH)_2]_n \cdot 4n$EtOH produced from EtOH.[95]

have high chemical and thermal stability. The structures of various ZIFs have been well documented,[96−99] and their gas storage properties have been reported.[100−103]

The H_2 storage capacities of several ZIFs have been reported. $Zn(MeIM)_2$ (ZIF-8) adsorbs 3.3 wt % of H_2 at 77 K and 30 bar, which is the highest H_2 adsorption capacity reported to date for ZIFs, indicating that ZIFs likely cannot be better H_2 storage materials than the carboxylate based MOFs. A recent review provides a detailed description of zeolitic imidazolate frameworks.[104]

Long and co-workers have reported a synthesis of Co(BDP)·2DEF·H_2O from the reaction of Co(II) ion and 1,4-benzenedi(4′-pyrazolyl) (BDP), which shows a high Langmuir surface area (2670 $m^2\ g^{-1}$) and a stepwise N_2 adsorption. It shows excess H_2 uptake capacities of 5.5 wt % at 10 bar and 50 K, and 3.1 wt % at 30 bar and 77 K.[105]

Triazolate-based MOFs are analogous to carboxylate-based MOFs with respect to their gas sorption properties. Triazole generally has a low pK_a value of about 9.3 and has different types of coordination modes depending on the degree of deprotonation. Gamez et al. provides a nice review on the triazoles, tetrazoles, and their possible coordination modes (Figure 6).[106] There are two different types of triazoles depending on the position of N on the ring, 1,2,3-triazole and 1,2,4-triazole.

Recently, Long and co-workers reported a triazolate-based framework $H_3[(Cu_4Cl)_3(BTTri)_8]$ (BTTri = 1,3,5-tris(1H-1,2,3-triazol-5-yl)benzene). The activated framework has exposed Cu^{2+} sites and shows a BET surface area of 1770 $m^2\ g^{-1}$ and a H_2 uptake capacity of 1.2 wt % at 1.2 bar and 77 K.[107] Most importantly, triazolate-based frameworks are stable in air, boiling water, and even acidic media. The framework FMOF-1 with the formula $\{Ag_2[Ag_4Tz_6]\}_n$ was synthesized from Ag(I) and 3,5-bis(trifluoromethyl)-1,2,4-triazolate and showed hysteretic

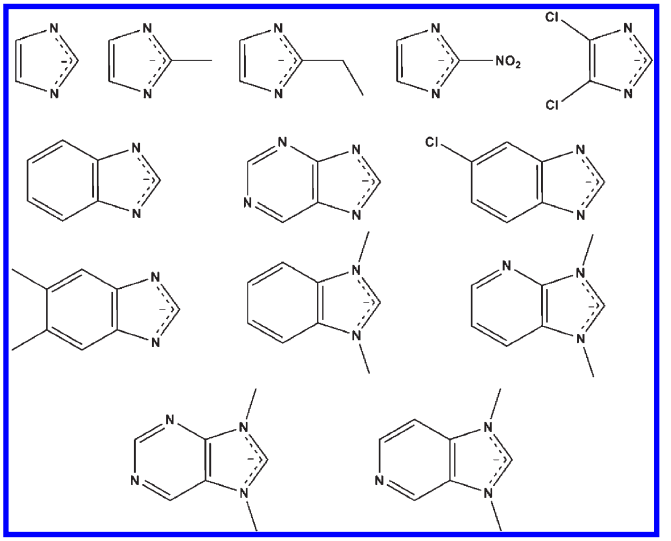

Figure 5. Various ligands used in the synthesis of zeolitic imidazolate frameworks.

adsorption of H_2 with a volumetric capacity of 41 kg m^{-3} at 77 K and 64 bar due to the fluoro-lined channels and cavities of the triazole framework.[108] In addition to the frameworks referred to here, many other porous triazolate-based frameworks exist.[109−111]

The tetrazolates are similar to carboxylic acids with respect to ligand acidity and planarity, and the tetrazole ring has a pK_a value of about 4.9. The presence of multiple N atoms gives rise to various types of coordination (Figures 7 and 8), which leads to the formation of a wide range of porous structures. There are many reports of tetrazolate-based MOFs,[48,112] a few of which

dx.doi.org/10.1021/cr200274s |*Chem. Rev.* 2012, 112, 782–835

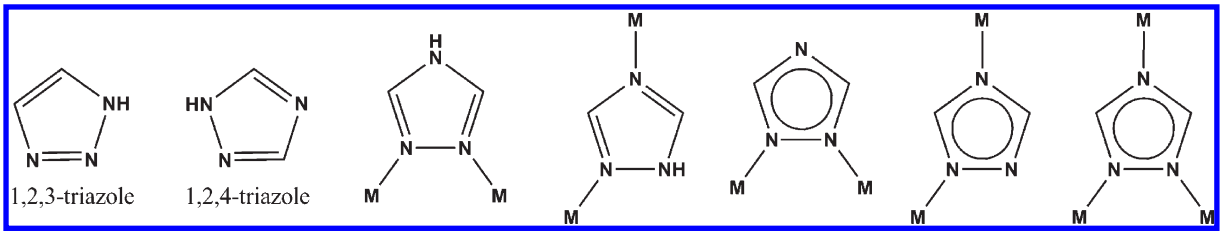

Figure 6. 1,2,3-Triazole, 1,2,4-triazole, and the coordination modes of 1,2,4-triazole and 1,2,4-triazolate.

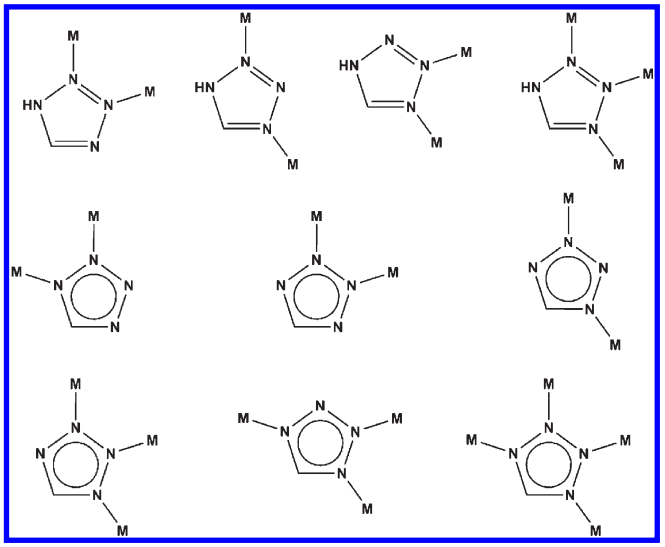

Figure 7. Coordination modes of tetrazole and tetrazolate.

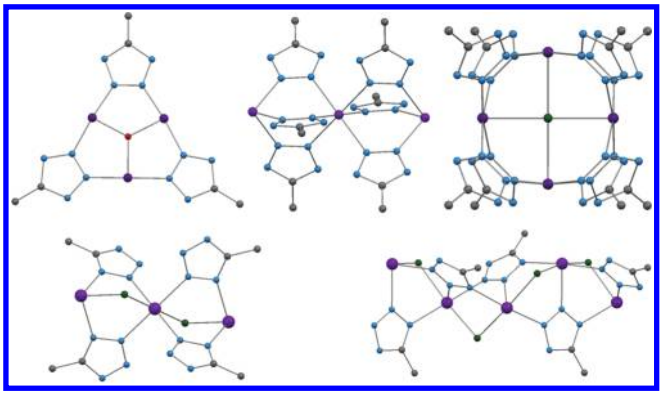

Figure 8. Various types of tetrazolate cluster units found in tetrazolate-based MOFs. Color code: violet, metal; green, Cl; red, O; blue, N; gray, C.

contain open metals sites. Dincă and Long reported the synthesis and gas sorption properties of $Mn_3[(Mn_4Cl)_3(BTT)_8(CH_3OH)_{10}]_2$ (BTT = 1,3,5-benzenetristetrazolate), which showed a total H_2 uptake capacity of 6.9 wt % at 77 K and 90 bar and zero coverage isosteric heat of H_2 adsorption of 10.1 kJ mol^{-1}.[48] Neutron powder diffraction (NPD) data showed that H_2 molecules were directly bound to unsaturated Mn^{2+} centers within the framework. The guest Mn^{2+} ions in the framework can be exchanged with various cations such as Li^+, Cu^+, Fe^{2+}, Co^{2+}, Ni^{2+}, Cu^{2+}, and Zn^{2+}, and all of them are porous, showing relatively high H_2 uptakes ranging from 2.00 to 2.29 wt % at 77 K and 900 Torr.[112] The Co^{2+}-exchanged compound has zero coverage isosteric heat of 10.5 kJ mol^{-1}, which is slightly greater than that of the original sample. The reactions of Cu(II) and two similar tetrazole ligands, 1,3,5-tri-*p*-(tetrazol-5-yl)phenylbenzene (H_3TPB-3tz) and 2,4,6-tri-*p*-(tetrazol-5-yl)phenyl-*s*-triazine (H_3TPT-3tz), lead to the formation of noncatenated and catenated sodalite-type MOFs. The catenated framework shows relatively high stability toward desolvation and shows higher surface area and H_2 uptake. The total hydrogen uptake capacity of the catenated framework is 4.5 wt % at 80 bar and 77 K.[113] There are few other reports for the tetrazolate-based frameworks that show moderate H_2 uptake capacities ranging from 0.82 to 1.46 wt %.[114]

3.3. MOFs with Mixed Ligands

Porous MOFs that contain two different organic ligands within the same framework or those constructed of a ligand that contains two different coordinating functional groups can be synthesized. The most common and well-known MOFs constructed from the combination of two different ligands are the 3D primitive cubic-type (α-Po) structures (Figure 9). In these MOFs, 2D layers are assembled from paddle-wheel cluster units $[M_2(O_2CR)_4]$ (M = Cu^{2+}, Zn^{2+}, and Co^{2+}) and dicarboxylate linkers. The 2D layers are linked with pillars to form 3D MOFs. The pore size and pore environment of these pillared square grid nets can be simply tuned by selecting the different combinations of dicarboxylates and pillar linkers. For example, Kim and co-workers reported the X-ray structures and gas sorption properties of a series of isomorphous MOFs that were systematically modulated from a prototype $[Zn_2(1,4\text{-bdc})_2(dabco)]$ by replacing 1,4-bdc with dicarboxylate linkers having aliphatic (tetramethylterephthalate, tmbdc), aromatic (1,4-naphthalenedicarboxylate, 1,4-ndc), or halogenic (tetrafluoroterephthalate, tfbdc) side groups on the phenyl ring of the ligands, and substituting 1,4-diazabicyclo[2.2.2]octane (dabco) with longer 4,4′-bpy.[115] Introduction of substituents on the phenyl ring of 1,4-bdc resulted in a significant decrease in the surface area. The H_2 adsorption isotherms showed similar uptake capacities, but the curves showed markedly different slopes in the low pressure ranges (P < 0.4 atm). The framework with the most crowded pore environment showed the fastest rise in H_2 uptake, indicating the highest affinity toward H_2 at low pressures. The authors proposed that a porous material with a surface area greater than 2000 $m^2 g^{-1}$, a void fraction greater than 60%, and free window sizes smaller than 6 Å might exhibit an excellent H_2 storage capacity.

When longer ligands were used in the construction of the primitive cubic net, multiply interpenetrated frameworks often resulted. Some of these multiply interpenetrating MOFs exhibit unusual stepwise gas adsorption and hysteretic desorption behavior due to the changes in the framework structures. Suh et al. reported a doubly interpenetrated (α-Po) net with 3D curved

dx.doi.org/10.1021/cr200274s |*Chem. Rev.* 2012, 112, 782–835

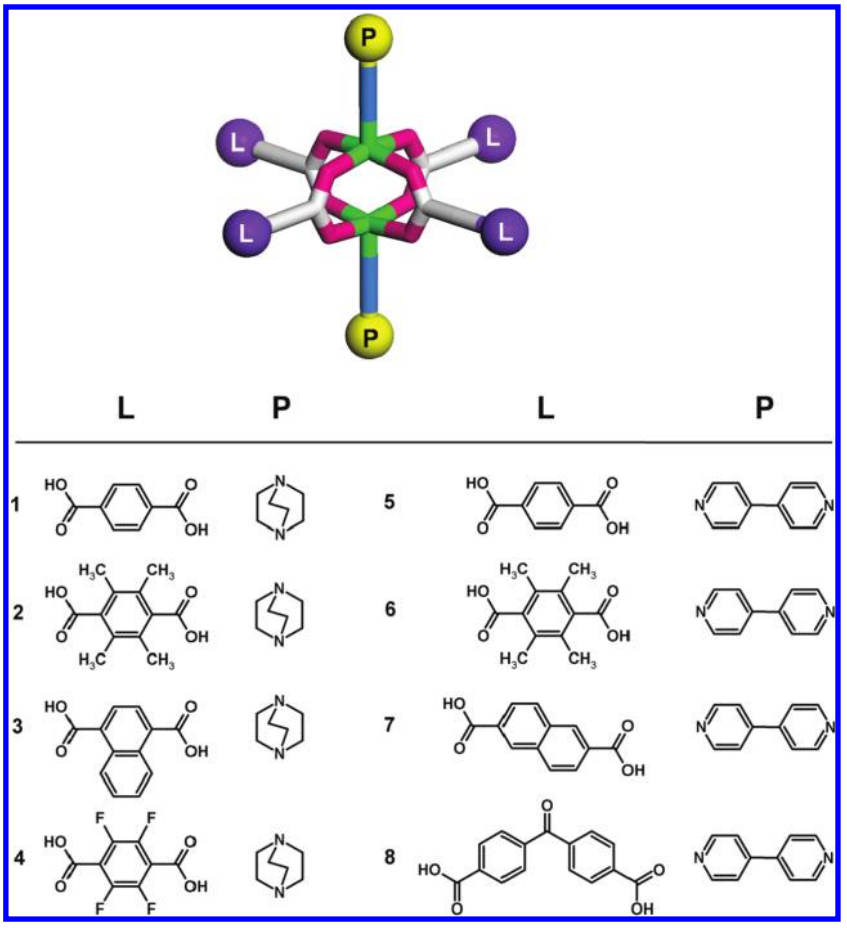

Figure 9. Linkers (L) and pillars (P) employed in the synthesis of 3D primitive cubic-type (α-Po) structures.

channels, $[Zn_2(BPnDC)_2(bpy)]_n$ (SNU-9), where BPnDC is 4,4′-benzophenone dicarboxylate.[116] In SNU-9, every binuclear Zn_2 unit is bridged by BPnDC1 and 4,4′-bpy to form a distorted square grid 2D network that runs parallel to the *ab* plane, while BPnDC2 acts as a pillar linking the layers along the *c* axis, which gives rise to a 3D framework. SNU-9 showed a three-step adsorption for N_2 and O_2 gases, and two-step adsorption for CO_2 and H_2 gases with large hysteresis on desorption, while it does not uptake CH_4 gas. SNU-9 has a Langmuir surface area of 1030 $m^2\ g^{-1}$, pore volume of 0.366 $cm^3\ g^{-1}$, and high gas uptake capacities for H_2, CO_2, and O_2 gases.

As a new method to develop highly porous MOF, Matzger and co-workers suggested coordination copolymerization of topologically different linkers with identical coordinating functionality.[72,117,118] They combined symmetrical dicarboxylate and tricarboxylate, which should be connected with $[Zn_4O]$ octahedral SBUs. For example, $[Zn_4O(BDC)(BTB)_{4/3}]$ (UMCM-1, UMCM = University of Michigan crystalline material) was obtained from BDC and BTB.[117] On the octahedral building unit, two BDC linkers are adjacent and the other four positions are occupied by BTB linkers, which construct an octahedral cage. When ditopic linker BDC was replaced with thieno[3,2-b]thiophene-2,5-dicarboxylate (T^2DC), 2,5-thiophenedicarboxylate (TDC), and NDC, different coodination modes formed, which provided the frameworks with different topologies, UMCM-2, UMCM-3, and MOF-205, respectively. All MOFs (UMCM-1, -2, -3, -4, -5, MOF-205, and MOF-210) prepared by this technique demonstrated BET surface areas ranging from 3500 to 6240 $m^2\ g^{-1}$ and the high pore volumes ranging from 1.64 to 3.60 $cm^3\ g^{-1}$.[29,118] UMCM-2, $\{[Zn_4O(T^2DC)(BTB)_{4/3}]\}$, showed high H_2 uptake (excess 68.8 mg g^{-1}) at 77 K and 46 bar. MOF-210 constructed from 4,4′,4″-[benzene-1,3,5-triyl-tris(ethyne-2,1-diyl)]tribenzoate (BTE) and biphenyl-4,4′-dicarboxylate (BPDC) exhibited excess H_2 uptake of 86 mg g^{-1} at 77 K and 56 bar with a total uptake of 176 mg g^{-1} at 77 K and 80 bar. This total H_2 uptake is the highest and excess is the second after NU-100 among the data ever reported for physisorption materials.

The ligand having two different coordinating functional groups has been also employed in the synthesis of porous MOFs. The representative example is pyridyl carboxylic acid such as isonicotinic acid[119] and pyridinedicaboxylic acid (Figure 10).[120] Recently, Su and Eddaoudi groups independently suggested a new pillaring strategy based on a ligand-to-axial approach by combining two previous methods, axial-to-axial and ligand-to-ligand pillaring.[121,122] They used trigonal heterofunctional ligand that is a functionalized isophthalic acid with N-donor (pyridyl of triazolyl) at the 5-position. From trigonal ligands (3-connected) and the common 6-coordinated paddle-wheel $[Cu_2(COO)_4L_2]$ motifs, (3,6)-connected 3D MOFs have been synthesized.

Recently, Chen and co-workers reported a new approach to construct interpenetrated microporous MOFs having primitive cubic net structures, which were constructed from the combination of pyridylcarboxylate and dicarboxylate linkers with paddle-wheel units (Figure 11).[123] $[Zn_2(PBA)_2(BDC)]\cdot 3DMF\cdot 4H_2O$ (UTSA-36; UTSA = University of Texas at San Antonio) was constructed from 4-(4-pyridyl) benzoic acid (PBA) and BDC

dx.doi.org/10.1021/cr200274s |*Chem. Rev.* 2012, 112, 782–835

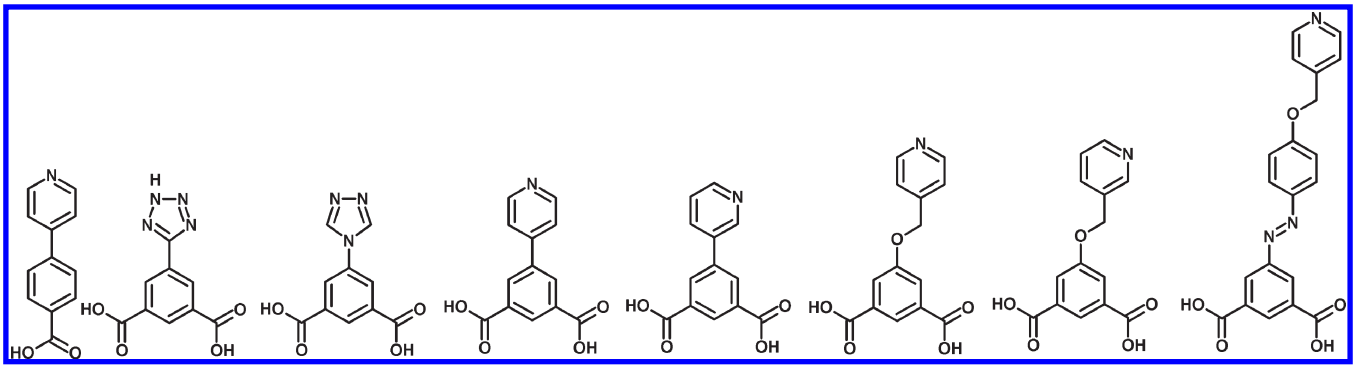

Figure 10. The ligands with two different functional groups.

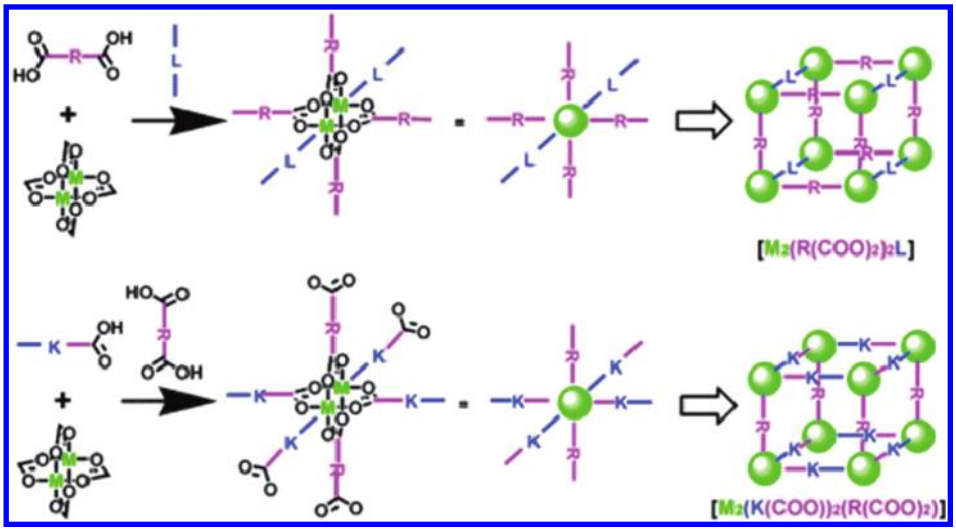

Figure 11. Two approaches for constructing the porous MOFs with primitive cubic net structure by using two different organic ligands. Reproduced with permission from ref 123. Copyright 2011 WILEY-VCH Verlag GmbH & Co. KGaA, Weinheim.

with a Zn salt. UTSA-36 is doubly interpenetrated to generate small pores of size 3.1−4.8 Å, which shows highly selective sorption of small hydrocarbons C_2H_2, C_2H_4, and C_2H_6 over CH_4. It has a Langmuir (BET) surface area of 806 $m^2\ g^{-1}$ (495 $m^2\ g^{-1}$), a pore volume of 0.33 $cm^3\ g^{-1}$, and a H_2 uptake of 123 $cm^3\ g^{-1}$ (1.1 wt %) at 77 K and 1 atm.

MOFs containing two different types of metal clusters can be also synthesized. Eddaoudi, Zaworotko, and co-workers reported $[Cu_6O(TZI)_3(H_2O)_9(NO_3)]$, which was constructed of two different Cu clusters and 5-tetrazolylisophthalic acid (TZI).[124] The X-ray crystal structure revealed isophthalates and tetrazolates formed $[Cu_2(O_2CR)_4]$ paddle-wheels units and trigonal $[Cu_3O(N_4CR)_3]$ trimers. The framework showed a Langmuir (BET) surface area of 3223 (2847) $m^2\ g^{-1}$, a total pore volume of 1.01 $cm^3\ g^{-1}$, high H_2 storage capacity (2.4 wt % at 77 K and 1 atm) with high isosteric heat of 9.5 kJ mol^{-1}.

3.4. MOFs with Metal Complexes as Building Blocks

3.4.1. MOFs Based on Macrocyclic Complexes. Another class of compounds that might find application in hydrogen storage is the frameworks constructed from square-planar Ni(II) macrocyclic complexes and organic ligands. When the square-planar macrocyclic complexes are reacted with various types of carboxylates, such as linear dicarboxylates, trigonal tricarboxylates, square-type or tetrahedral-shaped tetracarboxylates, the Ni(II) ions of the macrocyclic complex coordinate oxygen atoms of the carboxylate at the axial sites of the macrocyclic plane to yield electronically neutral 1D, 2D, and 3D networks, respectively.[125−133] In such networks, the carboxylate ligands are located at the nodes and the macrocyclic complexes are positioned at the struts since the macrocyclic complexes simply act as linear linkers to connect the organic ligands (Figure 12). The synthetic strategies are previously well reviewed.[125,126]

The advantage of Ni(II) macrocyclic complexes in the construction of MOFs is that they can form grooves in the structures, which induce fits between the networks and often lead to robust frameworks. Moreover, the networks constructed of Ni(II) macrocyclic complexes are redox active because the Ni(II) ion of the macrocyclic complex can be oxidized to Ni(III) species or reduced to Ni(I) species, which are stabilized by the macrocyclic effect despite of the uncommon oxidation state. By using such redox-active properties, Suh's group oxidized the crystal of the network by using I_2, which resulted in an oxidized framework containing I_3^- anions.[128] On the basis of this knowledge, Suh's group developed the fabrication method of Ag, Au, and Pd nanoparticles in the pores of the networks by simple immersion of the redox-active porous crystals in the solutions of Ag(I), Au(III), and Pd(II) salts, respectively.[130−132,134] The MOF loaded with palladium nanoparticles showed enhanced hydrogen uptakes at 77 K as well as at room temperature.[134]

dx.doi.org/10.1021/cr200274s |*Chem. Rev.* 2012, 112, 782–835

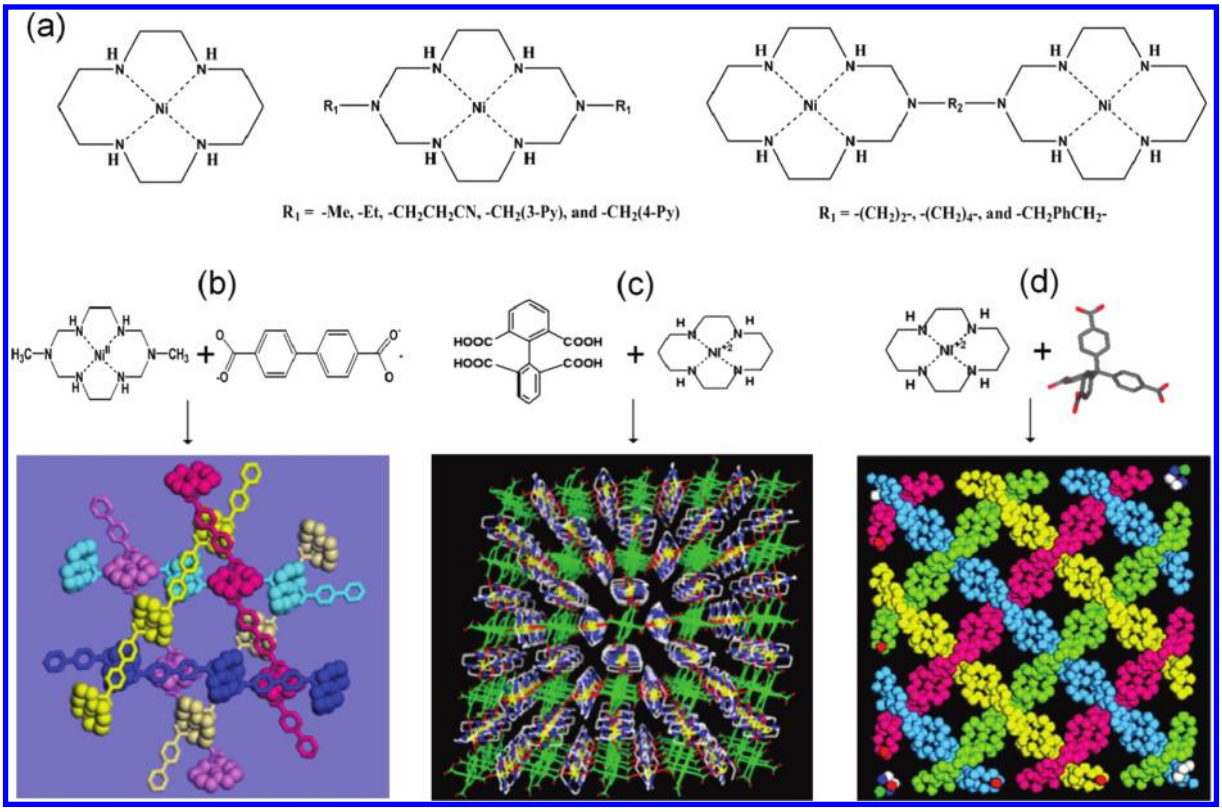

Figure 12. Typical examples of porous frameworks constructed from Ni(II) square-planar macrocyclic complexes and carboxylate ligands. (a) The employed Ni(II) macrocyclic complexes. (b) A robust 3D network formed by the packing of 1D coordination polymers in a double network of 3-fold braids.[129,130] (c) A 2D square-grid network.[131] (d) A 3D diamondoid network.[132]

The self-assembly of a Ni(II) macrocyclic complex and a linear dicarboxylate forms a linear coordination polymer, which is packed in a double network of 3-fold braids to construct an extremely robust 3D porous network. The single crystallinity and 3D packing structure were retained even after the removal of the solvent molecules by heating and evacuation. The network has a Langmuir surface area of 817 $m^2\ g^{-1}$ and pore volume of 0.37 $cm^3\ g^{-1}$. It adsorbs 1.1 wt % of H_2 at 1 atm and 77 K.[129]

In addition, 2D and 3D networks can be constructed from the Ni(II) macrocyclic complexes with tri- and tetracarboxylates. The 2D networks were prepared from Ni(II) macrocyclic complexes and tricarboyxlates.[135−138] In the case of large-sized tricarboxylates, multiple interwoven structures were formed.[138] The 2D bilayer network was prepared from BTC and a Ni(II) bismacrocyclic complex,[127,128] whose crystal behaves like a sponge, and thus shrinks and swells depending on the amount of guest solvent molecules included in the pores.

3D networks have been also prepared from Ni(II) macrocyclic complexes and tetracarboxylates. When the sizes of the tetracarboxylate ligands were very large, 8-fold, 4-fold, and doubly interpenetrated networks were generated (Figure 13).[132,133,139] The 4-fold network $\{[Ni(cyclam)]_2(MTB)\}_n$ (MTB = methanetetrabenzoate) showed a BET surface area of 141 $m^2\ g^{-1}$ (Langmuir = 154 $m^2\ g^{-1}$). At 77 K, the framework adsorbed 0.7 wt % of H_2 at 1 atm, and 1.25 wt % at 40 bar.

3.4.2. Metal-Cyanide Frameworks. Metal-cyanide frameworks are synthesized from the reaction of potassium hexacyanometallate with a different metal salt. For example, $Cu_3[Co(CN)_6]_2$ is synthesized from $K_3[Co(CN)_6]$ and $CuNO_3$ in an aqueous medium. These classes of MOFs have cubic network structures that are analogous to Prussian blue complex and are constructed of octahedral $[M(CN)_6]$ complexes linked by M^{2+} ions. The metal-cyanide frameworks have also been studied as potential hydrogen storage materials. Many of them contain accessible open metal sites, but the main limitation of these as porous materials is that the cyanide linker is too short to generate high porosity. In general, they have surface areas and pore volumes that are too small to adsorb a large amount of H_2 gas even at high pressures, except $Cu_3[Co(CN)_6]_2$ that adsorbs 2.61 wt % H_2 at 1 bar and 77 K with an isosteric heat of 6.9 kJ mol^{-1}.[140] The framework, $K_2Zn_3[Fe(CN)_6]_2$ showed a H_2 uptake capacity of 1.2 wt % at 77 K and 1.19 bar with 7.9−9.0 kJ mol^{-1} of the

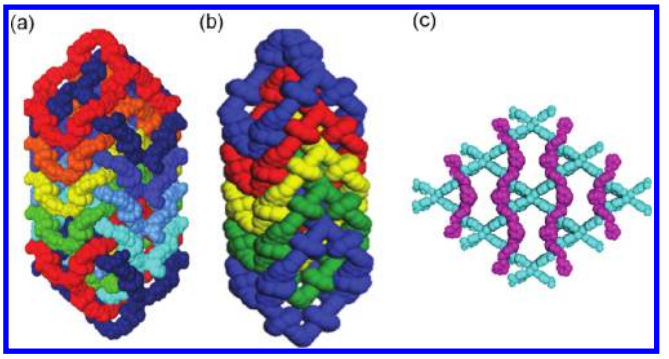

Figure 13. (a) 8-fold, (b) 4-fold, and (c) doubly interpenetrated networks constructed from various Ni(II) macrocyclic complexes and tetracarboxylate ligands. Figures adapted from refs 132, 133, and 139.

dx.doi.org/10.1021/cr200274s |*Chem. Rev.* 2012, 112, 782–835

isosteric heat of H_2 adsorption.[141] Many metal-cyanide frameworks exist that have relatively good H_2 uptake capacities at low temperature, such as $M[Fe(CN)_5NO]$ (M = Co^{2+}, Ni^{2+}),[142] $M(L)[M'(CN)_4]$ (M, M′ = Co, Ni; Co, Pd; Co, Pt; Ni, Ni; Ni, Pd),[143] $M[M'(CN)_6]$ (M, M′ = Mn, Co; Fe, Co; Co, Co; Ni, Co; Cu, Co; Zn, Co),[144] $[Ga[Co(CN)_6]$, $Fe_4[Fe(CN)_6]_3$, $M_2[Fe(CN)_6]$ (M = Mn, Co, Ni, Cu), $Co_3[Co(CN)_5]_2$,[145] $Zn_3A_2[M(CN)_6]_2$ (A = K, Rb, Cs; M = Fe, Ru, Os).[146] A series nanoporous Prussian blue analogues, $M^{II}{}_3[Co^{III}(CN)_6]_2$ (M^{II} = Mn, Fe, Co, Ni, Cu, Zn, Cd), and their H_2 adsorption capacities were also reported.[147]

3.5. Post-Synthetic Modification

Functionalization of MOFs is a method to change properties of MOFs, such as surface area and pore volume. Moreover, one can include specific functional groups that can change chemical properties of the MOF surface or provide strong interaction sites for H_2. For example, one may include a hydroxyl group in the ligand and then exchange the proton of the hydroxyl group with an alkali metal ion.[148] One may also synthesize a negatively charged framework including counter-cations and then exchange the counter-cations with alkali or alkaline earth metal ions.[149] In addition to these, several other postsynthetic modifications exist, such as covalent modification,[150] framework reduction,[151] and doping with metal nanoparticles.[134,152]

The functionalization of a MOF can be accomplished before and after the synthesis of the MOF. One can attach a specific functional group to the ligand that can be used in the construction of the MOF. This is known as "prefunctionalization". During the earlier periods of MOF chemistry, the prefunctionalization approach was used widely, especially for the introduction of $-NH_2$, $-CH_3$, −Br, etc. on the framework, which leads to the formation of a series of structures widely known as IRMOFs.[59] Similar prefunctionalization strategies provided a series of ZIFs[100] and a family of MILs.[82,83] The main problem associated with the prefunctionalization strategy is the difficulty in synthesis. The labile functional groups can be dissociated during the harsh solvothermal reaction conditions, or the functional group may take part in the reaction to provide an unwanted nonporous structure.

In 1990, Hoskins and Robson suggested the idea of postsynthetic modification.[153] In 2007, Wang and Cohen modified free $-NH_2$ groups present in IRMOF-3 by the reaction with acetic anhydride.[154] The modification was partially (>80%) made in 5 days, and even after the modification, the framework structure was maintained. Now postsynthetic modification is widely used in order to change the properties of a MOF for applications in gas storage and catalysis. A recent review by Cohen et al. provides some elaborate ideas about the postsynthetic modification of MOFs.[155,156]

By postsynthetic modification, the framework can be functionalized without altering the framework structure. Organic linker part of the framework can be modified by covalent modification, and the metal centers of the framework can be modified with various ligands. In addition, MOFs can be modified by inserting extra metal ions or metal nanoparticles into the channels. The metal centers of the MOF can be modified by generating the open metal centers followed by coordinating the ligands that have amine or pyridine groups at the open metal centers. After the functionalization of the framework, the effect of the specific functional groups on the H_2 uptake capacity can be studied. In addition, the introduction of a coordinating functional group in the framework allows the incorporation of new metal ions or metal nanoparticles, which increase the available open metal sites and thus enhance the total H_2 storage capacity. Such studies can be used to fine-tune the framework structure, metal centers, and functional groups of the ligands for the development of MOFs for ambient temperature H_2 storage.

3.5.1. Modification of Metal Centers. The postsynthetic modification at the metal centers of a MOF is less common than modification of the organic parts. Férey and co-workers reported amine-grafting at open metal sites of the MOFs.[157] The postsynthetic amine grafting was employed in the synthesis of the chromium(III)-terephthalate MIL-101. The coordinated water molecules in MIL-101 were replaced with ethylene diamine (ED), diethylenetriamine (DETA), and 3-aminopropyltrialkoxysilane (APS) by heating the sample at 423 K followed by refluxing the sample with those amines. There was no change in the crystallinity, as indicated by the powder X-ray diffraction (PXRD) patterns. After grafting the amines, the BET surface area decreased from 4230 $m^2\ g^{-1}$ to 3555 $m^2\ g^{-1}$ and the pore size was reduced. One may note that the amine modified framework is able to incorporate $[PdCl_4]^{2-}$, $[PtCl_6]^{2-}$, and $[AuCl_4]^-$ in the lattice. When the MOF incorporating those metal complex was reduced, metal nanoparticles around 2−4 nm in size were produced in the MOF. It has been reported that nanoparticles embedded in MOF increases the H_2 storage capacity.[134,158] In the other report, Farha et al. have shown that the H_2 storage capacity of MOFs can be modified by postsynthetic incorporation of pyridine type coordinating ligands at the open metal site.[159] The H_2 uptake capacities of the modified frameworks become lower than that with open metal sites. The framework with open metal sites, Zn_2(btatb) (btatb = 4,4′,4″,4‴-benzene-1,2,4,5-tetrayltetrabenzoate), shows a BET surface area of 1370 $m^2\ g^{-1}$ and the H_2 uptake capacity of 2.2 wt % at 77 K and 1 bar.

Suh et al. reported postsynthetic substitution of coordinated water molecules with bidentate organic linkers, which changes the pore size and pore shape of the MOF, leading to changes in gas sorption properties. The coordinated water molecules in $[Zn_2(TCPBDA)(H_2O)_2]\cdot 30DMF\cdot 6H_2O\}$ ($H_4TCPBDA$ = *N*,*N*,*N*′,*N*′-tetrakis(4-carboxyphenyl)biphenyl-4,4′-diamine) (SNU-30) were quantitatively substituted with 3,6-di(4-pyridyl)-1,2,4,5-tetrazine (bpta), which resulted in the new compound $[Zn_2(TCPBDA)(bpta)]\cdot 23DMF\cdot 4H_2O$ (SNU-31SC) where bpta is linked to two paddle-wheel type Zn_2 clusters, while maintaining single-crystallinity.[78] Unlike its pristine form, the bpta is significantly bent due to the steric constraints. The inserted bpta linker in SNU-31 can also be removed by immersion in DEF, which generates $[Zn_2(TCPBDA)(H_2O)_2]\cdot 23DEF$ (SNU-30SC) and again retains the single-crystallinity. The activated framework of SNU-30 (SNU-30′) adsorbed H_2, N_2, O_2, CO_2, and CH_4 gases. The BET surface area measured from the N_2 adsorption isotherm was 704 $m^2\ g^{-1}$ and the pore volume was 0.28 $cm^3\ g^{-1}$. At 1 atm, SNU-30′ has a H_2 uptake capacity of 1.42 wt % at 77 K and 0.72 wt % at 87 K. The framework has an isosteric heat of H_2 adsorption of 8.12−7.27 kJ mol^{-1}. At 77 K and 61 bar, the framework shows an excess H_2 uptake capacity of 2.75 wt % and total uptake of 3.27 wt %. At 298 K and 71 bar, the H_2 uptake capacity was 0.16 wt %. Interestingly, the postsynthetically modified framework did not adsorb H_2, N_2, O_2, CH_4 but selectively adsorbed CO_2.

3.5.2. Modification of Ligand Parts. The surface area, pore volume, and pore size of the MOFs can be modified by postsynthetic modification of the ligands. There are many reports in

dx.doi.org/10.1021/cr200274s |*Chem. Rev.* 2012, 112, 782–835

which the ligand component of MOFs are modified without collapsing the framework. Many different types of postsynthetic covalent modification are reported, such as amide coupling,[154,160,161] imine condensation,[162−164] bromination,[165] click chemistry,[166,167] etc. Detailed description can be found in the recent reviews by Cohen et al.[155,156] Cohen et al. showed that H_2 uptake capacities of the MOFs could be modified by postsynthetic modification.[150] The amine groups in various MOFs were modified to amides groups. The resulting MOFs such as IRMOF-3-AMPh, IRMOF-3-URPh, and UMCM-1-AMPh showed increased H_2 storage capacities up to 1.73 wt %, 1.54 wt %, and 1.54 wt %, respectively, compared to those of IRMOF-3 (1.51 wt %) and UMCM-1-NH_2 (1.35 wt %) at 77 K and 1 atm. Detailed discussion can be found in section 4.2.2.

4. STRATEGIES FOR IMPROVING HYDROGEN STORAGE CAPACITIES IN METAL−ORGANIC FRAMEWORKS

It has been shown through calculations and experimental results that a qualitative linear relationship exists between the H_2 storage capacities at 77 K and the specific surface areas. In Figure 14, the high pressure H_2 uptake capacities of various MOFs are presented versus the surface areas. In general, the pore volume is proportional to the specific surface area. Therefore, in order to increase the H_2 uptake capacities at 77 K, higher specific surface area and higher pore volume should be created in the MOF. However, the H_2 storage capacity decreases sharply with increasing temperature, and none of the MOFs yet satisfies the proposed DOE target at room temperature. The MOFs are physisorption-based materials for H_2 storage, and their interaction energy with H_2 molecules is very weak. Q_{st} in the porous MOFs are in the range of 5−9 kJ mol^{-1}. SNU-15, which contains an open metal site at every Co(II), has the H_2 adsorption enthalpy of 15 kJ mol^{-1} at zero coverage, but it decreases sharply as the H_2 loading increases.[168] To extend the H_2 storage performance to ambient temperature, one should increase substantially the heat of H_2 adsorption in the MOF. The predicted average heat of H_2 adsorption, which is necessary for effective ambient temperature storage and release, is ca. 15 kJ mol^{-1}.[169,170]

Snurr and co-workers performed GCMC simulations to predict H_2 adsorption isotherms in a series of 10 isoreticular MOFs (IRMOFs) at 77 K.[171] The effects of surface area, free volume, and heat of adsorption on the H_2 uptake were investigated by the simulations over a wide range of pressures at 77 K on this set of materials that have the same framework topology and surface environment but with different pore sizes. The results reveal the existence of three adsorption regimes; at low pressure (loading), the H_2 uptake correlates with the heat of H_2 adsorption, at intermediate pressure (up to 30 bar) with the surface area, and at the high pressures (120 bar) with the free volume (Figure 15).

Later, Frost and Snurr tested these correlations at room temperature and analyzed the absolute (total) and excess adsorptions.[172] The results showed that the correlations that had been held for absolute H_2 adsorption at 77 K could not be applied for absolute H_2 adsorption at 298 K due to very weak adsorption energy between MOF and H_2. Even at low loadings, the absolute adsorbed amount of H_2 at 298 K mainly correlates with the free volume. They also found that at low loading the excess adsorption of H_2 at 298 K correlates well with the heat of adsorption again, but at high loadings, the adsorption correlates better with the surface area than with the free volume (Figure 16). They suggested that a reasonable goal of 9 wt % and 30 g L^{-1} could be obtained with MOFs that can provide an isosteric heat of 15 kJ mol^{-1}

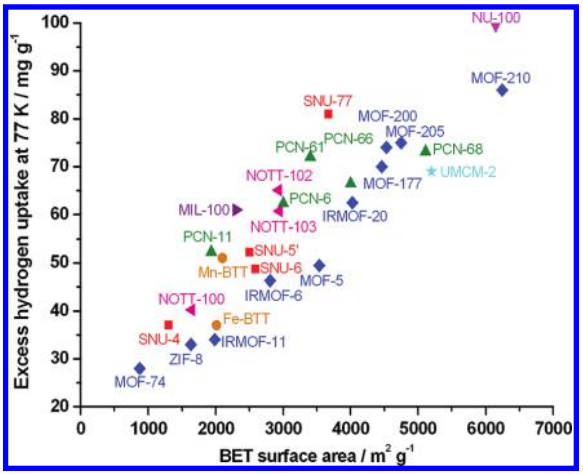

Figure 14. Excess high pressure H_2 uptake capacities at 77 K versus BET surface areas for some highly porous MOFs.

or higher while maintaining a free volume of 2.5 cm^3 g^{-1} and void fraction of 85%.

4.1. Increase in Surface Area and Pore Volume

Selected data for the H_2 uptake capacities and the surface areas of the MOFs reported so far are summarized in Tables 1 and 2. As shown in Figure 17, the H_2 uptake capacities at 77 K and 1 atm are related with the surface areas in the range of 100−2000 m^2 g^{-1}, but they hardly relate with the surface area when the surface area exceeds 2000 m^2 g^{-1}. It seems that at 1 atm of H_2 pressure, the surface area greater than 2000 m^2g^{-1} cannot be fully covered with H_2 molecules, since at low pressure, H_2 will preferentially bind on the sites that have large affinity for H_2. In addition, low-pressure H_2 adsorption may be influenced by other factors such as pore size, catenation, ligand functionalization, and open metal sites. For example, the H_2 uptake capacity at 77 K and 1 atm for doubly interpenetrating SNU-77 (1.80 wt %), which has a BET surface area of 3670 m^2 g^{-1} and a pore size of 8.0 Å,[173] is higher than that of MOF-177 (1.24 wt %) that has higher surface area (4750 m^2 g^{-1}) and larger pores (11.8 Å) in the noninterpenetrating (6,3)-connected net,[45] but it is lower than that of $[Zn_4O(NTB)_2]$ (SNU-1, 1.9 wt %) that has a much smaller surface area (1120 m^2 g^{-1}) and smaller pores (5.0 Å) in the doubly interpenetrating nets.[94] The factors influencing the H_2 uptake of porous MOFs will be discussed in the following sections. However, the H_2 uptake capacities at 77 K under high pressures show a quite nice qualitative relationship with the surface areas. As the surface area increases, the high pressure H_2 uptake capacity at 77 K increases.

4.1.1. Elongation of Ligands. The MOFs constructed from long organic ligands tend to collapse after removal of guest molecules. In addition, the longer ligands often lead to the framework interpenetration that gives rise to a reduced surface area or even a nonporous structure. However, some reports have shown that with a given framework topology, the surface area can be increased by using the elongated ligands. Suh and co-workers reported doubly interpenetrated pyr (pyrite) frameworks, $[Zn_4O(NTB)_2]$ (SNU-1)[94] and $[Zn_4O(TCBPA)_2]$ (SNU-77),[173] which were constructed from $[Zn_4O(COO)_6]$ octahedral secondary building units (SBUs) and tricarboxylates, NTB in the former and TCPBA in the latter. TCBPA is tris(4′-carboxybiphenyl)amine that is an extended form of NTB. Both frameworks

dx.doi.org/10.1021/cr200274s |Chem. Rev. 2012, 112, 782–835

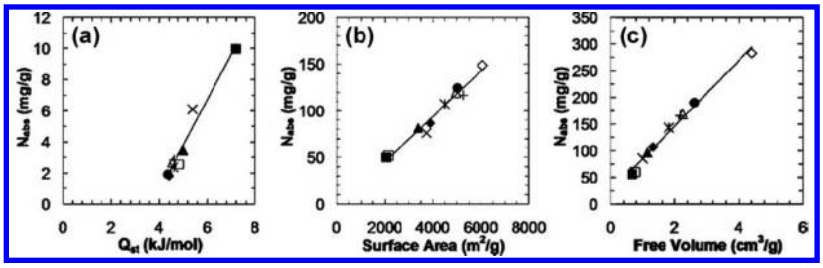

Figure 15. Simulated H_2 adsorption in a series of 10 IRMOFs at 77 K. (a) Adsorbed amounts at 0.1 bar vs isosteric heat of adsorption. (b) Adsorbed amounts at 30 bar vs accessible surface area. (c) Adsorbed amounts at 120 bar vs free volume. ♦, IRMOF-1; ■, IRMOF-4; ▲, IRMOF-6; x, IRMOF-7; *, IRMOF-8; ●, IRMOF-10; +, IRMOF-12; Δ, IRMOF-14; ◊, IRMOF-16; □, IRMOF-18. Reproduced with permission from ref 171. Copyright 2006 the American Chemical Society.

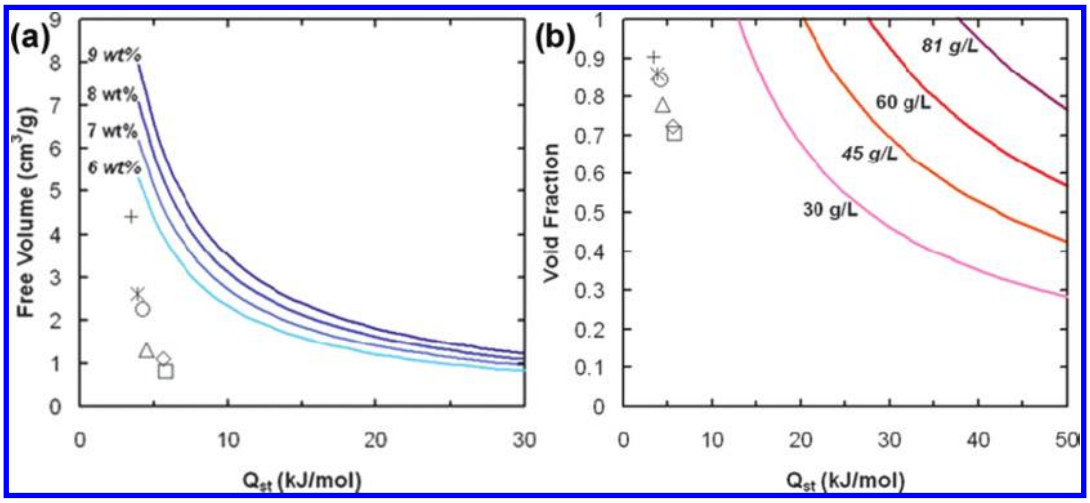

Figure 16. (a) Requirements for target gravimetric H_2 loadings at 120 bar and 298 K. (b) Requirements for target volumetric H_2 loadings at 120 bar and 298 K. Results for existing materials are marked with symbols: Δ, IRMOF-1; ◊, IRMOF-10; *, IRMOF-14; +, IRMOF-16; □, CuBTC. Reproduced with permission from ref 172. Copyright 2007 the American Chemical Society.

exhibit high permanent porosity, high thermal stability (up to 400 °C), guest-dependent luminescence, and single-crystal-to-single-crystal transformations, mainly rotational motions in response to removal of the guest molecules. The Langmuir surface area of SNU-77 is 4180 $m^2\ g^{-1}$, which is much higher than that (1121 $m^2\ g^{-1}$) of SNU-1.

Yaghi and co-workers also reported Zn_4O-based MOFs, MOF-177 and MOF-200, which are noninterpenetrating qom networks.[29] MOF-200 was prepared from BBC that is an elongated form of BTB employed in the synthesis of MOF-177. MOF-200 shows ultrahigh surface areas of 10 400 $m^2\ g^{-1}$ (Langmuir) and 4520 $m^2\ g^{-1}$ (BET) as determined by N_2 gas sorption data, while MOF-177 has surface areas of 5640 $m^2\ g^{-1}$ (Langmuir) and 4750 $m^2\ g^{-1}$ (BET).[45]

Schröder and co-workers reported an isostructural series of MOF having NbO type networks of $6^4 \cdot 8^2$ topology that were constructed from $[Cu_2(COO)_4]$ paddle-wheel configuration and tetracarboxylate ligands.[24] It was observed that elongation of the ligand dramatically increases pore diameter along the *c* axis from 10.0 Å in NOTT-100 to 32.0 Å in NOTT-102. As summarized in Table 3, the framework NOTT-100 that was synthesized from the shortest ligand shows the lowest BET surface area, pore volume, and pore size. The highest pore volume and BET surface area were obtained with NOTT-102 that incorporates the longest ligand.

An isoreticular series of rht topology with hexacarboxylate ligands have been also reported.[28,265,275,276] These MOFs contain the ligands having C_3 symmetry with three coplanar isophthalate moieties and the metal−organic polyhedra. The biggest hexacarboxylate reported is 5,5′,5″-(((benzene-1,3,5-triyltris(ethyne-2,1-diyl))tris(benzene-4,1-diyl))tris-(ethyne-2,1-diyl))triisophthalic acid (ttei). A solvothermal reaction of H_6ttei and $Cu(NO_3)_2 \cdot 2.5H_2O$ in DMF/HBF_4 afforded $[Cu_3(ttei)(H_2O)_3]_n$ (NU-100/PCN-610), whose X-ray crystal structure revealed noninterpenetrating (3,24)-connected framework formed from Cu_2-paddle-wheel units. Activated NU-100 prepared by a supercritical CO_2 drying method exhibits an ultra high BET surface area of 6143 $m^2\ g^{-1}$ and a pore volume of 2.82 $cm^3\ g^{-1}$. The excess H_2 uptake of NU-100 was 99.5 mg g^{-1} at 56 bar, and the total was 164 mg g^{-1} at 70 bar and 77 K. These values are the highest in excess among those of the MOFs reported so far, and second in total H_2 uptake after MOF-210. The reason why those MOFs from extended hexatopic ligand are stable is because of the formation of a special 3,24-connected network, which effectively reduces the pore opening and prevents the network interpenetration. This approach is an effective way to increase the MOFs' surface area without sacrificing their stability.

4.1.2. Catenation and Interpenetration. Catenation refers the physical entanglement of two or more identical frameworks.[277] It is also known as interpenetration, but interpenetration

dx.doi.org/10.1021/cr200274s |*Chem. Rev.* 2012, 112, 782–835

Table 1. The H_2 Gas Sorption Data for MOFs without Open Metal Sites

		surface area/$m^2\ g^{-1}$				hydrogen storage capacity[a]					
MOF		BET	Langmuir	pore size/ Å	pore volume/ $cm^3\ g^{-1}$	P/ bar	T/ K	gravimetric/ wt %	volumetric/ $g\ L^{-1}$	Q_{st}/ kJ mol^{-1}	ref
$Be_{12}(OH)_{12}(BTB)_4$		4030	4400			1	77	1.6		5.5	174
						20(100)	77	6 (9.2)	(43)		
						95	298	(2.3)	(11)		
$Mg_3(HCO_2)_6$		150		4.5, 5.5	0.043	1	77	0.6			175
$Mg_3(NDC)_3$	TUDMOF-2	190	520	3.6		1	77	0.78		9.5	91
Al(OH)(BDC)	MIL-53(Al)	1100		8.5		16	77	3.8	37		176
$Al_{12}O(OH)_{18}(H_2O)_3$-$(Al_2(OH)_4)(BTC)_6$	MIL-96					3	77	1.91			177
$Sc(BDC)_3$		721		5.4	0.332	1	77	1.5			178
$[Sc_2(BPTC)(OH)_2]$	NOTT-400	1350		7.5	0.56	1	77	2.14		5.96	179
						20	77	(3.84)			
[Sc(TDA)(OH)]	NOTT-401	1514		6.2	0.66	1	77	2.31		6.65	179
						20	77	(4.44)			
$Mn(HCO_2)_2$		297		4.5		1	77	0.9			180
$Mn_3[(Mn_4Cl)_3(tpt\text{-}3tz)_8]_2$		1580	1700			25 (80)	77	3.7 (4.5)			113
$Fe_3(OH)(pbpc)_3$		1200				1	77	1.6			181
						20	77	3.05			
Co(BDP)			2670		0.93	30	77	3.1			105
Co(HBTC)(4,4′-bpy)		887		5, 8		72	77	2.05		7.0	89
						72	298	0.96			
Co(NDC)(4,4′-bpy)			115	5.1, 4.0	0.1	1	77	0.72			182
Co(ox)(4,4′-bpy)						1	77	0.1			183
$Co_2(6\text{-mna})_2$	CUK-2	420			0.17	1	77	0.66			184
$Co_2(BDC)_2(dabco)$		1595	2120		0.77	10	298	0.03			185
						44.2	77	4.11			186
						100	293	0.32			
$Co_3(BDC)_3(dabco)$		360	538		0.2	0.93	77	1	51.2		187
$Co_3(bpdc)_3(4,4'\text{-bpy})$		922		8	0.38	1	77	1.98		7.1	188
$Co_3(NDC)_3(dabco)$		1502	2293	4.5	0.82	1	77	2.45	29.8		187
						17.2	298	0.89	10.8		
$Co_3(2,4\text{-pdc})_2(OH)_2$	CUK-1	630			0.26	1	77	1.6			184
$[Co_9(BTC)_6(tpt)_2(H_2O)_{15}]$				8,6		1	77	0.89			189
Ni(cyclam)(bpydc)			817	5.8	0.37	1	77	1.1			129
Ni(HBTC)(4,4′-bpy)		1590		5, 8		72	77	3.42		8.8	89
						72	298	1.2			
Ni(ox)(4,4′-bpy)						1	77	0.16			183
$[Ni^{II}_2Ni^{III}(\mu_3\text{-}OH)(IN)_3(BDC)_{1.5}]_3$		571.0	888.3			1	77	1.47			190
$Ni_3(OH)(pbpc)_3$		1553				1	77	1.99			181
						20	77	4.15			
$Ni_3O(TATB)_2$	PCN-5		225		0.13	1	77	0.63			191
$Cu(bpy)(CF_3SO_3)_2$						1	40	1.4			192
Cu(dccptp)(NO_3)		268			0.113	1	77	1.34		6.12	193
						20	77	1.91	23.9		
$Cu(fma)(bpe)_{0.5}$				3.2, 2.0		1	77	0.8			194
$Cu(2\text{-pymo})_2$		350		2.9		1.2	77	0.86	13		195
$Cu(F\text{-pymo})_2$						1.2	90	0.56	10		196
$Cu(hfipbb)(h_2hfipbb)_{0.5}$						1	77	0.23			183
						48	298	1	14.7		197
$Cu_2(abtc)(DMF)_2$	SNU-5		1260		0.48	1	77	1.83			76
$Cu_2(BDC)_2(dabco)$		1461				1	77	1.8			198

dx.doi.org/10.1021/cr200274s |*Chem. Rev.* 2012, 112, 782–835

Table 1. Continued

MOF		surface area/$m^2\ g^{-1}$		pore size/ Å	pore volume/ $cm^3\ g^{-1}$	hydrogen storage capacity[a]					
		BET	Langmuir			P/ bar	T/ K	gravimetric/ wt %	volumetric/ $g\ L^{-1}$	Q_{st}/ $kJ\ mol^{-1}$	ref
		1300	1703		0.63	33.7	77	2.7			186
						100	293	0.42			
$Cu_2(BPnDC)_2(4,4'\text{-bpy})$	SNU-6	2590	2910	14.0, 18.2	1.05	1	77	1.68	5.31	7.74	57
						70	77	4.87 (10.0)	15.4		
$Cu_3[(Cu_4Cl)_3(tpb\text{-}3tz)_8]_2\cdot 11CuCl_2$		1120	1200			30	77	2.8			113
$Zn(abdc)(bpe)_{0.5}$			100			1	77	0.62			80
$Zn(MeIM)_2$	ZIF-8	1630	1810		0.64	1	77	1.27			100
						55	77	3.01			
						1	77	1.3		4.5	199
						30	77	3.3			
						60	298	0.13			
$Zn(PhIM)_2$	ZIF-11					1	77	1.35			100
$Zn(BDC)(4,4'\text{-bpy})_{0.5}$	MOF-508		946	4.0, 4.0		1	77	0.8			56
$Zn(NDC)(bpe)_{0.5}$			303	5.1, 4.3	0.2	40	77	2	18		200
						65	298	0.3			
Zn(tbip)		256				1	77	0.75	54	6.7	201
$Zn_2(abtc)(DMF)_2$	SNU-4		1460		0.53	1	77	2.07			76
						50	77	3.7			
$Zn_2(BDC)(tmbdc)(dabco)$		1100	1670		0.59	1	77	2.08			115
$Zn_2(BDC)_2(dabco)$		1264				1	77	1.92			202
		1165	1488			83.2	77	3.17			186
						1	77	2.1		5.3	198
Zn(bpe)(tftpa)		512			0.203	1	77	1.04		6.2	203
$Zn_2(bpytc)$		313	424		0.15	4	77	1.1			204
$Zn_2(btatb)(DMF)_2$		796				1	77	1.2		7.4	159
$Zn_2(btatb)(Py)$		709				1	77	1.24			
$Zn_2(btatb)(MePy)$		370				1	77	0.59			
$Zn_2(btatb)(EtPy)$		309				1	77	0.57			
$Zn_2(btatb)(ViPy)$		473				1	77	1.04			
$Zn_2(btatb)(CF_3Py)$		388				1	77	0.57			
$Zn_2(cnc)_2(dpt)$			342		0.19	1	77	1.28		7.85	205
$Zn_2(NDC)_2(dabco)$		1000	1450		0.52	1	77	1.7			115
$Zn_2(NDC)_2(diPyNI)$		802			0.30	1	77	0.92		5.6	151
$Zn_2(tcpdep)$			252			1	77	0.2			206
$Zn_2(tfbdc)_2(dabco)$		1070	1610		0.57	1	77	1.78			115
$Zn_2(tmbdc)_2(4,4'\text{-bpy})$		1120	1740		0.62	1	77	1.68			
$Zn_2(tmbdc)_2(dabco)$		920	1400		0.5	1	77	1.85			
$Zn_3(bpdc)_3(4,4'\text{-bpy})$		792		8	0.33	1	77	1.74		7.1	188
$Zn_3(NTB)_2$			419	7.72	0.15	1	77	1			95
$Zn_3(TATB)_2(HCO_2)$			1100			1	77	1.3			207
$Zn_4O(adc)_3$	PCN-13		150	3.5	0.1	1	77	0.41			208
$[Zn_4O(azd)_3]$	MOF-646	925	1130			1	77	1.75	20.9	7.8	209
$Zn_4O(BBC)_2(H_2O)_3\cdot H_2O$	MOF-200	4530	10400		3.59	80	77	7.4(16.3)	(36)		29
$Zn_4O(BDC)_3$	MOF-5, IRMOF-1	2296	3840			50	77	4.7		3.8	210
						65	298	0.28			
						60	200	0.9			
						48	298	1.65	9.9		197
		3362				1	77	1.32			60
		3534	4171			45.4	77	4.95	30.8		62
			3080			30	77	4.3		4.1	211
						60	298	0.45			
		572	1014			67	298	0.2			212
						10	77	1.6			

dx.doi.org/10.1021/cr200274s |*Chem. Rev.* 2012, 112, 782–835

Table 1. Continued

MOF		surface area/$m^2\ g^{-1}$ BET	Langmuir	pore size/ Å	pore volume/ $cm^3\ g^{-1}$	hydrogen storage capacity[a] P/ bar	T/ K	gravimetric/ wt %	volumetric/ g L^{-1}	Q_{st}/ kJ mol^{-1}	ref
		2885			1.18	1	77	1.15			213
		3800	4400			40(100)	77	7.1 (10)	42.1 (66)		31
						1	77	1.32		4.8	61
			3080			30	77	4.3			211
						1	77	1.35			199
						35	77	5.75			
						60	298	0.3			
						1	77	4.5			30
$Zn_4O(BDC)_3$ (interpenetrated)	MOF-5		1130	6.7		1	77	2.0	23.3	7.6	214
						100	77	(2.8)	33		64
$Zn_4O(bpdc)_2$	IRMOF-9	1904	2613		0.9	1	77	1.17			61
$Zn_4O(Brbdc)_2$	IRMOF-2	1722	2544		0.88	1	77	1.21			61
$Zn_4O(BTB)_2$	MOF-177	4526				1	77	1.25			60
		4746	5640			70	77	7.5	32		62
		4750	5640		1.59	66	77	7.1	49		63
$Zn_4O(BTB)_{4/3}(NDC)$	MOF-205	4460	6170		2.16	80	77	7.0(12.0)	(46)		29
$Zn_4O(BTE)_{4/3}(BPDC)$	MOF-210	6240	10400		3.6	80	77	8.6(17.6)	(44)		
$Zn_4O(D_2\text{-TCPPDA})_{1.5}$			2095			1	77	0.8			215
$Zn_4O(dbdc)_2$	IRMOF-6	2476	3263		1.14	1	77	1.48			61
		2804	3305			45	77	4.63	31.7		62
$Zn_4O(dcbBn)_3$		396		4.5	0.13	48	298	0.98			216
$Zn_4O(dcdEt)_3$		502		4.7	0.2	48	298	1.12			
$Zn_4O(NH_2\text{-bdc})_2$	IRMOF-3	2446	3062		1.07	1	77	1.42			61
$Zn_4O(hpdc)_3$	IRMOF-11		1911			1	77	1.62			60
		1984	2337	9		33.7	77	3.4	26.7		62
$Zn_4O(NDC)_3$	IRMOF-8	890			0.45	1	77	1.45			202
		1466				1	77	1.50			60
			1818			15	77	3.6	20.9	6.1	211
						30	298	0.4	2.32		
$Zn_4O(NTB)_2$	SNU-1		1121	5	0.51	1	77	1.9			94
$Zn_4O(pyrdc)_2$	IRMOF-13	1551	2100		0.73	1	77	1.73			61
$Zn_4O(TCBPA)_2$	SNU-77H	3670	4180	8.1, 4.1	1.52	1	77	1.79	10.5	7.05	173
						90	77	8.1(11.0)	47.4		
						90	298	0.5(1.19)	2.93		
$Zn_4O(T^2DC)(BTB)_{4/3}$	UMCM-2	5200	6060			46	77	6.9		6.4	72
$Zn_4O(ttdc)_2$	IRMOF-20	3409	4346		1.53	1	77	1.35			61
		4024	4593			77.6	77	6.25	34.1		62
$Zn_4(trz)_4(1,4\text{-ndc})_2$		362				1	77	0.84			217
$Zn_4(trz)_4(2,6\text{-NDC})_2$		584				1	77	1.09			217
$Zn_6(BTB)_4(4,4'\text{-bipy})_3$	FJI-1	4043	4624	1.21		1	77	1.02		4.62	218
						37(62)	77	6.52(9.08)			
						65	298	0.43			
$Zn_7O_2(pda)_5(H_2O)_2$					0.17	71.43	298	1.01			219
$Pd(2\text{-pymo})_2$		600				1.2	77	1.3	18		195
$Pd(F\text{-pymo})_2$		600				1.2	77	1.15	18		220
$Ag_2[Ag_4(trz)_6]$	FMOF-1	810			0.324	64	77	2.33	41		221
$Cd_3(bpdc)_3$	JUC-48		880	25	0.19	100	298	1.1			222
						40	77	2.8	20		
$Cd(pymc)_2$	*rho*-ZMOF		1168		0.47	1	77	1.16		8.7	223
$[In(pmdc)_2Na_{0.36}K_{1.28}](NO_3)_{0.64}$	*sod*-ZMOF		616		0.25	1	77	0.9		8.4	223
$(In_3O)(OH)(adc)_2(IN)_2$		1496	1857			1	77	2.08		6.9	224
$(In_3O)(OH)(adc)_2(MH_2IN)_2$		1716	2106			1	77	2.31		7.9	

dx.doi.org/10.1021/cr200274s |*Chem. Rev.* 2012, 112, 782–835

Table 1. Continued

MOF		surface area/$m^2\ g^{-1}$ BET	Langmuir	pore size/ Å	pore volume/ $cm^3\ g^{-1}$	hydrogen storage capacity[a] P/ bar	T/ K	gravimetric/ wt %	volumetric/ g L^{-1}	Q_{st}/ kJ mol^{-1}	ref
$[CH_3NH_3][In_3O(bpdc)_3(HCO_2)_{3/2}(H_2O)]_2$	CPM-13	904	1441	7.02	0.487	1	77	1.0			225
$Yb_4(TATB)_{8/3}(SO_4)_2$	PCN-17	820			0.34	1	77	0.94			226

[a] The data in parentheses are total uptake amounts.

Table 2. The H_2 Gas Sorption Data for MOFs with Open Metal Sites

MOF		surface area/ $m^2\ g^{-1}$ BET	Langmuir	pore size/ Å	pore volume/ $cm^3\ g^{-1}$	hydrogen storage capacity[a] P/bar	T/K	gravimetric/ wt %	volumetric/ g L^{-1}	Q_{st}/ kJ mol^{-1}	ref
					Dicarboxylic Acid						
$Mg_2(dobdc)$	MOF-74(Mg)	1510				1	77	2.2		10.3	227
						15(100)	77	3.2 (4.9)	(49)		
						(100)	298	(0.8)	(7.5)		
$Cr_3OF(BDC)_3$	MIL-101		5500	8.6	1.9	6080	77	6.1	1.84	10	84
							298	0.43			
Mn(NDC)		191		6.1	0.068	1	77	0.57			228
$Fe_3O(tfbdc)_3$			635			1	77	0.9			229
$NaNi_3(OH)(sip)_2$		700				1	77	0.94		10.4	230
$Ni(dhtp)_2$			1083		0.41	70	77	1.8			231
						70	298	0.3			
Cu(peip)		1560	1780		0.696	1	77	2.51		6.63	232
						40	77	4.14			
						100	298	0.46			
Cu(pmip)		1490	1690		0.605	1	77	2.36		7.24	233
$Cu_6O(tzi)_3(NO_3)$		2847	3223		1.01	1	77	2.4		9.5	124
Zn(peip)		1660	1880		0.667	1	77	2.27		6.56	232
$Zn_2(dhtp)$	MOF-74, CPO-27-Zn	783	1132		0.39	1	77	1.77		8.3	61
		950	1072			26.1	77	2.21	27.6		62
		870				30	77	2.8		8.8	234
$Zn_3(BDC)_3(Cu(pyen))$					0.26	1	77	0.66		12.3	235
$Zn_3(OH)(cdc)_{2.5}$		152		5		1	77	2.1		7	236
$Y_2(pdc)_3$		676				1	77	1.32			237
$Sm_2Zn_3(oxdc)_6$		719			0.31	34	77	1.19			54
						35	298	0.54			
$Er_2(3,5\text{-}pdc)_3$		427				1	77	0.68			237
					Tricarboxylic Acid						
$Cr_3(BTC)_2$		1810	2040			1	77	1.9		7.4	238
$Cr_3OF(BTC)_2$	MIL-100		2700	25, 29	1	73.3	298	0.15	1.04	6.3	84
						90	77	3.28	23		
$Cr_3OF(ntc)_{1.5}$	MIL-102		42	4.4	0.12	35	77	1		6	239
						35	298	0.05			
$Fe_4O_2(BTB)_{8/3}$		1121	1835		0.69	1	77	2.1			240
$H_2[Co_4O(TATB)_{8/3}]$	PCN-9		1355	6.5	0.51	1	77	1.53		10.1	88
$Cu_3(TATB)_2$ (catenated)	PCN-6		3800	5	1.456	1	77	1.9			241
						50	77	7.2		6.2	242
$Cu_3(TATB)_2$ (noncatenated)	PCN-6′		2700		1.045	1	77	1.35		6	243
						50	77	4.2			242

dx.doi.org/10.1021/cr200274s |*Chem. Rev.* 2012, 112, 782–835

Table 2. Continued

MOF		surface area/ $m^2\ g^{-1}$ BET	Langmuir	pore size/ Å	pore volume/ $cm^3\ g^{-1}$	hydrogen storage capacity[a] P/bar	T/K	gravimetric/ wt %	volumetric/ $g\ L^{-1}$	Q_{st}/ $kJ\ mol^{-1}$	ref
$Cu_3(bhtc)_2$	UMCM-150	2300	3100		1	1	77	2.1		7.3	244
						45	77	5.7	36		
Y(BTC)						1	77	1.57		7.3	245
						10	77	2.1	28.8		
$Mo_3(BTC)_2$	TUDMOF-1	1280	2010		0.67	1	77	1.75			246
Dy(BTC)		655		6		1	77	1.32			247
				Tetracarboxylic Acid							
$Co_2(H_2O)_2(MTB)$	SNU-15′					1	77	0.74		15.1	168
$Cu_2(bdpb)$	PMOF-3	1879	2489			1	77	2.47			248
$Cu_2(bptc)$	MOF-505		1830	6.5	0.63	1	77	2.47			249
	NOTT-100	1670			0.68	1	77	2.59	(38.9)	6.3	250
						20	77	(4.02)			75
$Cu_2(tptc)$	NOTT-101	2247		7.3	0.89	1	77	2.52	43.6	5.3	75, 250
						20	77	6.06			
$Cu_2(qptc)$	NOTT-102	2932		8.3	1.14	1	77	2.24	41.1	5.4	75, 250
						20	77	6.07			
Cu_2(L, tetracarboxylate)	NOTT-103	2929		8	1.142	1	77	2.63		5.71	75
						20	77	(6.51)			
						60	77	(7.78)			
	NOTT-105	2387		7.3	0.898	1	77	2.52		5.77	75
						20	77	(5.40)			
	NOTT-106	1855		7.3	0.798	1	77	2.29		6.34	75
						20	77	(4.50)			
	NOTT-107	1822		7	0.767	1	77	2.26		6.70	75
						20	77	(4.46)			
	NOTT-109	1718		6.9	0.705	1	77	2.33			75
						20	77	(4.15)			
	NOTT-110	2960		8	1.22	1	77	2.64		5.68	251
						55	77	5.43	46.8		
	NOTT-111	2930		8	1.19	1	77	2.56		6.21	251
						48	77	5.47	45.4		
$Cu_2(aobtc)$	PCN-10	1407	1779		0.67	1	77	2.34	18	6.8	252
						3.5	30	6.84	52.5		
						45	300	0.25			
$Cu_2(sbtc)$	PCN-11	1931	2442		0.91	1					252
						3.5	30	7.89	59.1		
						45	77	5.23	39.2		
$Cu_2(C_{2v}$-mdip)	PCN-12′	1577	1962		0.73	1	77	2.4	20.4		253
$Cu_6(C_s$-mdip$)_2(C_{2v}$-mdip)	PCN-12	1943	2425		0.94	1	77	3.05	23.2		253
Cu_2(adip)	PCN-14	1753				1	77	2.7		8.6	254
						45	77	4.42	36.6		
Cu_2(ebdc)	PCN-16	2273	2800		1.06	1	77	2.6			255
						~45	77	5.1			
Cu_2(ebdc)	PCN-16′	1760	2200		0.84	1	77	1.7			255
						~28	77	2.9			
Cu_2(PMTB)	PCN-21	2718	4485		1.54	1	77	1.6			256
Cu_2(bdi)	PCN-46	2500	2800		1.012	1	77	1.95		7.2	257
						32(97)	77	5.31(6.88)	34.7(45.7)		

dx.doi.org/10.1021/cr200274s |*Chem. Rev.* 2012, 112, 782–835

Table 2. Continued

MOF		surface area/ $m^2\ g^{-1}$ BET	Langmuir	pore size/ Å	pore volume/ $cm^3\ g^{-1}$	hydrogen storage capacity[a] P/bar	T/K	gravimetric/ wt %	volumetric/ $g\ L^{-1}$	Q_{st}/ $kJ\ mol^{-1}$	ref
Cu_2(abtc)	JUC-62				0.89	40	77	4.71	53		258
	SNU-5		2850		1	1	77	2.84			76
						50	77	5.22			
Cu_2(TCM)	SNU-21S		905	6.6, 9.2	0.31	1	77	1.95		6.65	259
						70	77	4.37			
						70	298	0.26			
	SNU-21H		695	6.3, 10.7	0.25	1	77	1.64		6.09	259
						70	77	4.36			
						70	298	0.18			
Cu_2(bdcppi)	SNU-50′	2300	2450	11	1.08	1	77	2.1		7.1	260
						60	77	5.53 (7.86)			
						61	298	0.399 (0.980)			
Cu_2(BDDC)		2357	3111		1.113	0.95	77	1.64	15	6.9	261
						17(31)	77	3.98(4.60)	36(41)		
Cu_2(tcpdep)			733			1	77	0.8			206
Cu_2(C_{2h}-TCPPDA)			504			1	77	1.2			262
Cu_2(D_{2h}-TCPPDA)			626			1	77	1.4			
Zn_2(btatb)		1370				1	77	2.2		8.1	205
In_3O(abtc)$_{1.5}$(NO_3)	*soc*-MOF		1417	7.65, 5.95	0.5	1.2	77	2.61		6.5	85
					Hexacarboxylic						
Cu_3(abtt)	NOTT-114	3424			1.36	1	78	2.28			263
						30 (60)	78	5.0 (6.8)	(41.6)	5.3	
Cu_3(BHB)	UTSA-20	1156		3.4, 8.5		1	77	2.9			264
						15	77	4.1			
Cu_3(btei)	PCN-61	3000	3500		1.36	1	77	2.25	12.6	6.36	265
						33	77	6.24	35		
						90	298	0.667	3.74		
Cu_3(btti)	NOTT-119	4118			2.35	1	77	1.4		7.3	266
						44 (60)	77	5.6 (9.2)	(37)		
Cu_3(btti)	PCN-69	3989			2.173	1	77	1.7		8.14	267
						60	77	5.22			
Cu_3(ntbd)	NOTT-115	3394			1.38	1	78	2.42			263
						33(60)	78	5.6 (7.5)	(49.3)	5.8	
Cu_3(ntei)	PCN-66	4000	4600		1.63	1	77	1.79	7.98	6.22	265
						45	77	6.65	29.6		
						90	298	0.785	3.5		
Cu_3(ptei)	PCN-68	5109	6033		2.13	1	77	1.87	7.2	6.09	265
						50	77	7.32	28		
						90	298	1.01	4.1		
Cu_3(tbtt)	NOTT-113	2970			1.25	1	78	2.39			263
						30 (60)	78	5.1 (6.7)	(42.5)	5.9	
Cu_3(ttei)	NU-100	6143			2.82	1	77	1.82		6.1	28
						56(70)	77	9.95(16.4)			
Cu_3(L, hexacarboxylate)	NOTT-112	3800				1	78	2.3		5.64	268
						35−40 (77)	77	7.07 (10)	(50.3)		
	PMOF-2(Cu)	3730	4180			1	77	2.29		9.2	269
						30 (50)	77	5 (7)	(39.2)		
					Octacarboxylic Acid						
Cu_4(L)	NOTT-140	2620			1.07	1	77	2.5		4.15	270
						20	77	(6)			

dx.doi.org/10.1021/cr200274s |*Chem. Rev.* 2012, 112, 782–835

Table 2. Continued

MOF		surface area/ $m^2\ g^{-1}$ BET	Langmuir	pore size/ Å	pore volume/ $cm^3\ g^{-1}$	hydrogen storage capacity[a] P/bar	T/K	gravimetric/ wt %	volumetric/ g L^{-1}	Q_{st}/ kJ mol^{-1}	ref
					Azolates						
$Mn_3[(Mn_4Cl)_3(BTT)_8]_2$	Mn-BTT	2100			0.795	1.2	77	2.2	43	10.1	48
						90	77	5.1 (6.9)	(60)		
						90	298	0.94	7.9		
$Mn_3[(Mn_4Cl)_3(BTT)_8]_2 \cdot 0.75CuPF_6$		1911	2072			1.2	77	2		9.9	112
$Fe_3[(Mn_4Cl)_3(BTT)_8]_2 \cdot FeCl_2$		2033	2201			1.2	77	2.21		10.2	112
$Fe_3[(Fe_4Cl)_3(BTT)_8(MeOH)_4]_2$	Fe-BTT	2010	2200			1.2	77	2.3		11.9	271
						13(95)	77	3.7(4.1)	(35)		
$Co_3[(Mn_4Cl)_3(BTT)_8]_2 \cdot 1.7CoCl_2$		2096	2268			1.2	77	2.12		10.5	112
$Ni_{2.75}Mn_{0.25}[(Mn_4Cl)_3(BTT)_8]_2$		2110	2282			1.2	77	2.29		9.1	112
Cu(BDT)		200				1	77	0.66			114
$Cu_3[(Cu_{2.9}Mn_{1.1}Cl)_3(BTT)_8]_2 \cdot 2CuCl_2$		1695	1778			1.2	77	2.02		8.5	112
$Cu_9(4\text{-TBA})_{10}(C_2H_5OH)$ 2		616	686			1	77	1.16			62
$Cu_2(4\text{-TBA})_2(DMF)(C_2H_5\ OH)$		356	402	4.24		1	77	1.54			62
$Cu_2(2\text{-F-4-TBA})_2(DMF)_2$						1	77	0.67			62
$Cu_4(TTPM)_2 \cdot 0.7CuCl_2$		2506	2745			1	77	2.8			272
						20 (70)	77	4.1 (5.6)	(41)		
$HCu[(Cu_4Cl)_3(BTT)_8] \cdot 3.5HCl$	Cu-BTT	1710	1770			1.2	77	2.42		9.5	273
						20(70)	77	4.1 (~6)	38(53)		
						90	298	(0.46)			
$Zn_3(BDT)_3$		640				1.17	77	1.46		8.7	114
$Zn_3[(Zn_{0.7}Mn_{3.3}Cl)_3(BTT)_8]_2 \cdot 2ZnCl_2$		1927	2079			1.2	77	2.1		9.6	112
$[Zn_5Cl_4(BTDD)_3]$	MFU-4 L	2750		1.2, 1.86	1.15	20	77	4		5	274
						20	117	1.8			
$[Cd_2(Tzc)_2]$		230	339			1	77	0.55		11.4	55

[a] The data in parentheses are total uptake amounts.

commonly refers to a type of catenation in which a maximal displacement happens between the catenated frameworks. Interweaving is also a type of catenation where a minimal displacement occurs between the catenated frameworks.[278]

One can control the interpenetration of MOF by the rational design of the organic building blocks. In general, if big pores should be generated in a MOF that is synthesized from an extended organic building block, an interpenetrated framework often resulted, since nature prefers to form a compact structure and reduce the free space. A review by Batten and Robson introduces various types of interpenetrated networks.[279,280] Zhou et al. reported that catenation or noncatenation can be controlled by adding a template during the solvothermal synthesis. When oxalic acid was used as a template during the synthesis of MOF, a noncatenated framework was formed, while a catenated framework resulted in the absence oxalic acid.[243] Farha et al. have controlled the catenation of MOF by the rational design of the ligands. When they used a brominated ligand, a noncatenated framework was produced, while the use of a nonbrominated ligand yielded a catenated structure.[281] Zaworotko and co-workers controlled the interpenetration by adjusting the concentration and temperature in the synthesis. In the reaction of Cd^{2+} with 4,4′-bpy and BDC linkers, a noninterpenetrated framework was formed at low temperature and low concentration, while a doubly interpenetrated framework resulted at relatively high concentration and high temperature.[282] Fischer and co-workers reported that the catenation was controlled by liquid-phase epitaxy on an organic template.[283]

Catenation significantly affects the gas sorption properties. Zhou and co-workers compared the H_2 adsorption capacities of the MOFs that are chemically identical but with a catenated and noncatenated sturcture.[242,243] The catenated PCN-6 and noncatenated PCN-6′ have the general formula $Cu_3(TATB)_2$, and they were built from copper paddle-wheel units and 4,4′,4″-*s*-triazine-2,4,6-triyltribenzoate (TATB). The volumetric H_2 adsorption measurements for the samples activated at 50 °C showed that catenated PCN-6 adsorbed 1.74 wt %, while PCN-6′ adsorbed 1.35 wt % at 77 K and 1 atm. When the samples were activated at 150 °C the adsorption capacity increased slightly, PCN-6 to 1.9 wt % and PCN-6′ to 1.62 wt %. The larger improvement in H_2 adsorption of PCN-6′ was attributed the open metal sites. However, the open copper sites in PCN-6 were blocked because of the catenation, which leads to less improved H_2 adsorption. The catenated structures adsorb more H_2 gas than the noncatenated structures.

dx.doi.org/10.1021/cr200274s |*Chem. Rev.* 2012, 112, 782–835

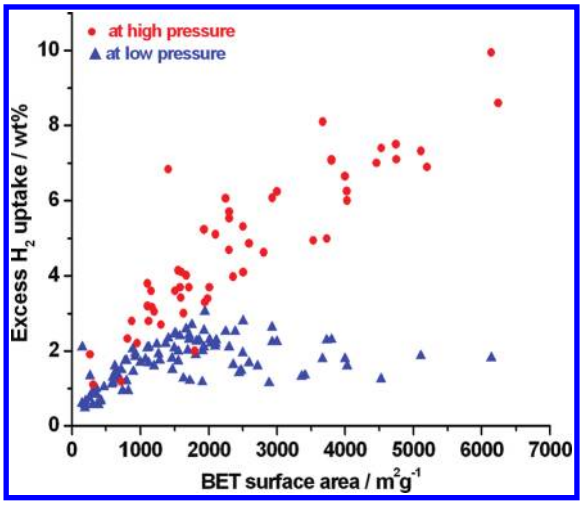

Figure 17. A plot showing the relationship between H_2 uptake capacities at 77 K and BET surface areas of various MOFs. Low pressure is 1 atm and high pressures are in the range of 10−90 bar.

The high pressure gas sorption data showed that the excess H_2 uptake of PCN-6 was 72 mg g^{-1} (6.7 wt %) at 77 K and 50 bar, while that of PCN-6′ is 42 mg g^{-1} (4.0 wt %). The total H_2 uptake capacity of PCN-6 was 95 mg g^{-1} (8.7 wt %) at 77 K and 50 bar and that of PCN-6′ was 58 mg g^{-1} (5.5 wt %). At 298 K and 50 bar, the excess H_2 adsorption capacities of PCN-6 and PCN-6′ were 9.3 mg g^{-1} (0.92 wt %) and 4.0 mg g^{-1} (0.40 wt %), and the total adsorption capacities were 15 mg g^{-1} (1.5 wt %) and 8.1 mg g^{-1} (0.80 wt %), respectively. At low coverage, PCN-6 (6.2−4.5 kJ mol^{-1}) and PCN-6′ (6.0−3.9 kJ mol^{-1}) have similar isosteric heats of the H_2 adsorption, but as the H_2 loading increases, catenated PCN-6 shows steadily higher H_2 adsorption enthalpies than those of PCN-6′. Inelastic neutron scattering measurement indicates that in both PCN-6 and PCN-6′, the first sites occupied by H_2 are the open metal sites, and as the H_2 loading increases, the interaction between H_2 molecules and the organic linkers becomes stronger in catenated PCN-6 than that in PCN-6′. These interesting results suggested that the catenation enhances H_2 uptake at room temperature.

Even though there was no direct comparison between the noncatenated and catenated frameworks, many catenated frameworks showed comparatively high H_2 uptake capacities. Long et al. employed two similar ligands, 1,3,5-tri-*p*-(tetrazol-5-yl)-phenylbenzene (H_3TPB-3tz) and 2,4,6-tri-*p*-(tetrazol-5-yl) phenyl-*s*-triazine (H_3TPT-3tz), to construct MOFs of Cu(II) and Mn(II), which afforded sodalite-type frameworks. The reaction of $CuCl_2 \cdot 2H_2O$ and H_3TPB-3tz yielded a noncatenated framework, $Cu_3[(Cu_4Cl)_3(TPB\text{-}3tz)_8]_2 \cdot 11CuCl_2 \cdot 8H_2O \cdot 120DMF$, while the reaction of $MnCl_2 \cdot 4H_2O$ and H_3TPT-3tz yielded the catenated framework $Mn_3[(Mn_4Cl)_3(TPT\text{-}3tz)_8]_2 \cdot 25H_2O \cdot 15CH_3OH \cdot 95DMF$. The activated sample of noncatenated Cu framework showed an H_2 uptake of 2.8 wt % at 77 K and 30 bar, while the catenated Mn framework showed a higher H_2 uptake of 3.7 wt % at 77 K and 25 bar with a total H_2 uptake of 4.5 wt % at 77 K and 80 bar. At 298 K, both of the frameworks showed comparable excess H_2 uptakes, 0.5 wt % at 68 bar. The isosteric heat of the noncatenated framework is 8.2 kJ mol^{-1}, and that of the catenated framework is 7.6 kJ mol^{-1}. The slightly higher isosteric heat in the noncatenated framework is attributed to the presence of exposed chloride anions of the $CuCl_2$ units.[113] The result indicates that not only the catenation but also the availability of exposed metal sites affects the hydrogen uptake properties.

It was also reported that $Zn_4O(dcdEt)_3$ and $Zn_4O(dcbBn)_3$ (dcdEt = 6,6′-dichloro-2,2′-diethoxy-1,1′-binaphthyl-4,4′-dibenzoate, dcbBn = 6,6′-dichloro-2,2′-dibenzyloxy-1,1′-binaphthyl-4,4′-dibenzoate), which have 4-fold interpenetrated structures, adsorb about 1.0 wt % of H_2 and 298 K and 48 bar due to the smaller pores that increased the H_2−host interactions.[216,284] Sometimes even if MOFs are highly interpenetrated, they show very low H_2 adsorption enthalpy. For example, the 3-fold interpenetrated 3D microporous MOFs $[Cu_3(4,4'\text{-bpy})_{1.5}(2,6\text{-NDC})_3]_n$ and $\{[Cu(bpe)_{0.5}(2,6\text{-NDC})] \cdot 0.5H_2O\}_n$ (bpe = 1,2-bis(4-pyridyl)ethane) have H_2 adsorption enthalpies of 3.7 and 4.5 kJ mol^{-1}, respectively. The Langmuir surface areas of the MOFs were very low due to the interpenetration, 113 m^2 g^{-1} and 337.5 m^2 g^{-1}, respectively. The frameworks show low H_2 uptake capacities at 77 K and 15 bar, 0.88 wt % for the former and 0.96 wt % for the latter.[285]

Despite the above examples, catenation may reduce the free volume and thus have a detrimental effect on the high pressure H_2 storage. Sometimes it even leads to nonporous structures. The positive effect of catenation and interpenetration on hydrogen storage is due to a strengthened framework and narrower pore size. Theoretical calculations predict that interpenetration is beneficial for hydrogen storage at low temperature and low pressure, but at ambient temperature, the adsorption capacity decreases significantly.[286]

4.1.3. Mixed Ligand System. As described in section 4.1.1, the elongation of the organic linker can increase the surface area and pore volume. However, the strategy has a considerable disadvantage of multistep organic synthesis. For example, the organic building block (H_6ttei) used in the synthesis of NU-100 or PCN-610 was prepared by a 10-step procedure.[28,266]

Another approach for the preparation of the porous materials is to combine two types of ligands within the same structure. In many previous reports, 2D layers are assembled from bimetallic tetracarboxylate paddle-wheel units $M_2(O_2CR)_4$, whose axial sites are linked with the linear ditopic nitrogen donor linkers to construct 3D primitive cubic MOFs. This strategy of constructing pillared structures can afford highly porous frameworks. For example, SNU-6 is a framework built from BPnDC, 4,4′-bpy, and Cu(II).[57] The solvent-accessible volume for this material is 83.7% with a BET (Langmuir) surface area of 2590 (2910) m^2 g^{-1}. The structure has very large pores with an effective size of 18.2 Å. The large pores result in modest H_2 uptake at 1 bar (1.68 wt % at 77 K) but high uptake at 70 bar (excess: 4.87 wt %, total: 10.0 wt %).

As mentioned in section 3.3, Matzger and co-workers provided an alternative strategy, which is coordination copolymerization of topologically different linkers with identical coordinating functionality.[118] $[Zn_4O(T^2DC)(BTB)_{4/3}]$ (UMCM-2) has BET and Langmuir surface areas of 5200 m^2 g^{-1} and 6060 m^2 g^{-1}, respectively, and its excess H_2 storage capacity is 68.8 mg g^{-1} at 77 K and 46 bar. Yaghi and co-workers also used mixed BTB/NDC and BTE/BPDC to obtain MOF-205 and MOF-210, respectively.[29] Activated MOF-205 and MOF-210 showed extraordinarily high BET (and Langmuir) surface areas, 4460 (6170) m^2 g^{-1} and 6240 (10400) m^2 g^{-1}, respectively. The BET surface area of MOF-210 is the highest reported so far for the crystalline materials. At 77 K, the excess and total H_2 uptake in MOF-210 are 86 mg g^{-1} at 56 bar and 176 mg g^{-1} at 80 bar, respectively, which are also the highest values at 77 K among data ever reported for physisorption materials.

It should be noted here that the high surface areas of MOFs synthesized by this coordination copolymerization do not come

dx.doi.org/10.1021/cr200274s |*Chem. Rev.* 2012, 112, 782–835

Table 3. Effect of Elongation of Ligands on the Gas Sorption Properties

tricarboxylate	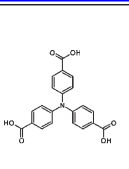	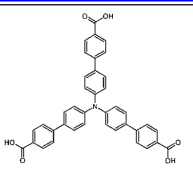	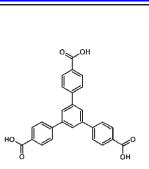	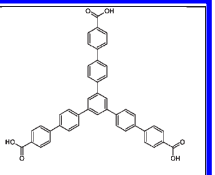	
metal	Zn^{II}				
topology	pyr	pyr	qom	qom	
MOFs	SNU-1	SNU-77	MOF-177	MOF-200	
surface area,[a] m^2g^{-1}	1121	4180 (3670)	5640 (4750)	10400 (4530)	
pore volume, cm^3g^{-1}	0.51	1.52	1.59	3.59	
tetracarboxylate	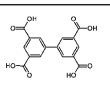	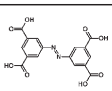	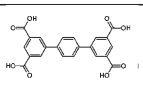	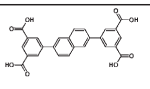	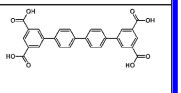
metal	Cu^{II}				
topology	NbO				
MOFs	NOTT-100	SNU-5'	NOTT-101	NOTT-103	NOTT-102
surface area,[a] m^2g^{-1}	(1640)	2850	(2316)	(2929)	(2942)
pore volume, cm^3g^{-1}	0.680	1.00	0.886	1.142	1.138
hexacarboxylate	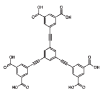	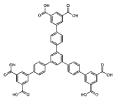	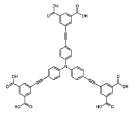	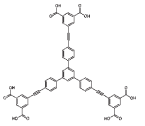	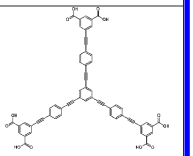
metal	Cu^{II}				
topology	rht				
MOFs	PCN-61	NOTT-112	PCN-66	PCN-68 NOTT-116	NU-100
surface area,[a] m^2g^{-1}	3500 (3000)	(3800)	4600 (4000)	6033 (5109)	6143
pore volume, cm^3g^{-1}	1.36	1.62	1.63	2.13	2.82

[a] Number in the parentheses is the BET surface area and the other is the Langmuir surface area.

from different chemical compositions of the ligands but from the novel framework topologies that are hard to achieve using only one ligand. In other words, using mixed carboxylate ligands will generate novel framework topology that may have huge porosity, independently of whether the ligands are O donors or N donors.

4.2. Increase in Isosteric Heat of Hydrogen Adsorption

Some MOFs with large surface areas meet the H_2 storage targets proposed by the U.S. Department of Energy (DOE), but only at cryogenic temperatures. None of the MOFs yet satisfy the targeted goals specified by the DOE in the United States for H_2 storage materials that should be developed by 2017. The materials should have at least 5.5 wt % of H_2 uptake ability for the whole system at moderate temperature and pressure. The main problem is that H_2 adsorption in MOFs is a physisorption, and the van der Waals interaction between H_2 and pore surface of MOFs is very weak. The H_2 uptake capacity at moderate temperatures falls down to less than 1/10 of the cryogenic value. To enhance the H_2 uptake at ambient temperature, strong adsorption sites should be incorporated into the pores. In addition, the pore surfaces/curvatures should be optimized for efficient H_2 packing.

As mentioned previously in section 4, Frost and Snurr have shown that the H_2 storage capacity at 298 K of a MOF can be

dx.doi.org/10.1021/cr200274s |*Chem. Rev.* 2012, 112, 782–835

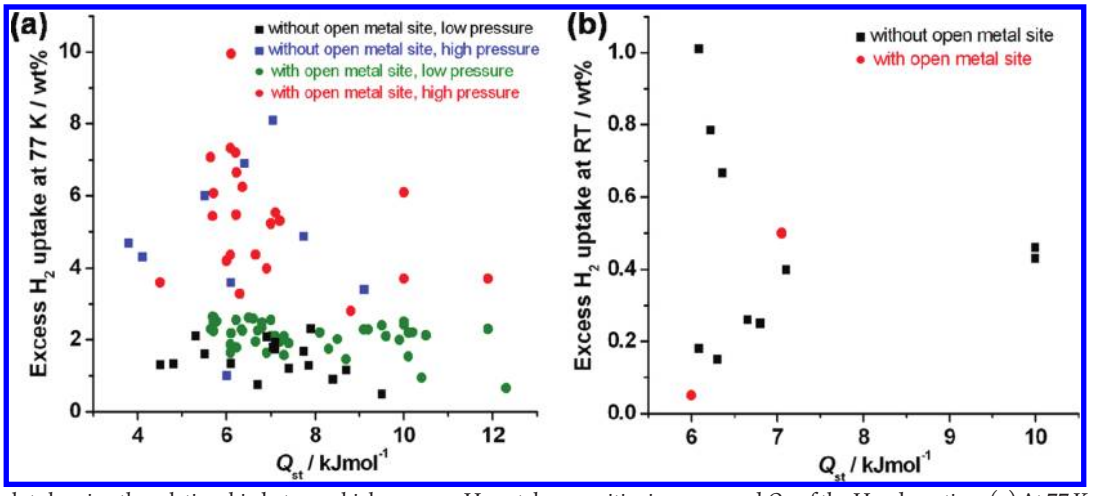

Figure 18. A plot showing the relationship between high pressure H_2 uptake capacities in excess and Q_{st} of the H_2 adsorption. (a) At 77 K. (b) At 298 K. Low pressure is 1 atm, and high pressures are in the range of 10−90 bar.

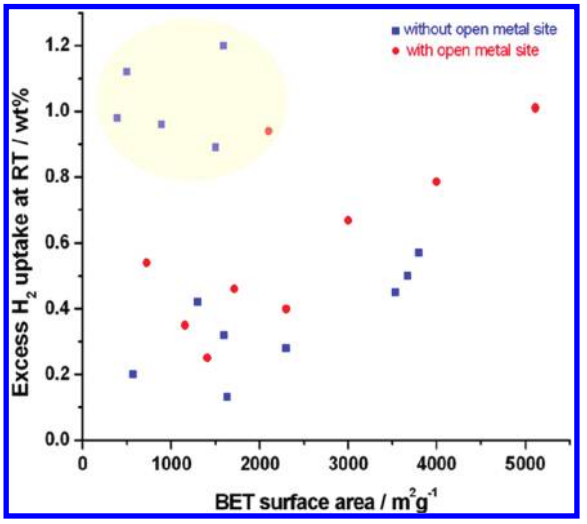

Figure 19. A plot of the room temperature H_2 uptake capacities vs BET surface areas of MOFs.

considerably increased at high pressures when the MOF has a high isosteric heat of H_2 adsorption, although big pore volume is the most important factor to achieve high H_2 adsorption capacity at high pressures.[172]

Recently, Bae and Snurr studied H_2 storage and delivery between 1.5−120 bar in a MOF. By using GCMC simulations, they estimated the optimal Q_{st} value for maximum H_2 delivery.[287] The deliverable capacity is the difference between the adsorbed amount of H_2 at high pressure and the adsorbed amount of H_2 at the discharge pressure (1.5 bar). The simulations demonstrated that the optimal Q_{st} is approximately 20 kJ mol^{-1}. However, Q_{st} of H_2 adsorption in most porous MOFs is in the range 5−9 kJ mol^{-1}.

Bhatia and Myers calculated that if the H_2 adsorption enthalpy is 6 kJ mol^{-1}, the optimal operating temperature of H_2 storage in microporous material is 131 K between 1.5 and 100 bar.[170] Therefore, to eliminate the need for a heavy and expensive cooling system, the H_2 affinity to MOFs should be increased. Various strategies have been made to increase the H_2 interactions with MOFs, such as creation of the open metal sites, introduction of cations generating strong electrostatic field within the cavities,

Table 4. Gas Sorption Data for HKUST-1

BET surface area, $m^2\ g^{-1}$	pore volume, $cm^3\ g^{-1}$	H_2 uptake, wt %	isosteric heat, kJ mol^{-1}	ref
1239	0.62	2.18[a]	6.1	202
1154		3.6,[b] 0.35[c]	4.5	210
1507	0.75	2.48[a]	6.8	61
1944		3.3[d]		62
	0.4	1.44[a]	6−7	183
		3.6[e]		289

[a] At 77 K and 1 bar. [b] At 77 K and 50 bar. [c] At 298 K and 65 bar. [d] At 77 K and 77 bar. [e] At 77 K and 10 bar.

doping with metal ions, fabrication of metal nanoparticles, and functionalization of the ligands that are exposed to the pores, which will be discussed in detail in the following sections.

In Figure 18, we have plotted reported data for the excess H_2 adsorption capacities of some MOFs at 77 and 298 K vs their Q_{st} values, to see if a relationship exists between them. As seen in Figure 18a, most of the MOFs have Q_{st} values in the range of 4−12 kJ mol^{-1}, and even if Q_{st} values are increased by several kJ mol^{-1}, they did not enhance the high pressure H_2 storage capacities at 77 K. However, at room temperature and high pressures (Figure 18b), there is a tendency that as the Q_{st} value increases, the excess H_2 adsorption capacity is increased, although there are not so many data for the statistics.

One of the reasons why there is no obvious relationship between hydrogen uptake capacities at 77 K and isosteric heats of hydrogen adsorption may be that the isosteric heats of H_2 adsorption represented are the low coverage data. When we refer to the impact of isosteric heat of adsorption, especially in the theoretical calculation study, we mean the average isosteric heat of adsorption instead of the one at very low hydrogen coverage. However, there is no commonly accepted method to determine the average isosteric heat of adsorption; almost all of the isosteric heats of adsorption reported so far are low coverage data.

4.2.1. Generation of Active Metal Sites in MOFs. On the basis of both experimental and computational studies, it has been shown that the coordinatively unsaturated metal centers ("open metal site", "exposed metal site", or "accessible metal site") enhance Q_{st} of the H_2 adsorption in a MOF because H_2

dx.doi.org/10.1021/cr200274s |Chem. Rev. 2012, 112, 782–835

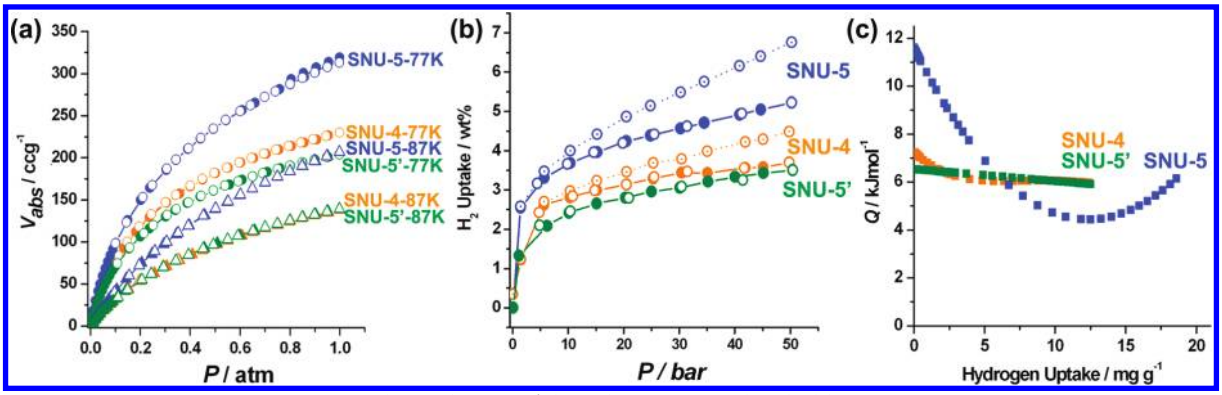

Figure 20. H_2 gas uptake properties of SNU-4 (orange), SNU-5′ (green), and SNU-5 (blue). (a) The H_2 adsorption isotherms measured at 77 K (circle) and 87 K (triangle) up to 1 atm of H_2. (b) Excess (solid line) and total (dotted line) H_2 adsorption isotherms at 77 K and high pressure. Filled shape: adsorption; open shape: desorption. (c) Isosteric heat of H_2 adsorption. SNU-4 and SNU-5′ have no accessible metal site, while SNU-5 has accessible metal sites. Reproduced with permission from ref 76. Copyright 2008 WILEY-VCH Verlag GmbH & Co. KGaA, Weinheim.

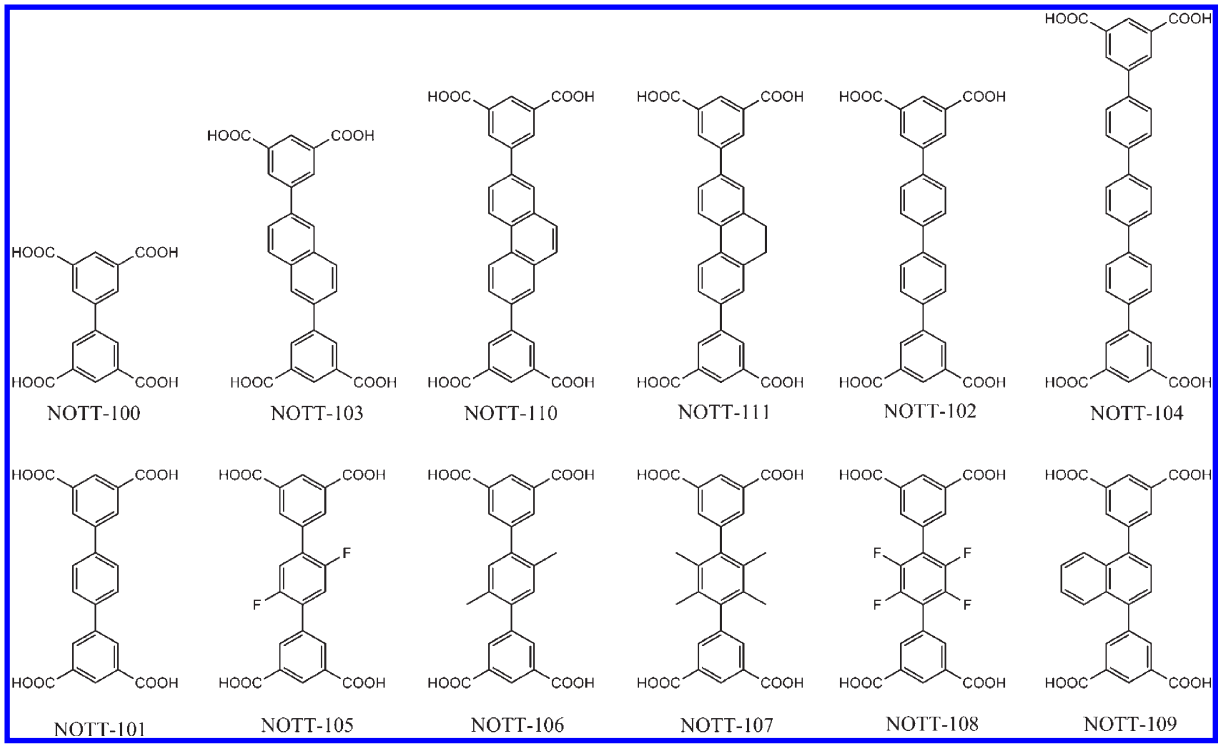

Figure 21. Various tetracarboxylic acids used in the synthesis of NOTT-series having NbO-net structure. NOTT-series generate open Cu(II) sites on activation.

molecules can directly interact with these sites. The metal−H_2 interactions in a MOF have been confirmed by neutron powder diffraction (NPD) experiments and inelastic neutron scattering (INS) spectroscopy.[48,275,288] The strategies for introducing open metal sites in the MOFs are the incorporation of metal clusters coordinating solvent molecules that are easily removable, the use of the metal building blocks that contain open metal sites, such as porphyrins, salens, etc., the attachment of organometallic complexes to the aromatic components of the struts,[70] and the electrostatic intercalation of metal complexes[112] or solvated (or unsolvated) metal cations in the anionic frameworks.[149]

In Figure 19, the excess H_2 uptake capacities at room temperature and high pressures are plotted against surface areas of various MOFs. The room temperature H_2 storage capacities of the MOFs with open metal sites are much higher than those without open metal sites, in particular when the surface areas are higher than 3000 $m^2 g^{-1}$. However, if the surface area is smaller than 3000 $m^2 g^{-1}$, the effect of the open metal sites on the room temperature H_2 storage capacities is rather minor. We will discuss the region marked by the yellow circle in Figure 19 in section 4.2.2.

4.2.1.1. Open Metal Sites at Secondary Building Units. The primary method for generating open metal sites consists of the synthesis of the MOF constructed of metal clusters coordinating solvent molecules as SBUs, which locate at the framework nodes, followed by removal of the coordinating solvent molecules by thermal evacuation. Most common SBUs for such purposes are the bimetallic paddle-wheel units of $M_2(O_2CR)_4$ (M = Cu^{2+}, Zn^{2+}, and Cd^{2+}), where solvent molecules are coordinated at the axial sites.

It was reported that open metal sites were generated in $[Cu_3(BTC)_2(H_2O)_3]_n$ (HKUST-1), which was constructed from benzene-1,3,5-tricarboxylate and Cu paddle-wheel SBUs.[73] The Langmuir and BET surface areas were 917.6 $m^2 g^{-1}$ and

dx.doi.org/10.1021/cr200274s |*Chem. Rev.* 2012, 112, 782–835

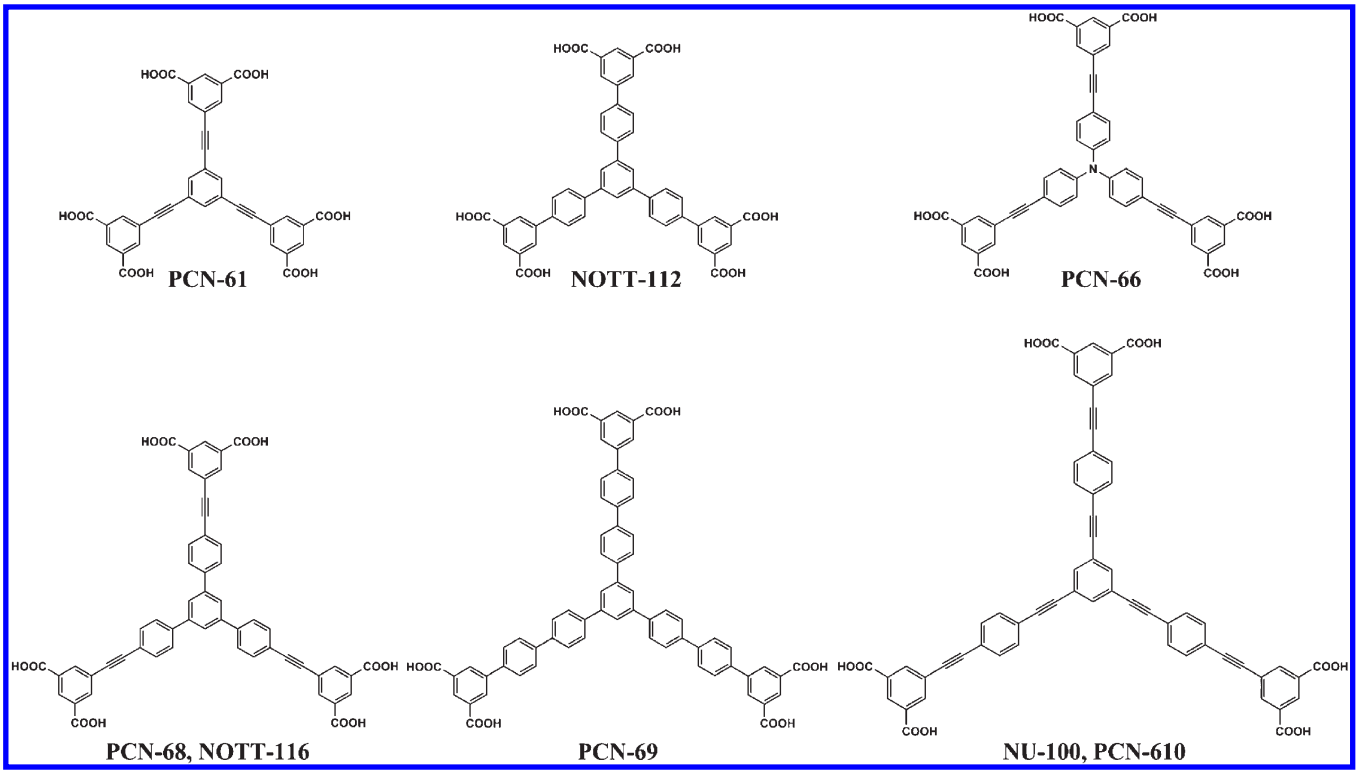

Figure 22. Various hexacarboxylic acid ligands used in the synthesis of polyhedral frameworks.

692.2 $m^2 g^{-1}$, respectively, with a total pore volume of 0.333 $cm^3 g^{-1}$. However, many other research groups later reported different values of the surface area, pore volume, H_2 storage capacity, and H_2 adsorption enthalpy, which are summarized in Table 4. We assume that the activation method, handling of the activated sample containing open metal sites, and method of gas sorption measurements might cause these differences. For example, Kaskel and coworkers have reported that the use of new pressure free synthesis, which means refluxing copper acetate and H_3BTC in DMF without sealing the reaction vessel during the synthesis, and by avoiding the nitrate precursor, produced better quality product without any impurities.[202] The new synthetic method led to greater micropore volume of 0.62 $cm^3 g^{-1}$ compared to a previous report of 0.41 $cm^3 g^{-1}$. This suggests that we have to be very careful in handling the activated MOFs that contain open metal sites in order to obtain the data that can be reproducible.

Suh's group made a comparison of the H_2 storage capacities for three isostructural MOFs with and without open metal sites. $[\{Zn_2(abtc)(dmf)_2\}_3]$ (SNU-4) and $[\{Cu_2(abtc)(dmf)_2\}_3]$ (SNU-5′) have no open metal site, whereas $[\{Cu_2(abtc)\}_3]$ (SNU-5) has open metal sites (abtc = 1,1′-azobenzene-3,3′,5,5′-tetracarboxylate).[76] The available surface area and pore volume in SNU-5 having open metal sites are 1.4−1.7 times greater than those of SNU-4 and SNU-5′. Furthermore, the H_2 sorption capacities of SNU-5 are much higher than those of SNU-4 and SNU-5′; at 77 K and 1 atm, the H_2 uptake capacities are 2.07 wt % for SNU-4, 1.83 wt % for SNU-5′, and 2.87 wt % for SNU-5. At 77 K and 50 bar, the excess adsorption capacities of SNU-4 and SNU-5 are 3.70 wt % and 5.22 wt %, respectively, with the total adsorption capacities of 4.49 wt % and 6.76 wt % (Figure 20). To exclude the reduced mass effect for the sample without coordinated solvent molecules, the H_2 adsorption capacities per volume of the MOFs were also compared, which still indicated that the MOF with open metal sites adsorbed a higher amount of H_2 gas (120%). The isosteric heats of H_2 adsorption for SNU-4, SNU-5′, and SNU-5 were 5.96−7.24, 5.91−6.53, and 4.43−11.60 kJ mol^{-1} respectively. The zero coverage isosteric heat of H_2 adsorption for SNU-5, 11.6 kJ mol^{-1}, is one of the highest values reported so far. However, the room temperature H_2 uptake capacity of SNU-5 is still not so satisfactory, 0.5 wt % at 100 bar. These results suggest that the presence of open metal sites in a MOF leads to the higher H_2 uptake capacity and higher isosteric heat of H_2 adsorption as well as a higher surface area and pore volume.

Similarly, Zhou et al. reported that alignment of open metal sites affects the H_2 adsorption. PCN-12 ($[Cu_6(C_s\text{-mdip})_2(C_{2v}\text{-mdip})(H_2O)_6]\cdot 3DMA\cdot 6H_2O$) and PCN-12′ ($[Cu_2(C_{2v}\text{-mdip})(H_2O)_2]\cdot 3DMSO$) are polymorphs formed from the Cu paddlewheel SBUs and 5,5′-methylenediisophthalate (mdip).[253] The polymorphism occurred due to two extreme conformations, one in C_s and the other in C_{2v} symmetry. The structure consists of cuboctahedra, and in PCN-12 the open metal sites are aligned while in PCN-12′ the open metal sites are out of alignment. The dissimilar alignments of open metal sites significantly affected the hydrogen uptakes of these MOFs. The Langmuir surface areas of PCN-12 and PCN-12′ are 2425 and 1962 $m^2 g^{-1}$, and the pore volumes are 0.94 mL g^{-1} and 0.73 mL g^{-1}, respectively. The H_2 uptake capacities of PCN-12 and PCN-12′ are 3.05 wt % and 2.40 wt %, respectively, at 77 K and 1 atm. The inelastic neutron scattering spectrum of PCN-12 indicates that H_2 strongly prefers available Cu sites to other binding sites.

PCN-10 $\{Cu_2(abtc)(H_2O)_2\cdot 3DMA\}$ and PCN-11 $\{Cu_2(sbtc)(H_2O)_2\cdot 3DMA\}$, which are synthesized from azoxybenzene-3,3′,5,5′-tetracarboxylic acid (H_4azobtc) and *trans*-stilbene-3,3′,5,5′-tetracarboxylic acid (H_4sbtc), respectively, with Cu(II) paddlewheel SBUs, are isostructural porous MOFs.[252] Both frameworks contain nanoscopic cages and generate coordinatively unsaturated metal centers on activation. PCN-10 and PCN-11 have Langmuir

dx.doi.org/10.1021/cr200274s |*Chem. Rev.* 2012, 112, 782–835

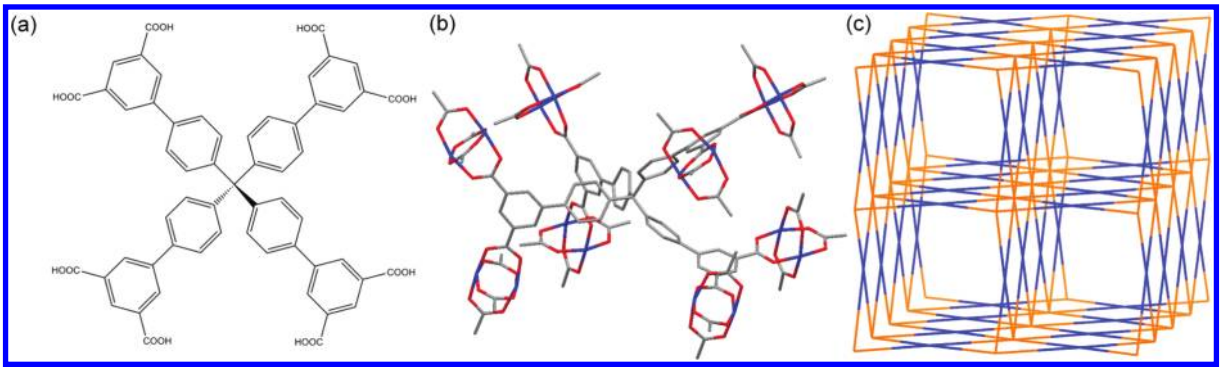

Figure 23. NOTT-140.[270] (a) Octacarboxylic acid employed in the synthesis, (b) connectivity of L^{8-} with eight Cu paddle-wheel units, and (c) (4,8)-connected scu topology of the framework.

surface areas of 1779 and 2442 $m^2\ g^{-1}$ with total pore volumes of 0.67 and 0.91 $cm^3\ g^{-1}$, respectively. At 77 K and 1 atm, PCN-10 shows a H_2 uptake capacity of 2.34 wt %, while PCN-11 shows a capacity of 2.55 wt %. The high pressure adsorption isotherms at 77 K show that the H_2 uptakes reach saturation at 20 atm, and the excess uptake capacities of PCN-10 and PCN-11 are 4.33 wt % and 5.05 wt %, respectively. This suggests that MOF with N═N double bonds has a slightly higher H_2 affinity than corresponding MOF with C═C double bonds.

A series of MOFs (NOTT-100−NOTT-111) were constructed from Cu(II) paddle-wheel SBUs and long tetracarboxylic acids (Figure 21).[75,250,251] On activation, all of them have similar structures and stoichiometry, except NOTT-104, which forms an interpenetrated structure and is unstable to desolvation. All MOFs show high H_2 uptake capacities due to the large pore volumes as well as the presence of copper open metal sites. The neutron powder diffraction data indicate that the open Cu(II) sites are the strongest adsorption sites in the pores, but the heat of H_2 adsorption is very similar in all sites in a MOF. In the series of MOFs, the heat of H_2 adsorption is affected by the ligand structure near the paddle-wheel SBUs. The high heat of adsorption at low H_2 loading was observed for NOTT-106 and NOTT-107, and it is due to the exposed Cu(II) sites as well as methyl groups exposed to the pores. The MOFs with functionalized pores with fluorine and methyl groups have lower pore volumes and lower H_2 capacities, and the heat of adsorption drops rapidly with increasing H_2 loading. The naphthalene ring in NOTT-103, and the phenanthrene group in NOTT-110 have a positive effect on the H_2 uptake, which may be due to the presence of a large aromatic surface.

The MOFs formed from hexacarboxylic acids and Cu paddle-wheel units are an interesting class of compounds. In these MOFs, large cavities are formed in the fused polyhedral frameworks (Figure 22). For example, NOTT-112, $[Cu_3(L)(H_2O)_3]\cdot 8DMSO\cdot 15DMF\cdot 3H_2O$, was constructed from 1,3,5-tris(3′,5′-dicarboxy[1,1′-biphenyl]-4-yl)benzene (L) and copper paddle-wheel SBUs, and it shows high H_2 uptake capacity.[268] The BET surface area of NOTT-112 was 3800 $m^2\ g^{-1}$, and the total pore volumes calculated from the N_2 and Ar isotherms were 1.62 $cm^3\ g^{-1}$ and 1.69 $cm^3\ g^{-1}$, respectively. It adsorbs 2.3 wt % of H_2 at 78 K and 1 bar. The high H_2 adsorption capacity at low pressure is attributed to the presence of exposed Cu(II) centers and the presence of the relatively small cages. The isosteric heat of H_2 adsorption is 5.64−4.74 kJ mol^{-1}. At high pressure, the excess H_2 uptake of NOTT-112 was 7.07 wt % at 35−40 bar, and the total uptake was 10.0 wt % at 77 bar. The high H_2 uptake is attributed to the high surface and large pore volume along with the presence of polyaromatic ligands.[290] NOTT-116, $[Cu_3(ptei)(H_2O)_3]\cdot 16DMF\cdot 26H_2O$, also shows high H_2 uptake, which was constructed from (5,5′-((5′-(4-((3,5-dicarboxyphenyl)ethynyl)phenyl)-[1,1′:3′,1″-terphenyl]-4,4″-diyl)-bis(ethyne-2,1-diyl))diisophthalic acid = H_6ptei) and copper paddle-wheel SBUs. The desolvated NOTT-116 contains open metal sites, and its apparent BET surface area is 4664 $m^2\ g^{-1}$. The framework has big pores with a pore-size distribution around 1.6, 2.0, and 2.6 nm. The total pore volume calculated from the Ar sorption isotherm is 2.17 $cm^3\ g^{-1}$, which is extraordinarily high for a porous MOF material. NOTT-116 adsorbs 1.9 wt % of H_2 at 78 K and 1 bar, and the isosteric heat of the H_2 adsorption is 6.7 kJ mol^{-1} at zero coverage. The high pressure volumetric H_2 sorption isotherm of desolvated NOTT-116 indicates an excess H_2 uptake capacity of 6.4 wt % at 77 K and 27 bar with the total uptake amounts of 9.2 wt % at 50 bar, which is lower than that of NOTT-112. This indicates that for mesoporous materials, a higher internal surface area and higher pore volume do not guarantee the higher H_2 adsorption capacity.[275]

NU-100 having the formula $[Cu_3(ttei)(H_2O)_3]_n$ was prepared from 1,3,5-tris[(1,3-carboxylic acid-5-(4-(ethynyl)phenyl))ethynyl]-benzene (H_6ttei) and copper paddle-wheel SBUs, which forms a noncatenated structure. Because of the elongated ligand and open Cu(II) sites in NU-100, BET surface area of activated NU-100 was 6143 $m^2\ g^{-1}$ and the total pore volume of NU-100 was 2.82 $cm^3\ g^{-1}$. The excess hydrogen uptake of NU-100 was 18.2 mg g^{-1} at 1 bar and 99.5 mg g^{-1} at 56 bar and at 77 K, with the total H_2 uptake of 164 mg g^{-1} at 70 bar and 77 K. The isosteric heat of H_2 adsorption is 6.1 kJ mol^{-1} at low loading.[28]

Zhou et al. have reported a series of isostructural MOFs, which were synthesized from dendritic hexacarboxylate ligands and copper paddle-wheel SBUs, namely, PCN-61 (5,5′,5″-benzene-1,3,5-triyltris(1-ethynyl-2-isophthalate), btei), PCN-66 (5,5′,5″-(4,4′,4″-nitrilotris(benzene-4,1-diyl)tris(ethyne-2,1-diyl))triisophthalate, ntei), PCN-68, H_6ptei), PCN-610 H_6ttei), and PCN-69 (5,5′,5″-(benzene-1,3,5-triyl-tris(biphenyl-4,4′-diyl)) triisophthalic acid, H_6btti).[265,267] On evacuation at 100 °C, the PCN series generate open Cu(II) sites. Among the desolvated PCNs, PCN-61, PCN-66, PCN-68, and PCN-69 showed remarkably high surface areas and H_2 uptake capacities, while PCN-610 was unstable on evacuation. At 77 K, the pressure of maximum H_2 adsorption increases from PCN-61 to PCN-68, coincident with the increase of the surface area, and the total H_2

dx.doi.org/10.1021/cr200274s |Chem. Rev. 2012, 112, 782–835

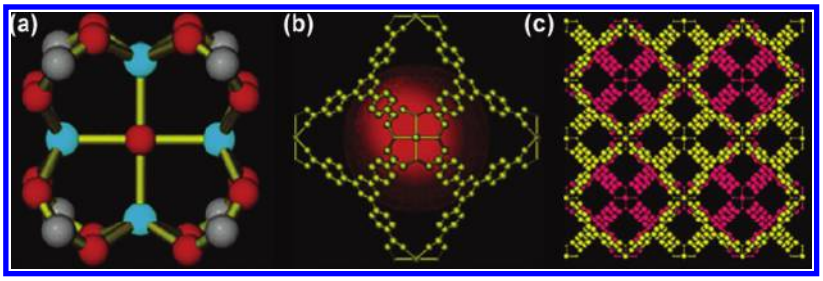

Figure 24. (a) The $Co_4(\mu_4\text{-O})(\text{carboxylate})_4$ SBU in PCN-9. Color scheme: C, gray; Co, aqua; and O, red. (b) Crystal structure of PCN-9 showing an octahedral cage; the red sphere represents void inside the cage. (c) View of the crystal structure of PCN-9 along the *a*-axis; the two interpenetrated networks are shown in gold and pink, respectively. All atoms are shown in arbitrary scales. Figure was adapted from ref 88. Copyright 2006 American Chemical Society.

uptake capacity reaches to 130 mg g^{-1} for PCN-68, which is one of the high gravimetric hydrogen uptake capacities reported so far. However, these frameworks have relatively low isosteric heats of H_2 adsorption at zero coverage, 6.36, 6.22, and 6.09 kJ mol^{-1} for PCN-61, PCN-66, and PCN-68, respectively, despite the presence of open Cu(II) sites. Even though the surface area of PCN-69 is greater than PCN-61, its H_2 uptake capacity is smaller than any of the series. However, PCN-69 shows a slightly higher isosteric heat (8.14 kJ mol^{-1}) at zero coverage because of the bent ligand creating pockets and concaves in the pores, which increases the interaction between the H_2 and host.

UTSA-20, $[Cu_3(BHB)(H_2O)_3]\cdot 6DMF\cdot 2.5H_2O$, was constructed from 3,3′,3″,5,5′,5″-benzene-1,3,5-triyl-hexabenzoic acid (BHB) and paddle-wheel type $Cu_2(COO)_4$ SBUs. Unlike the other MOFs, which are all based on the same 3,24-connected network, USTA-20 has a completely different structure of zyg topology.[264] The desolvated MOF has open Cu sites. It has a BET surface area of 1156 m^2 g^{-1} and H_2 uptake capacity of 2.9 wt % at 77 K and 1 bar. The high pressure adsorption isotherm shows excess H_2 uptake capacity of 4.1 wt % at 77 K and 15 bar, and this rather low uptake capacity must be due to the low surface area.

NOTT-140, $[Cu_4L(H_2O)_4]\cdot 10DMF\cdot C_4H_8O_2\cdot 8H_2O$, was constructed from copper paddle-wheel SBUs and octacarboxylic acid (4′,4‴,4⁗,4⁗⁗-methanetetrayltetrakis(([1,1′-biphenyl]-3,5-dicarboxylic acid))), which forms a 4,8-connected network comprised of octahedral and cuboctahedral cages (Figure 23).[270] The desolvated framework contains exposed Cu sites and shows total H_2 uptake capacity of 6.0 wt % at 20 bar at 77 K. The isosteric heat of H_2 adsorption was 4.15 kJ mol^{-1} at zero surface coverage. The relatively low isosteric heat is due to the different alignment of the vacant Cu sites. Contrary to other NOTT series that have the exposed Cu sites in the pores of the cages, NOTT-140 has the Cu sites that locate outside the cages, which results in reduced affinity for H_2.

The highest Q_{st} value of MOFs reported so far is 15 kJ mol^{-1} for $[Co^{II}_4(\mu\text{-}OH_2)_4(MTB)_2]_n$ (SNU-15′) prepared by heating of $[Co^{II}_4(\mu\text{-}OH_2)_4(MTB)_2(H_2O)_4]_n\cdot 13n\text{DMF}\cdot 11nH_2O$ (SNU-15) at 220 °C under a vacuum for 24 h.[168] SNU-15 has fluorite-like network generating 3D channels. In the as-synthesized MOF, each Co(II) ion coordinates terminal aqua ligand, and Co−Co distances are 3.550 Å and 3.428 Å. During the activation process, the coordinated water molecules were removed and the vacant coordination sites were created on every Co^{II} ion. The extraordinarily high isosteric heat of H_2 adsorption in SNU-15 might be attributed to the Co−Co distance that makes it possible for a H_2 molecule to bind in a side-on fashion.

An oxo-centered trigonal $[M_3(\mu_3\text{-O})(COO)_6]$ unit (M = Cr^{3+}, Al^{3+}, $Fe^{2+/3+}$, Ni^{2+}, and In^{3+}) is the one of the most common carboxylate-bridged clusters. Every metal ion in $[M_3(\mu_3\text{-O})(COO)_6]$ unit displays one potential open metal site. Férey and co-workers reported the H_2 sorption properties of metal-BDC M(OH)(BDC) containing Cr(III) and Al(III), denoted as MIL-53 (MIL = material from Institute Lavoisier), which are well-known as material exhibiting the breathing phenomenon upon guest removal and reintroduction.[176] The structure is formed of infinite *trans* corner-sharing octahedral $MO_4(OH)_2$ chains linked with each other through the BDC molecules to generate 1D lozenge-shape tunnels with a pore size of 8.5 Å. At 77 K under 1.6 MPa, MIL-53(Cr) shows a maximum H_2 adsorption capacity of 3.1 wt %, whereas MIL-53(Al) exhibits 3.8 wt % at the same pressure. The BET surface areas are 1020 m^2 g^{-1} and 1026 m^2 g^{-1} for MIL-53 (Al) and MIL-53 (Cr), respectively.

Two chromium carboxylate MOFs, $Cr_3OF(BTC)_2$ (MIL-100) and $Cr_3OF(BDC)_3$ (MIL-101) have totally different topologies from MIL-53.[84] They contain trimeric chromium(III) octahedral clusters coordinating removable terminal water molecules and thus provide potentially unsaturated metal sites. The resulting zeotype architectures were built by the connection of large hybrid supertetrahedron and generated very large mesopores. After removal of the guests, the accessible pore diameters are 25 and 29 Å for MIL-100, and 29 and 34 Å for MIL-101. Desolvated MIL-100 prepared by evacuating at 220 °C showed a Langmuir surface area of 2700 m^2 g^{-1} and a maximum H_2 uptake of 3.28 wt % at 77 K and 26.5 bar and 0.15 wt % at 298 K and 73 bar. In the case of MIL-101, two different treatments were applied to afford MIL-101a with H_2BDC and MIL-101b without H_2BDC in the pores. For MIL-101a, the Langmuir surface was 4000 m^2 g^{-1}, and maximum H_2 adsorption capacities were 4.5 wt % at 77 K and 40 bar and 0.36 wt % at 298 K and 86 bar. For MIL-101b, the Langmuir surface was 5500 m^2 g^{-1}, and maximum H_2 adsorption capacities were 6.1 wt % at 77 K and 80 bar and 0.43 wt % at 298 K and 86 bar. Furthermore, MIL-101b has high heat of H_2 adsorption (9.3−10.0 kJ mol^{-1}) at low coverage, which is larger than that (5.6−6.3 kJ mol^{-1}) of MIL-100. The high isosteric heat of H_2 adsorption in MIL-101b was explained by the presence of strong adsorption sites within the microporous supertetrahedra (ST), probably at each corner close to the trimers of chromium octahedra.

The cubic structure of $[In_3O(abtc)_{1.5}(H_2O)_3](NO_3)$ is built from trimers of corner-sharing octahedrally coordinated indium centers linked by abtc organic linkers.[85] The trimers contain three $[InO_5(H_2O)]$ octahedra sharing one central μ_3-oxo anion located on a 3-fold axis. In each octahedron, the apical position is occupied by a terminal water molecule, which can be

dx.doi.org/10.1021/cr200274s |*Chem. Rev.* 2012, 112, 782–835

Table 5. The H_2 Adsorption Data for DMA-*rho*-ZMOF, Mg-*rho*-ZMOF, and Li-*rho*-ZMOF[149,292]

	DMA-*rho*-ZMOF	Mg-*rho*-ZMOF	Li-*rho*-ZMOF
H_2 uptake at 78 K and 0.95 atm, wt %	0.95	0.91	0.91
adsorbed H_2 (mol)/In atom	2.21	2.21	2.28
heat of adsorption, kJ mol^{-1}	8	9	9.1

Table 6. Compositions and Gas Sorption Properties of Cation-Exchanged Mn(II) Framework[112]

exchanged metal ion	formula[a]	M/Mn ratio	H_2 ads, wt %[b]	Q_{st}, kJ mol^{-1}[c]
	$Mn_3[(Mn_4Cl)_3(BTT)_8]_2$	N/A	2.23	10.1−5.5
Li^+	$Li_{3.2}Mn_{1.4}[(Mn_4Cl)_3(BTT)_8]_2\cdot 0.4LiCl$	0.017	2.06	8.9−5.4
Cu^+	$Mn_3[(Mn_4Cl)_3(BTT)_8]_2\cdot 0.75CuPF_6$	N/A	2.00	9.9−5.6
Fe^{2+}	$Fe_3[(Mn_4Cl)_3(BTT)_8]_2\cdot FeCl_2$	0.17	2.21	10.2−5.5
Co^{2+}	$Co_3[(Mn_4Cl)_3(BTT)_8]_2\cdot 1.7CoCl_2$	0.21	2.12	10.5−5.6
Ni^{2+}	$Ni_{2.75}Mn_{0.25}[(Mn_4Cl)_3(BTT)_8]_2$	0.121	2.29	9.1−5.2
Cu^{2+}	$Cu_3[(Cu_{2.9}Mn_{1.1}Cl)_3(BTT)_8]_2\cdot 2CuCl_2$	3.999	2.02	8.5−6.0
Zn^{2+}	$Zn_3[(Zn_{0.7}Mn_{3.3}Cl)_3(BTT)_8]_2\cdot 2ZnCl_2$	0.546	2.1	9.6−5.5

[a] Based on the relative ratio of M^{n+}/Mn^{2+}. [b] Measured at 77 K and 900 Torr. [c] Obtained by using a virial fit to the H_2 adsorption isotherms at 77 and 87 K.

removed by activation. Each trimer unit is linked by six separate organic linkers to produce a novel 3D structure having *soc* topology. The Langmuir surface area and pore volume of desolvated sample are 1417 $m^2\ g^{-1}$ and 0.50 $cm^3\ g^{-1}$, respectively. It adsorbs high amounts of H_2 gas, up to 2.61 wt % at 78 K and 1.2 atm and shows the invariable isosteric heat (6.5 kJ mol^{-1}) of the H_2 adsorption up to 1.8 wt % of loading, which indicates the homogeneity of the sorption sites up to this experimental loading (ca. 70% of the full loading of 2.61 wt % H_2 at 78 K and 1.2 atm). This result suggests the potential effects of open metal site, framework charge, and pore dimension on the energetics of sorbed H_2 molecules in MOFs.

Among heterocyclic azolate-based frameworks, Mn-BTT, $Mn_3[(Mn_4Cl)_3(BTT)_8(CH_3OH)_{10}]_2$, exhibited the highest surface area, H_2 uptake capacity, and isosteric heat of H_2 adsorption.[48] The X-ray crystal structure indicates that the chloride-centered square-planar $[Mn_4Cl]^{7+}$ units are linked with eight trigonal planar BTT^{3-} ligands to form the anionic, three-dimensional sodalite-type framework. The solvent molecules occupy the sixth coordination site on each Mn^{2+} ion, while charge balance is provided by Mn complexes. The desolvated Mn-BTT, which contains open metal sites, exhibited a BET surface area of 2100 $m^2\ g^{-1}$, excess (total) H_2 adsorption capacity of 5.1 wt % (6.9 wt %) at 77 K and 90 bar, and high zero-coverage isosteric heat of H_2 adsorption, 10.1 kJ mol^{-1}. On the contrary, $[Mn(DMF)_6]_3[(Mn_4Cl)_3(BTT)_8(DMF)_{12}]_2$, which is the isomorphous framework where all Mn^{2+} ions are coordinatively saturated with DMF molecules shows much lower zero-coverage enthalpy of H_2 adsorption, 7.6 kJ mol^{-1}. It adsorbs only total 3.9 wt % of H_2 at 77 K and 50 bar. These values indicate strong H_2 adsorption sites are available in Mn-BTT, which do not exist in $[Mn(DMF)_6]_3[(Mn_4Cl)_3(BTT)_8(DMF)_{12}]_2$. The neutron powder diffraction study reveals that this is directly related to H_2 binding at coordinatively unsaturated Mn^{2+} centers with a distance of 2.27 Å. The isostructural sodalite frameworks, $HCu[(Cu_4Cl)_3(BTT)_8]\cdot 3.5HCl$ (Cu-BTT)[273] and $Fe_3[(Fe_4Cl)_3(BTT)_8(MeOH)_4]_2$ (Fe-BTT),[271] also showed high zero-coverage H_2 binding enthalpy, 9.5 and 11.9 kJ mol^{-1}, respectively. The strongest binding site is located just 2.47 and 2.17 Å away from the exposed Cu^{2+} and Fe^{2+} metal sites, respectively.

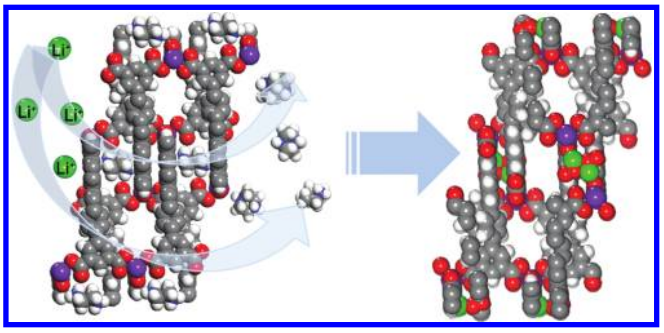

Figure 25. The X-ray structures of NOTT-200 (left) and NOTT-201 (right).[87] The H_2ppz^{2+} dications in the channel B of NOTT-200 can be completely exchanged with Li^+ ions in the channel C of NOTT-201. Color code: In, violet; Li, green; C, gray; N, blue; O, red; H, white.

$[Cu_6O(TZI)_3(H_2O)_9(NO_3)]$ (TZI = 5-tetrazolylisophthalate is a unique example consisting of two different types of metal clusters.[124] The X-ray crystal structure revealed the framework was constructed from truncated cuboctahedra (24 functionalized isophthalate ligands connected by 12 copper dimer centers, $[Cu_2(O_2CR)_4]$ paddle-wheels) connected to trigonal $Cu_3O(N_4CR)_3$ trimers through each tetrazolate (N_4CR) moiety. As mentioned previously, the solvent molecules are coordinated to the axial sites of each paddle-wheel unit. Each copper atom of $Cu_3O(N_4CR)_3$ trimer is coordinated to two nitrogen atoms (one from each of two tetrazolates), an oxygen (oxo) core, two oxygen atoms of two different equatorial water molecules to give square pyramidal geometry. The Langmuir (BET) surface area is 3223 (2847) $m^2\ g^{-1}$ and the total pore volume is 1.01 $cm^3\ g^{-1}$. H_2 capacity is up to 2.4 wt % at 77 K and 1 atm with the isosteric heat of 9.5 kJ mol^{-1} at the lowest coverage.

Another approach for generating the open metal sites is synthesis of MOF with entatic metal centers (EMCs). In contrast to the examples discussed above, the EMCs have the potential to bind the substrate without ligand removal. Ma and Zhou reported

dx.doi.org/10.1021/cr200274s |*Chem. Rev.* 2012, 112, 782–835

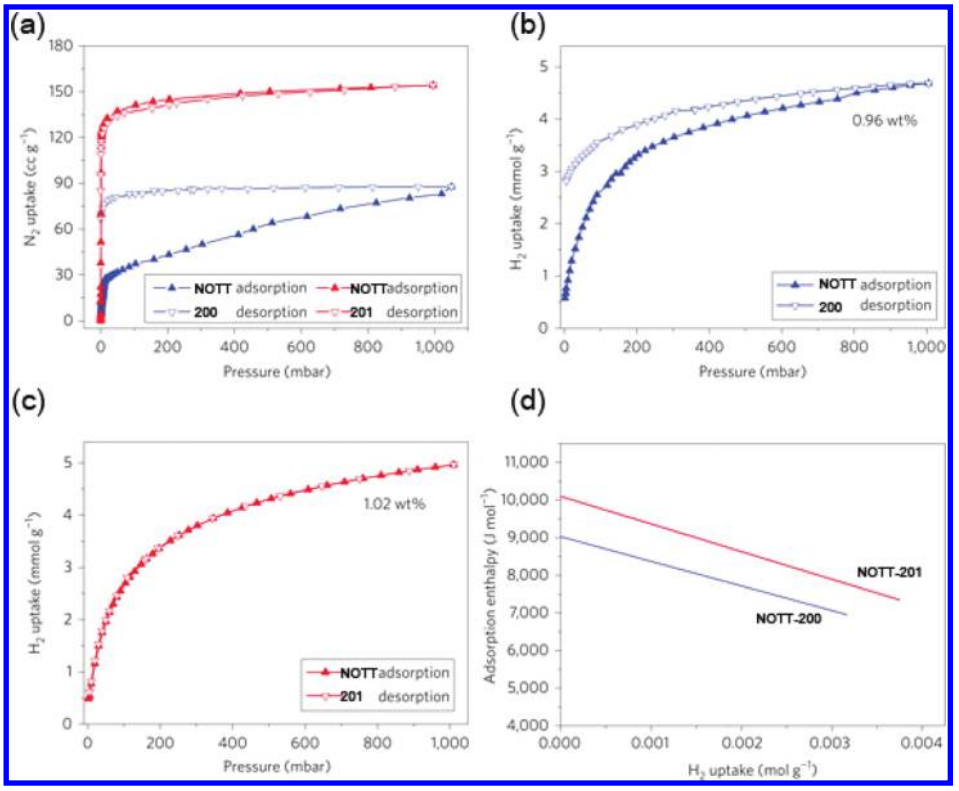

Figure 26. Gas adsorption isotherms of NOTT-200 and NOTT-201. (a) N_2 at 78 K. (b) H_2 for NOTT-200 at 78 K up to 1 bar. (c) H_2 for NOTT-201 at 78 K up to 1 bar. (d) Enthalpies of H_2 adsorption at low surface coverage. Reproduced with permission from ref 87. Copyright 2009 Macmillan Publishers Limited.

an MOF with EMCs, $H_2[Co_4O(TATB)_{8/3}]$, designated as PCN-9 (TATB = 4,4′,4″-*s*-triazine-2,4,6-triyltribenzoate, PCN = porous coordination network).[88] It adopts a square-planar $Co_4(\mu_4\text{-O})$ SBU, with a μ_4-oxo residing at the center of four Co atoms (Figure 24). All four Co atoms in the SBU are five-coordinate with square-pyramidal geometry, and the position below the square-plane formed of the four O atoms is in an entatic state and ready to bind a substrate to achieve octahedral coordination. The square-planar μ_4-oxo bridge found in PCN-9 is unique in a MOF. After desolvation, PCN-9 exhibits a Langmuir surface area of 1355 $m^2\ g^{-1}$ and a pore volume of 0.51 $cm^3\ g^{-1}$. The H_2 adsorption isotherm at 77 K indicates that PCN-9 has an uptake of 1.53 wt % at 1 atm. At low coverage, the heat of adsorption of PCN-9 for H_2 is 10.1 kJ mol^{-1}.

All H_2 adsorption data for the MOFs having open metal sites are summarized in Table 2. According to the collected data for the MOFs having open metal sites, the highest zero coverage isosteric heat of H_2 adsorption is 15 kJ mol^{-1} for SNU-15[168] and the next highest is 12.3 kJ mol^{-1} for $[Zn_3(BDC)_3(Cu(pyen))]$ (pyen = 5-methyl-4-oxo-1,4-dihydropyridine-3-carbaldehyde),[235] and the lowest is 4.15 kJ mol^{-1} for NOTT-140.[270] For all MOFs having open metal sites reported so far, the average value of isosteric heats of H_2 adsorption is 7.8 kJ mol^{-1} according to our calculation. These are greater than the values for the MOFs without open metal sites, in which the average value of isosteric heats of H_2 adsorption is 6.8 kJ mol^{-1}. Among all MOFs without open metal sites reported so far, the highest isosteric heat of H_2 adsorption is 9.5 kJ mol^{-1} for $Mg_3(NDC)_3$,[291] and the lowest is 3.8 kJ mol^{-1} for MOF-5.[210]

4.2.1.2. Introduction of Metal Ions in the Pores. As discussed in the previous section, in order to increase hydrogen storage capacity at ambient temperature, the interaction energy between H_2 and a MOF should be increased. The MOF should have a binding energy of 15−25 kJ mol^{-1} for satisfactory H_2 storage. One of the approaches to enhance the heat of H_2 adsorption is exchanging the counter-cations included in the anionic framework with metal ions that can interact with H_2 molecules more strongly.

Eddaoudi et al. have synthesized anionic zeolite-like frameworks, $[In_2(HImDC)_4\cdot(HPP^{2+})]_{24}\cdot 36DMF\cdot 192H_2O$ (*rho*-ZMOF, HImDC = 4,5-imidazoledicarboxylic acid, HPP = 1,3,4,6,7,8-hexahydro-2*H*-pyrimido[1,2-a]pyrimidine), $[In(HImDC)_2\cdot(HIM^+)]\cdot 4DMF\cdot CH_3CN\cdot 4H_2O$ (*sod*-ZMOF, HIM = protonated imidazole), and $[In(HImDC)_2\cdot(DMA^+)]_{48}$(DMA-*rho*-ZMOF, DMA = dimethylammonium).[149,292] They exchanged the cations included in the ZIFs, such as HPP^{2+}, HIM^+, and DMA^+, with Na^+, Li^+, and Mg^{2+} by immersion of the ZIFs in the solution of the metal salt and obtained the fully exchanged products at room temperature after 18 h. Contrary to their expectations, however, the H_2 uptake amount and the isosteric heat of H_2 adsorption were not significantly increased compared to those for the MOFs with open metal sites, even though they were higher than those of some neutral MOFs (Table 5). The X-ray structure of Mg-*rho*-ZIF indicated that Mg^{2+} ions were coordinatively saturated with six aqua ligands. The adsorption isotherms for three samples including DMA^+, Li^+, and Mg^{2+} were similar, since the exchanged metal cations retained the aqua ligands even after the activation and direct access of the H_2 molecules to the metal sites was impossible.

Long et al. also reported that Mn^{2+} ions in an anionic framework, $Mn_3[(Mn_4Cl)_3(BTT)_8]_2\cdot 10CH_3OH$, could be exchanged with a variety of metal ions such as Li^+, Cu^+, Fe^{2+},

dx.doi.org/10.1021/cr200274s |*Chem. Rev.* 2012, 112, 782–835

Table 7. Theoretical H_2 Uptake Capacities of MOFs Doped with Li Atoms at 300 K and 10 MPa[296,297] [a]

$Zn_4O(CO)_6$ Cubic lattice	MOF-C6	MOF-C10	MOF-C16	MOF-C22	MOF-C30
ratio C / Li H_2 uptake amount	C_6Li 2.0 wt%	C_5Li 3.3 wt%	$C_{5.3}Li$ 4.2 wt%	$C_{5.5}Li$ 4.6 wt%	C_5/ Li 5.2 wt%
$Zn_4O(CO)_6$ Hexagonal lattice	IRMOF-2-24	IRMOF-2-42	IRMOF-2-60		
ratio C / Li H_2 uptake amount	C_6Li 3.8 wt%	C_6Li 4.0 wt%	C_6Li 5.0 wt%		
$Zn_4O(CO)_6$ Hexagonal lattice	IRMOF-2-54	IRMOF-2-96			
Ratio of C / Li H_2 uptake amount	$C_{5.4}Li$ 5.1 wt%	$C_{5.05}Li$ 5.6 wt%			

[a] In each case the $Zn_4O(CO_2)_6$ connector couples to six aromatic linkers through the O−C−O common to each linker. The MOFs are named according to the number of aromatic carbon atoms. The large green atoms in the linkers represent Li atoms above the linkers while small green Li atoms lie below the linkers. The C_xLi ratio considers only aromatic carbon atoms.

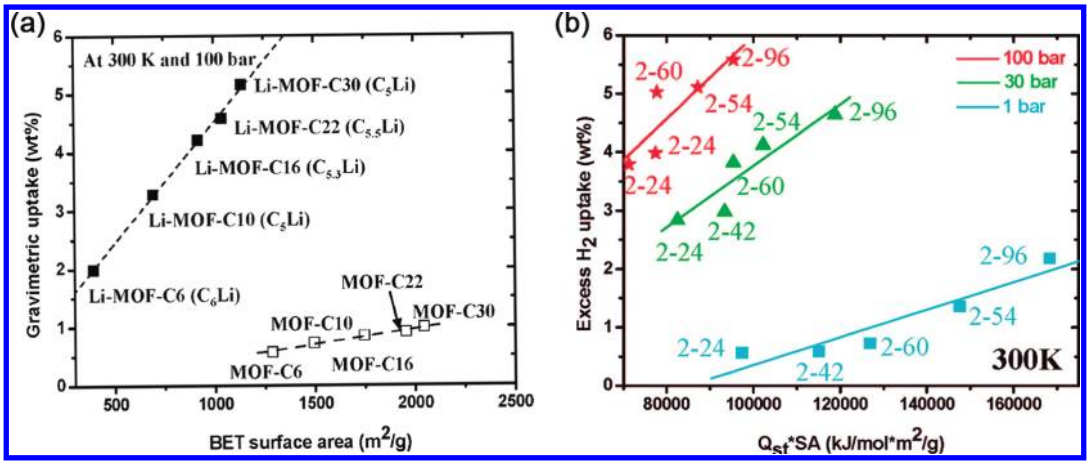

Figure 27. (a) Theoretical gravimetric H_2 uptakes at 300 K and 100 bar plotted against BET surface areas for MOFs and Li-MOFs systems. (b) Relationship between H_2 uptake in IRMOF-Li at 300 K and multiple value of Q_{st} and surface area (SA). This shows that both surface area and the ratio of Li to C are important for high performance. Reproduced with permission from refs 296 and 297. Copyright 2007 and 2008 American Chemical Society.

Co^{2+}, Ni^{2+}, Cu^{2+}, and Zn^{2+}.[112] The H_2 adsorption properties depending on the type and the amount of exchanged metal cations are summarized in Table 6. The total number of extra-framework cations including both charge-balancing and additional adsorbed species are not larger than five, and almost similar for all exchanged materials with Fe^{2+} (4.0), Co^{2+} (4.7), Ni^{2+} (3.0), Cu^{2+} (5.0), Zn^{2+} (5.0), and Li^+ (5.0), respectively (Table 6). The original material showed the isosteric heat of H_2 adsorption of

dx.doi.org/10.1021/cr200274s |Chem. Rev. 2012, 112, 782–835

Table 8. The N_2 and H_2 Gas Adsorption Data for Alkali Metal Ion Doped MOFs, $Zn_2(NDC)_2(diPyNI)$, $Zn_2(NDC)_2(diPyNI)\cdot M$, $Zn_2(NDC)_2(diPyTz)$, and $Zn_2(NDC)_2(diPyTz)\cdot M$[293,294]

	M: diPyNI or diPyTz	BET surface area ($m^2\ g^{-1}$)	DR micropore volume ($cm^3\ g^{-1}$)	H_2/wt% (1 atm, 77 K)	Q_{st} range (kJ mol^{-1})
$Zn_2(NDC)_2(diPyNI)$	0.00	802	0.30	0.93	5.6−3.4 (av. 4.31)
$Zn_2(NDC)_2(diPyNI)\cdot Li$	0.06	676	0.34	1.23	6.3−5.6 (av. 5.96)
$Zn_2(NDC)_2(diPyNI)\cdot Na$	0.10	837	0.33	1.45	5.6−4.5 (av. 4.99)
$Zn_2(NDC)_2(diPyNI)\cdot K$	0.06	988	0.39	1.54	6.0−3.3 (av. 4.51)
$Zn_2(NDC)_2(diPyNI)\cdot K'$	0.26	813	0.32	1.42	5.6−3.7 (av 4.46)
$Zn_2(NDC)_2(diPyNI)\cdot K''$	0.84	382	0.15	0.75	5.1−4.0 (av. 4.45)
$Zn_2(NDC)_2(diPyTz)$	0.00	400	0.16	1.12	8.5−6.5
$Zn_2(NDC)_2(diPyTz)\cdot Li$	0.05	526	0.19	1.46	8.3−6.1
$Zn_2(NDC)_2(diPyTz)\cdot Na$	0.12	558	0.21	1.60	8.7−4.0
$Zn_2(NDC)_2(diPyTz)\cdot K$	0.07	509	0.20	1.51	8.9−4.4
$Zn_2(NDC)_2(diPyTz)\cdot Li^*$,[a]	0.35	163	0.07	0.54	9.0−5.0

[a] * represents different degree of the alkali metal ion doping.

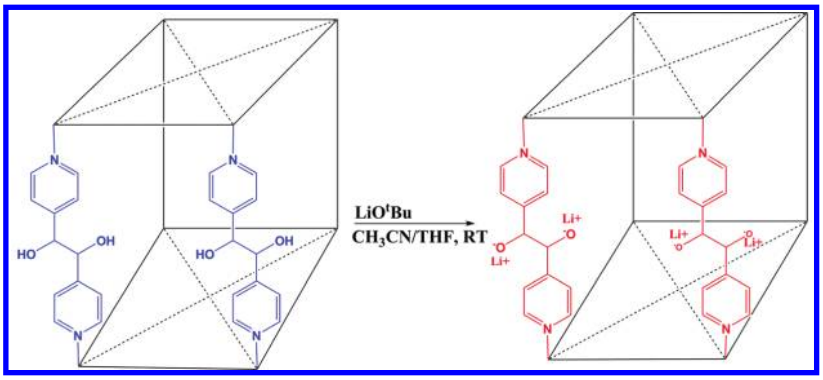

Figure 28. Metal alkoxide formation within a porous framework.[148]

10.1 kJ mol^{-1} and those cation-exchanged materials exhibited a large variation of the H_2 adsorption enthalpy for Li^+ (8.9 kJ mol^{-1}), Cu^+ (9.9 kJ mol^{-1}), Fe^{2+} (10.2 kJ mol^{-1}), Co^{2+} (10.5 kJ mol^{-1}), Ni^{2+} (9.1 kJ mol^{-1}), Cu^{2+} (8.5 kJ mol^{-1}), and Zn^{2+} (9.6 kJ mol^{-1}) respectively.

Champness and Schröder et al. reported an interesting investigation for the kinetics and hysteresis of the H_2 adsorption related with cation exchange.[87] $\{[H_2ppz][In_2(qptc)_2]\cdot 3.5DMF\cdot 5H_2O\}_\infty$ (NOTT-200), which was synthesized from In(III) and a tetracarboxylate ligand (qptc = 1,1′,4′,1″,4″,1‴-quaterphenyl-3,5,3‴,5‴-tetracarboxylate) in the presence of piperazine (ppz), has a doubly interpenetrated anionic structure with three kinds of channels with sizes of 6.6 Å × 4.4 Å (channel A), 4.3 Å × 4.1 Å (channel B), and 4.6 Å × 1.0 Å (channel C). The NH_2^+ group of the H_2ppz^{2+} located in channel B, which forms hydrogen bonds with the oxygen atoms of the ligands, was confirmed by single-crystal X-ray analysis (Figure 25). When the H_2ppz^{2+} cation was substituted with Li^+ by immersion of the MOF in a LiCl solution, $\{Li_{1.5}[H_3O]_{0.5}[In_2(L)_2]\cdot 11H_2O\}_\infty$ (NOTT-201) resulted. The structure of NOTT-201 showed an open channel B that must be blocked by the NH_2^+ group in NOTT-200. NOTT-200 showed big hysteretic N_2 and H_2 adsorption isotherms due to the kinetic trapping of H_2 and H_2ppz^{2+} blocking the channel B. However, NOTT-201 showed not only the typical Type-1 isotherms with no hysteresis but also enhanced H_2 adsorption capacity from 0.96 wt % to 1.02 wt % at 78 K and 1 bar as well as increased H_2 adsorption enthalpy from 9.0 kJ mol^{-1} to 10.1 kJ mol^{-1} (Figure 26). The result suggests that the postsynthetic cation exchange with a reasonable selection of cation size would increase the heat of H_2 adsorption as well as modulate the hysteretic adsorption behavior in an anionic framework.

Hupp et al. reported a MOF doped with 5 mol % Li^+ cations, which was obtained by the reaction of a doubly interpenetrated $[Zn_2(NDC)_2(diPyNI)]$ containing redox active ligand *N*,*N*′-di-(4-pyridyl)-1,4,5,8-naphthalenetetracarboxydiimide (diPyNI) with the suspension of Li in DMF. The Li^+-doped material showed the H_2 uptake of 1.63 wt % at 77 K and 1 atm, which is considerably higher than 0.93 wt % in the original material.[151] The heat of H_2 adsorption was also increased from 5.5 kJ mol^{-1} to 6.1 kJ mol^{-1} by the Li^+ ion doping. This rather small increase in the H_2 adsorption enthalpy is attributed to solvent molecules coordinated at the impregnated Li^+ ion, which cannot be completely removed by the activation. According to the authors' later report, more than one DMF molecules remained per Li^+ ion even after the activation by heating at 110 °C under vacuum for 24 h.[293,294] Therefore, the effect of the Li^+ was structural instead of electronic.

The reports demonstrating the enhancement of H_2 uptake by the impregnation of the metal ion in MOFs are very rare, but the examples described above suggest that other materials can be modified by a similar manner to enhance the hydrogen affinity. However, the effect of the impregnated metal ions would be rather minor because the degree of metal ion impregnation may be not so high and the doped metal ions would be usually coordinated with solvent molecules, which cannot be easily removed by the activation.

To exploit the system having enhanced heat of H_2 adsorption, theoretical studies were performed on metal-doped MOFs and

dx.doi.org/10.1021/cr200274s |*Chem. Rev.* 2012, 112, 782–835

the results suggested significantly increased hydrogen sorption capacities.[295−303] For example, Goddard et al. reported that Li-doped MOFs can significantly improve H_2 uptake capacities at ambient conditions.[296,297] They examined the effect of metal doping in MOFs that have cubic and hexagonal lattices constructed from $[Zn_4O]$ SBUs with carboxylate links. In order to predict the structure and H_2 uptake behavior, quantum mechanics (QM) calculation and GCMC simulations have been used, respectively. The results suggest that Li atoms prefer to bind at the centers of the hexagonal aromatic rings, but Li atoms at the adjacent aromatic rings should locate on the opposite sides (Table 7). Furthermore, the doped Li atoms increase the amount of hydrogen storage in the MOFs. The simulated results for MOF-C6 and IRMOF-2-24 were compared with the experimental results of MOF-5[60] and MOF-177,[62] respectively. Further extension of the organic linker via increasing number of phenyl ring afforded more positive values by offering increased attractive sites for Li. According to these results, IRMOF-2-96 which has the biggest ligand showed a H_2 storage capacity of 6.5 wt % at 243 K and 100 bar. The ligands employed in the theoretical study and the predicted H_2 uptake amounts at ambient temperature and high pressure are summarized in Table 7 and Figure 27. Despite the interesting theoretical results, however, synthetic chemists would doubt whether those ligands could be really synthesized. In addition, a full charge was used on the Li in the calculations, but it may be overestimated even if we consider that some of the charge on Li should be used to interact with the framework.

Hupp et al. also reported a metal doping effect on the H_2 sorption properties of MOFs.[148,293,294] They reduced the organic linker of doubly interpenetrated $Zn_2(NDC)_2(diPyNI)$ and triply interpenetrated $Zn_2(NDC)_2(diPyTz)$ (diPyTz = 3,6-di(4-pyridyl)-1,2,4,5-tetrazine) with an alkali metal (Na, Li, and K) naphthalenides. The ligands in the frameworks were partially reduced (6−84%) and the alkali metal ions were concomitantly introduced to the MOFs as counter-cations.[293,294] All alkali metal doped MOFs exhibited enhanced N_2 and H_2 sorption properties. As summarized in Table 8, the alkali metal cation doping together with framework reduction significantly enhanced the H_2 uptake but modestly increased the binding energy of H_2 with the MOFs. This must be attributed to the solvent DMF molecules still bound to the doped metal ions (DMF/M^+ ratio = 0.28−1.8), as evidenced by ^1H NMR spectra. At 77 K and 1 atm, the reversible H_2 uptake increased with dopant cation size: 0.93 wt % for the pristine $Zn_2(NDC)_2(diPyNI)$, 1.23 wt % for $Zn_2(NDC)_2(diPyNI)\cdot Li$, 1.45 wt % for $Zn_2(NDC)_2(diPyTz)\cdot Na$, and 1.54 wt % for $Zn_2(NDC)_2(diPyNI)\cdot K$. It was noted that the improved N_2 and H_2 uptakes were not attributed to the direct access of the gas molecules to the doped metal cations, but due to the cation-induced displacement of the catenated structures. The order of average Q_{st} values for $Zn_2(NDC)_2(diPyNI)\cdot M$ is $Li^+ > Na^+ > K^+$, which corresponds to the ratio of cation charge to radius. This must be related with the strength of the interaction between the alkali cations and quadrupole moment of H_2. However, a triply interpenetrated framework, $Zn_2(NDC)_2(diPyTz)$, represented the different Q_{st} order ($K^+ > Na^+ > Li^+$). Although those results represent enhanced hydrogen uptakes at 77 K and 1 atm by doped metal cations, they did not show a direct relationship between hydrogen sorption capacities and heat of H_2 adsorption. This indicated that the catenated structures might interfere with the direct interaction between an alkali metal cation and H_2 gas.

As an alternative approach for alkali metal doping, Hupp and Hartman et al. independently performed postsynthetic modifications

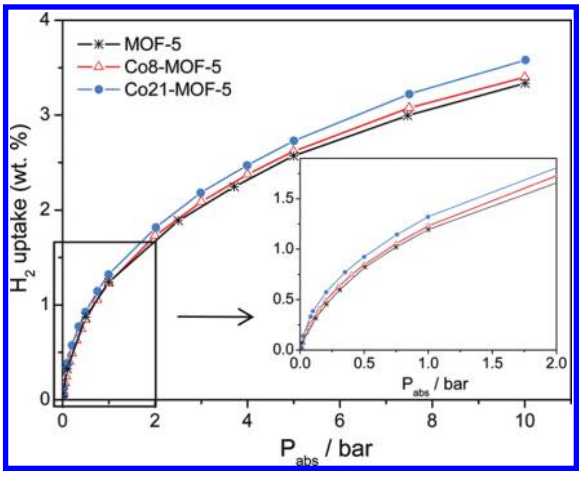

Figure 29. Hydrogen adsorption isotherms for Co8-MOF-5, Co21-MOF-5, and MOF-5 at 77 K. Reproduced with permission from ref 306. Copyright 2010 American Chemical Society.

of pendant-alcohol groups of the MOFs.[148,304] Hupp et al. exchanged the hydroxyl protons of the diol groups of the organic linker in the Zn(II) MOF (DO-MOF) with Li^+ and Mg^{2+} ions by using lithium and magnesium alkoxides (Figure 28).[148] They achieved this modification by exchanging (via soaking) the initially present guest solvent molecules (DMF) with more volatile THF and then stirring the MOF in an excess of $Li^+[O(CH_3)_3^-]$ in CH_3CN/THF. The extent of lithium loading was controlled by adjusting the stirring rate and time. When the Li^+/Zn^{2+} ratio was about 0.20, the BET surface area and the pore volume slightly increased, and the H_2 uptake also increased (1.32 wt % at 1 atm) with the increased isosteric heat of H_2 adsorption (6.3−6.6 kJ mol^{-1}) compared to the H_2 uptake capacity (1.23 wt % at 77 K and 1 atm) and the isosteric heat of H_2 adsorption (6.3−4.7 kJ mol^{-1}) of the original DO-MOF. It is not common that isosteric heat increases as the H_2 loading increases. However, as the Li^+/Zn^{2+} ratio became 2.62, the isosteric heat of H_2 adsorption as well as the surface area and pore volume diminished. Similar results were observed for the Mg^{2+} exchanged samples. When the Mg^{2+}/Zn^{2+} ratio was 0.86, the surface area and pore volume increased and the isosteric heat reached 6.2−6.9 kJ mol^{-1}, but the H_2 uptake capacity slightly decreased. When the Mg^{2+}/Zn^{2+} ratio increased to 2.02, the heat of H_2 adsorption slightly increased to 7.3−5.0 kJ mol^{-1}, although the H_2 uptake capacity decreased. At low to intermediate levels of metal ion substitution, the activated metals appear to be naked, apart from alkoxide anchoring, providing unusual Q_{st} behavior and modest enhancement of H_2 sorption.

Hartmann et al. also exchanged the protons of hydroxyl pendants in [Al(OH)(BDC-OH)], MIL-53(Al) with lithium by using lithium diisopropylamide (LDA).[304] By chemical analysis, it was found that 15% of the acidic framework protons were exchanged with lithium. The apparent Langmuir (BET) surface area of Li-MIL-53(Al) was 1450 $m^2\ g^{-1}$ (1384 $m^2\ g^{-1}$), which is 180 $m^2\ g^{-1}$ smaller than that of the original MOF. The H_2 uptake capacities at 77 K and 1 bar were 0.5 wt % and 1.7 wt % for nondoped MIL-53(Al)-OH and Li-doped Li-MIL-53(Al), respectively. The enhancement of the H_2 storage in Li-MIL-53(Al) was not only due to the lithium doping but also due to the temperature-induced structural transformation. The isosteric heat of H_2 adsorption clearly demonstrated the impact of Li^+ doping on hydrogen sorption. Compared with the undoped compound which has an adsorption enthalpy of 5.8−4.4 kJ mol^{-1},

dx.doi.org/10.1021/cr200274s |Chem. Rev. 2012, 112, 782–835

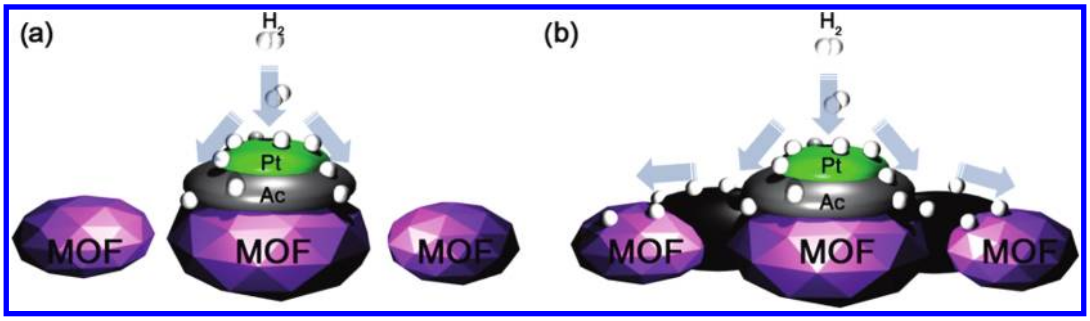

Figure 30. (a) Primary spillover of atomic hydrogen from Pt metal to the activated carbon support and secondary spillover to the MOF receptor that has limited contacts with the support. (b) Facilitated primary and secondary spillover by using carbon bridges (dark black zone).[308]

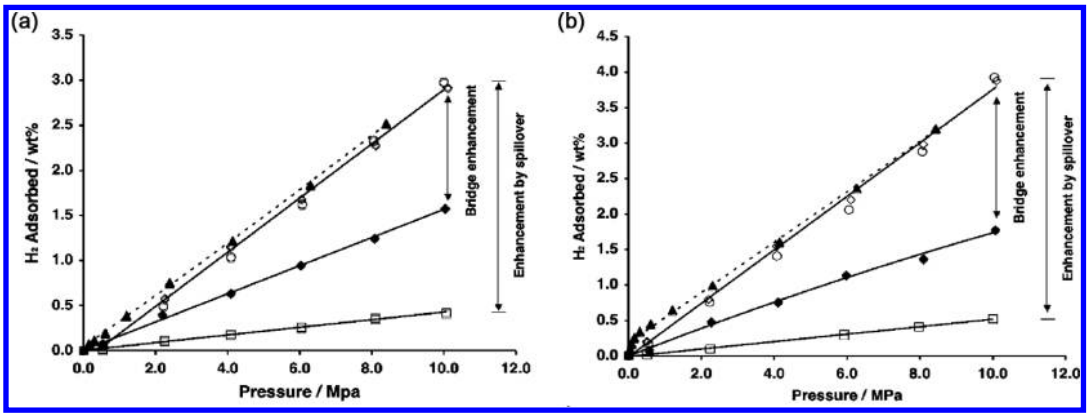

Figure 31. (a) High-pressure hydrogen isotherms at 298 K for pure IRMOF-1 (□), and physical mixture of Pt/AC and IRMOF-1 (1:9 weight ratio; ♦) and for a carbon-bridged sample of Pt/AC-bridges-IRMOF-1: first adsorption (○), desorption (▲), and second adsorption (◊). (b) High-pressure hydrogen isotherms at 298 K for pure IRMOF-8 (□), physical mixture (1:9 weight ratio) of Pt/AC and IRMOF-8 (♦) and for a sample of Pt/AC-bridges-IRMOF-8: first adsorption (○), desorption (▲), and second adsorption (◊). Reproduced with permission from ref 308. Copyright 2006 American Chemical Society.

Table 9. Hydrogen Uptake Capacities of MOFs Embedded with Pt Nanoparticles[310]

sample	Pt CVD condition	Pt content (wt%)	average Pt size (nm)	BET surface area ($m^2\ g^{-1}$)	pore volume ($cm^3\ g^{-1}$)	H_2 uptake at 298 K, 10 MPa (wt %)
IRMOF				1430	0.69	0.44
Pt/IRMOF-8-1	303 K, 6 h	4.8	2.2 ± 1.0	1175	0.59	0.85
Pt/IRMOF-8-2	308 K, 8 h	6.2	3.9 ± 1.9	1071	0.53	0.67
Pt/IRMOF-8-3	318 K, 11 h	7.7	9.1 ± 4.3	1014	0.55	0.49

Li-MIL-53(Al) has a heat of H_2 adsorption of 11.6−6.4 kJ mol^{-1}, which approaches the theoretical maximum value of ca. 13 kJ mol^{-1}.[305]

There has also been a report about the transition metal ion doping in a MOF. Botas et al. partially doped MOF-5 with Co^{2+} ions during the crystallization step of the solvothermal synthesis.[306] On the basis of the ICP analysis, the materials were characterized as $Zn_{3.68}Co_{0.32}O(BDC)_3(DEF)_{0.75}$ (Co8-MOF-5) containing 8% Co and 92% Zn and $Zn_{3.16}Co_{0.84}O(BDC)_3$-$(DEF)_{0.47}$ (Co21-MOF-5) having 21% Co and 79% Zn. The chemical compositions of Co-MOF-5 materials suggest that the substitution of more than one Co^{2+} ion in a given Zn_4O cluster is difficult. The PXRD data indicated that both undoped and Co-doped MOF-5 had an identical crystal phase. The pink color of the as-synthesized crystal changed to blue upon evacuation due to the removal of the guest solvent, indicating that the coordination geometry around Co^{2+} changed from octahedral to tetrahedral by the loss of two diethylformamide (DEF). The hydrogen uptake capacities at 77 K and 10 bar were in the order of Co21-MOF-5 > Co8-MOF-5 > MOF-5. Furthermore, the heat of adsorption in Co21-MOF-5 was ~7 kJ mol^{-1}, which is higher than that (5.5 kJ mol^{-1}) of MOF-5. Even though the increase in the absolute H_2 uptake was not so large, the H_2 uptake increased proportionally with the increased amount of Co^{2+}. This result suggests that Co^{2+} must be a good doping agent for enhancing the hydrogen storage capacity (Figure 29).

As discussed above, MOFs can be doped with alkali, alkaline earth, or transition metal ions at the ligand parts or at the metal centers. Although the metal doped MOFs showed enhanced H_2 uptakes, the enhancement was in general not so great. Because of the lack of H_2 storage data at ambient temperature, it is difficult to predict the impact of the metal doping on the H_2 storage at

dx.doi.org/10.1021/cr200274s |Chem. Rev. 2012, 112, 782–835

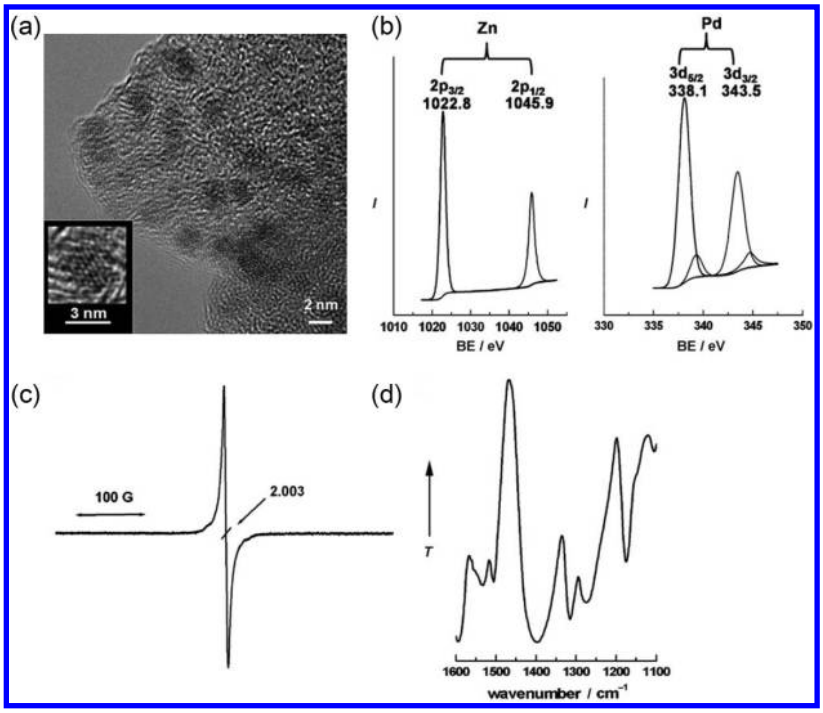

Figure 32. SNU-3 with embedded Pd nanoparticles. (a) FE-TEM image, (b) X-ray photoelectron spectrum, (c) EPR spectrum (powder, measured at 173 K), and (d) IR spectrum, for 3 wt % PdNPs@$[SNU\text{-}3]^{0.54+}(NO^{3-})_{0.54}$. Reproduced with permission from ref 134. Copyright 2009 WILEY-VCH Verlag GmbH & Co. KGaA, Weinheim.

room temperature, but based on the rather small values of the H_2 adsorption enthalpy, we may assume that it would be minor.

4.2.1.3. Spillover Effect of Palladium and Platinum. A hydrogen spillover effect has been known for a long time in the hydrogenation catalysts. It is defined as the dissociative chemisorption of hydrogen on the metal and the subsequent migration of atomic hydrogen onto the surface of the support such as alumina, carbon, etc.[307] The support can be considered as the primary receptor for atomic hydrogen. Spillover on a secondary material is referred to as secondary spillover.

Yang et al. reported significantly enhanced room temperature hydrogen storage in some MOFs, which was achieved simply by mixing Pt/AC (AC = active carbon) catalysts with IRMOF-1 or IRMOF-8.[69] For a spillover experiment, they utilized active carbon containing 5 wt % Pt that was ground with the secondary receptor (IRMOF-1 or IRMOF-8) in a weight ratio of 1:9. For this physical mixture, the active carbon and MOF were considered as the primary and secondary receptor, respectively. The high pressure gas sorption data at 298 K and 10 MPa indicated that the hydrogen adsorption capacity of Pt/AC was 1.0 wt % and those of unmodified IRMOF-1 and IRMOF-8 were ~0.4 wt % and ~0.5 wt %, respectively. The physical mixture of the Pt/AC catalyst and the MOF substantially increased the hydrogen uptake capacities by ca. three times that of the pure MOF, resulting in 1.56 wt % for modified the IRMOF-1 and 1.8 wt % for the modified IRMOF-8. Furthermore, these modified MOFs not only adsorbed 70% of the total H_2 uptake amount within 1 h, but also released over 60% of the adsorbed hydrogen in 10 min. Yang et al. also reported that a carbon bridge introduced in the mixture further increased H_2 uptake.[308] They used sucrose to build a carbon bridge to increase the contacts between the catalyst and the MOF. The three-component mixture of sucrose consisting of Pt/AC (5 wt % of Pt) and IRMOF-1 or IRMOF-8 (1:9 weight ratio of catalyst/MOF) was heated up to 473 K under helium for 3 h. This step allows sucrose to diffuse to the space between the particles of catalyst and MOF by melting, and enhances the secondary spillover (Figure 30). During the construction of the sucrose bridge, the MOFs did not decompose as confirmed by PXRD and the N_2 adsorption data. With a carbon bridge, the hydrogen uptake capacities of the modified IRMOF-1 and IRMOF-8 reached to ca. 3 wt % and 4 wt % (Figure 31), respectively, at ambient temperature and 10 MPa, which are 6−8 times higher than that of the original MOFs. The H_2 uptake amount of 4 wt % for IRMOF-8 is equivalent to ca. 34 hydrogen atoms per formula unit $[Zn_4O(NDC)_3]$. The isosteric heat of the H_2 adsorption estimated from the data at 298 and 323 K by using Clausius−Clapeyron equation was 20−23 kJ mol^{-1}, which was the highest value reported so far for the MOFs.

Table 10. The H_2 Adsorption Capacities of MOFs Embedded with Palladium Nanoparticles[134,152]

sample	amount of Pd NPs, wt %	condition	H_2 uptake amount, wt %
PdNPs@SNU-3	0	77 K, 1 bar 298 K, 95 bar	1.03 0.13
	1.70/5 min[a]	77 K, 1 bar	0.35
	2.60/10 min[a]	77 K, 1 bar	0.20
	2.94/30 min[a]	77 K, 1 bar	1.48
		298 K, 95 bar	0.3
	3.20/60 min[a]	77 K, 1 bar	1.10
MIL-100(Al)	0	77 K, 4 MPa	3.1
		298 K, 4 MPa	0.19
MIL-100(Al)/Pd	9.7	77 K, 4 MPa	1.3
		298 K, 4 MPa	0.35

[a] In the MeCN solution of 1.0×10^{-3} M $Pd(NO_3)_2 \cdot 2H_2O$ with a 1:1 mol ratio of Pd^{II}/MOF.

dx.doi.org/10.1021/cr200274s |*Chem. Rev.* 2012, 112, 782–835

The report that physical mixing of Pt metal to the activated carbon support with MOF increased the H_2 storage has been reproduced by Liu et al.[309] According to this report, MIL-101 and MIL-53 were mixed with Pt/AC catalysts and carbon bridge. The H_2 storage capacities of the carbon bridge modified MIL-101 and MIL-53 became 1.14 wt % and 0.63 wt % at 293 K and 5.0 MPa, respectively, which were significantly higher than that of the pristine-MOFs.

Increased hydrogen storage by direct embedding of metal nanoparticles also has been reported for Pt-doped IRMOF-8,[310] Pt-doped MOF-177,[311] Ni-doped MIL-101,[312] Pd-doped redox-active MOF,[134] and Pd-doped MIL-100.[152] Recently, Yang et al. prepared Pt-doped IRMOF-8 by the chemical vapor deposition (CVD) of volatile platinum precursor, (trimethyl)methylcyclopentadienyl platinum(IV), and reported that the different Pt nanoparticle sizes in Pt-doped IRMOF-8 yielded different spillover effects on the hydrogen storage.[310] As shown in Table 9, the hydrogen storage capacities are in the order of Pt/IRMOF-8-1 > Pt/IRMOF-8-2 > Pt/IRMOF-8-3, which contain Pt nanoparticles of sizes, 2.2, 3.9, and 9.1 nm, respectively. The results indicate that smaller size nanoparticles afford better spillover effect.

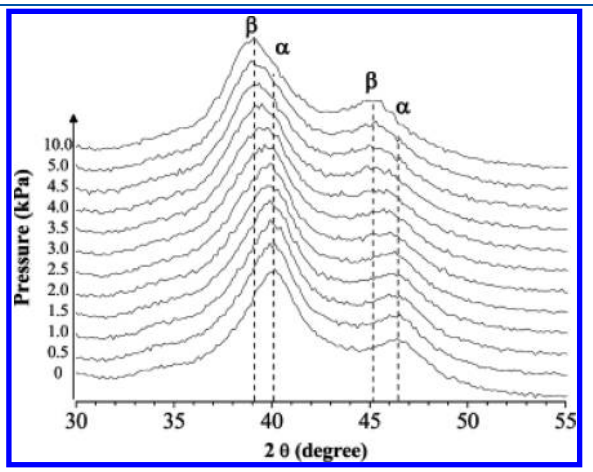

Figure 33. In situ PXRD for MIL-100(Al)/Pd (0.35 wt %) measured during the hydrogen absorption at room temperature and 10 kPa. The peak positions for the α- and β-phase of Pd NPs are shown by the straight lines in order to follow the phase transition during hydrogen adsorption. Reproduced with permission from ref 152. Copyright 2010 American Chemical Society.

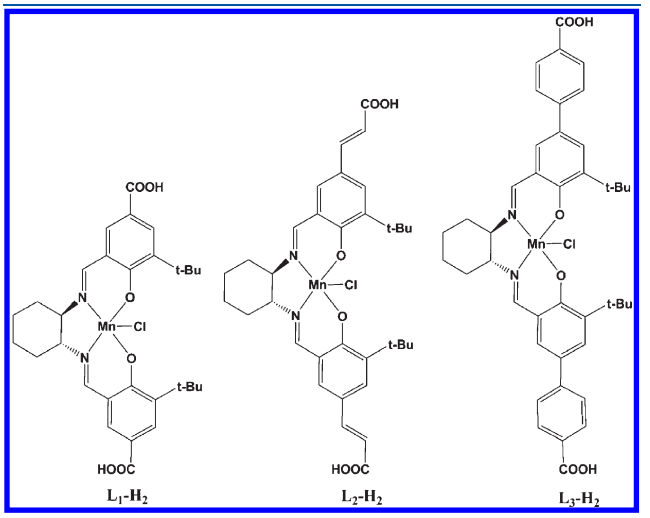

Figure 35. Schiff base complexes with dicarboxylic acid groups used in the synthesis of CMOFs.[321]

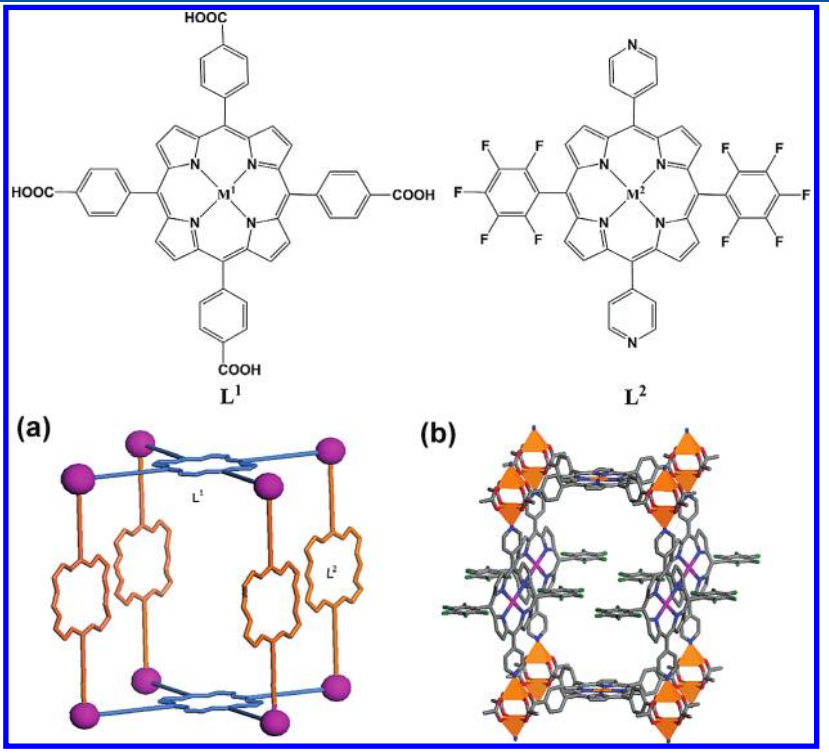

Figure 34. Structure of porphyrins and porphyrinic framework materials.[320] Porphyrinic tetraacid ligand (L^1) and pillaring dipyridylporphyrin strut (L^2). (a) Schematic diagram of porphyrinic framework. (b) Unit cell view of a porphyrinic framework.

dx.doi.org/10.1021/cr200274s |*Chem. Rev.* 2012, 112, 782–835

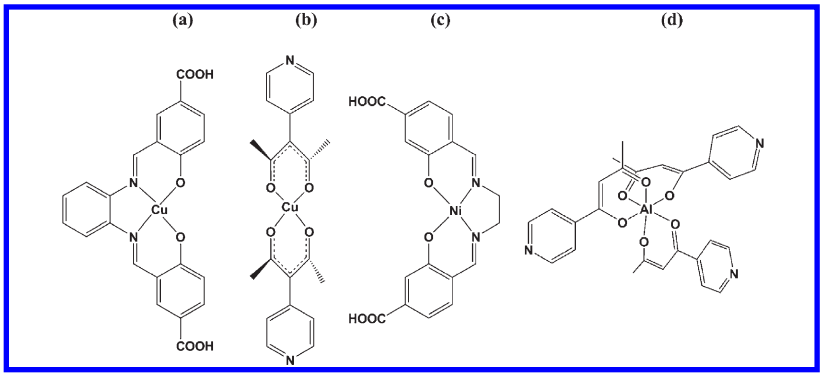

Figure 36. Schiff base complexes used in the synthesis of (a) $[Zn_3(OH)_2(L^{Cu})_2]\cdot 2DMF$,[322] (b) $[Cu_2(pzdc)_2L(H_2O)]\cdot 4H_2O$,[324] (c) $[Ln_2(L^{Ni})_3(DMF)(H_2O)_3]\cdot 4DMF\cdot 10H_2O$ (Ln = Er, Lu),[325] and (d) $[(ZnBr_2)_3(AlL_3)_2]$, $[Pd_6(AlL_3)_8](NO_3)_{12}$.[323]

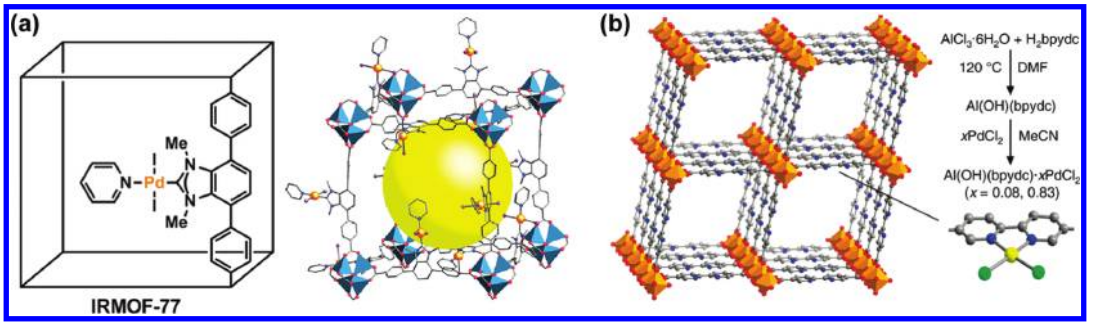

Figure 37. (a) Structure of IRMOF-77. Atom colors: blue tetrahedron, Zn; purple, I; orange, Pd; red, O; blue sphere, N. (b) Synthesis and representative structure of MOF-253. Post synthetic insertion of $PdCl_2$ into free bpy ligand sites. Atom colors: orange, yellow, green, red, blue, and gray spheres represent octahedral Al, Pd, Cl, O, N, and C atoms, respectively. Reproduced with permission from ref 329 and 330. Copyright 2010 American Chemical Society.

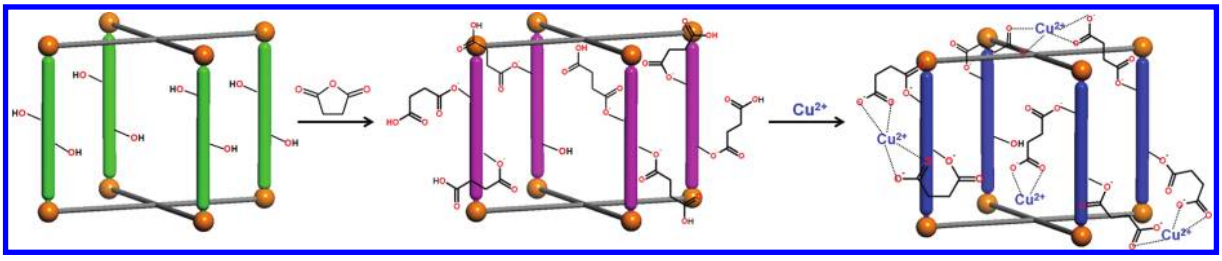

Figure 38. Schematic representation of generating open metal sites in the ligand part: postsynthetic reaction of $[Zn_2(TCPB)(DPG)]$ with succinic anhydride followed by the Cu^{2+} chelation.[331]

It should be noted here that nanoparticles embedded in MOFs were not so stable for many cycles of H_2 adsorption and desorption. It was reported that Pt@MOF-177 adsorbed 2.5 wt % of H_2 at room temperature and 144 bar in the first adsorption cycle.[311] However, in the second cycle, the storage capacity considerably decreased to 0.5 wt %, which was close to the value of pure MOF-177. This was due to the formation of Pt hydrides, from which hydrogen could not be desorbed at room-temperature.

Suh and co-workers have developed novel methods for producing metal nanoparticles in MOFs by using redox reactions between the redox-active MOFs and metal ions such as Ag(I), Au(III), and Pd(II).[95,130−134] They demonstrated that Pd nanoparticles (3.0 ± 0.4 nm, 3 wt % Pd) could be embedded in a redox-active MOF, $[Zn_3(NTB)_2]_n$ (SNU-3) simply by immersing the MOF in a MeCN solution of $Pd(NO_3)_2\cdot 2H_2O$ at room temperature without any extra reducing or capping agent.[134] The redox reaction between the redox-active organic building block (NTB^{3-}) in the MOF and the Pd(II) ions produced the positively charged framework that incorporated palladium nanoparticles (Pd NPs) and NO_3^- anions in the channels. The particle size was independent of immersion time and the concentration of the Pd(II) solution. The PXRD pattern indicated that the framework structure was maintained even after the formation of the Pd NPs. The amount of Pd NPs embedded in the MOF could be controlled by the immersion time of the MOF in the palladium(II) solution. The coexistence of Pd^0 nanoparticles and Zn^{II} in the MOF was supported by X-ray photoelectron spectroscopy (Figure 32). The H_2 adsorption capacity depended on the amount of Pd NPs loaded in the MOF. In particular, the MOF loaded with 3 wt % Pd NPs showed significantly increased H_2 sorption capacities (1.48 wt % at 77 K and 1 atm and 0.30 wt % at 298 K and 100 bar) compared to the respective 1.03 wt %

dx.doi.org/10.1021/cr200274s |Chem. Rev. 2012, 112, 782–835

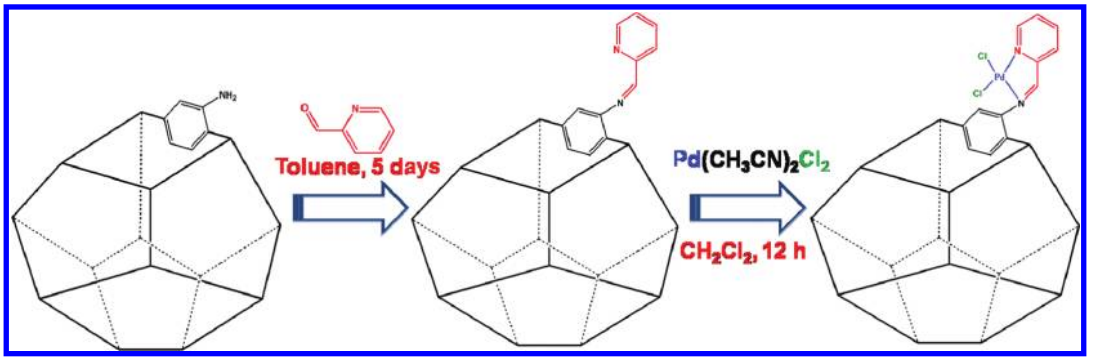

Figure 39. Covalent modification of UMCM-1-NH_2 for generating open metal sites on the struts of the MOFs.[332]

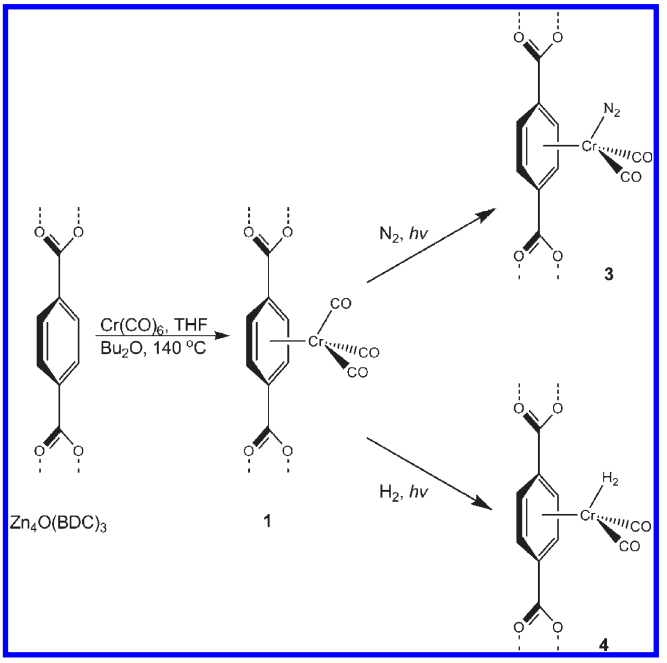

Figure 40. Reaction of $Zn_4O(BDC)_3$ with $Cr(CO)_6$ to generate $Zn_4O[(BDC)Cr(CO)_3]_3$, followed by photolysis under N_2 or H_2 to afford $Zn_4O[(BDC)Cr(CO)_2(N_2)]_3$ and $Zn_4O[(BDC)Cr(CO)_2(H_2)]_3$.[272]

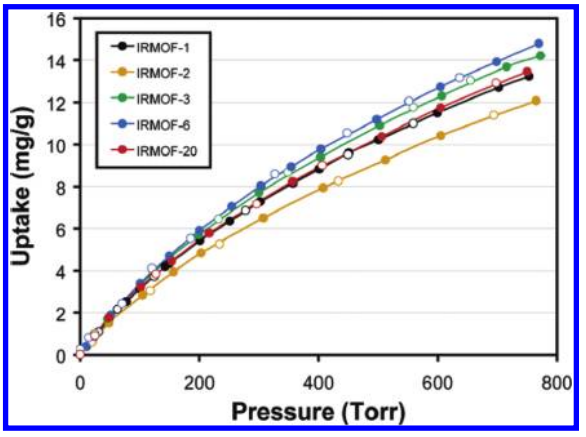

Figure 41. The H_2 adsorption isotherms at 77 K for noncatenated IRMOFs having various functional groups at the organic linker. Reproduced with permission from ref 61. Copyright 2006 American Chemical Society.

and 0.13 wt % for $[Zn_3(NTB)_2]$ without Pd NPs, even though the surface area significantly decreased from 559 $m^2 g^{-1}$ to 242 $m^2 g^{-1}$ due to the Pd NPs and NO_3^- counter-anions occupying the pores. Interestingly, the zero coverage isosteric heat of 3 wt % Pd NPs loaded sample was 6.62 kJ mol^{-1}, which was significantly lower than that (8.11 kJ mol^{-1}) of $[Zn_3(NTB)_2]$.

Férey et al. also fabricated Pd NPs (size 2.5 ± 0.2 nm) into MIL-100(Al).[152] After embedding Pd NPs, the composite MIL-100(Al)/Pd (0.35 wt %) adsorbed 1.3 wt % H_2 at 77 K and 40 bar, which was lower than 1.8 wt % H_2 of MIL-100(Al) under the same condition due to the decrease in the specific surface area and pore volume. However, at room temperature and 4 MPa, it showed an H_2 uptake capacity (0.35 wt %) that was almost twice as high as that (0.19 wt %) of the pristine MIL-100(Al) (Table 10). The adsorption isotherm of MIL-100(Al)/Pd at ambient temperature and low pressure (below 0.1 MPa) displayed a steep increase, which was ascribed to the transformation of Pd to Pd hydride. Under a H_2 pressure of 4.5 kPa, PXRD peaks for Pd were shifted to the low angle region, suggesting the lattice expansion of Pd by the formation of Pd β-hydride (Figure 33). It was difficult to identify the pressure value where the phase transition of Pd hydride started to form Pd β-hydride because very broad PXRD peaks resulted from a convolution of the α- and β-phase of Pd hydride.

4.2.1.4. Other Possibilities: Open Metal Sites at Organic Linker Parts. Porous MOFs constructed of various types of porphyrin complexes have been known for many years.[313−316] Even though there has been no H_2 adsorption data reported for the porphyrin based MOFs, they have been suggested as possible H_2 storage materials since they contain open metal sites with respect to the square-planar coordination plane.[55,317−320] From multiple porphyrin ligands and various metal ions, porous robust porphyrinic materials (RPMs) (Figure 34) have been synthesized.[320]

Similarly, MOFs constructed from Schiff Base complexes also possess open metal sites. Lin and co-workers synthesized a series of isoreticular chiral metal−organic frameworks (CMOFs) from the chiral Mn-Salen-derived dicarboxylate ligands and $[Zn_4O]$ SBUs, which contained Mn(III) open metal sites (Figure 35).[321] The N_2 adsorption isotherm showed a negligible surface area due to the collapse of the framework on activation. There have been many reports for such networks, in which Schiff base complexes were used as the building blocks (Figure 36), although the H_2 gas sorption data were missing.[322−327]

The other approach for creating the open metal sites in the MOF is the synthesis of an organometallic MOF where the metal fragments are attached to the organic linker parts. This approach

dx.doi.org/10.1021/cr200274s |*Chem. Rev.* 2012, 112, 782–835

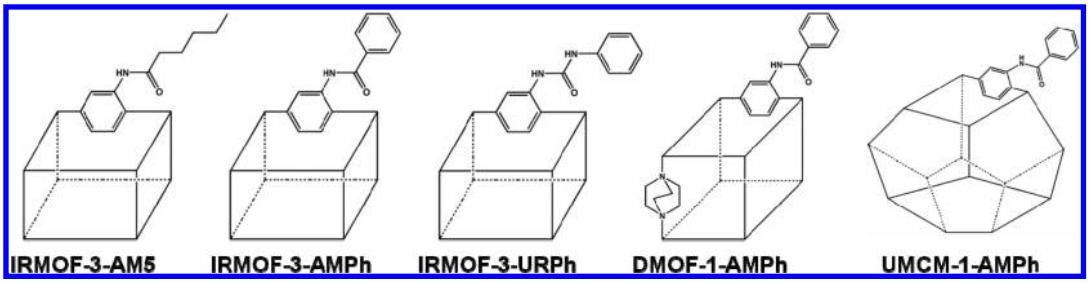

Figure 42. Schematic representation of the five postsynthetically modified MOFs. IRMOF-3, DMOF-1, UMCM-1 contain $-NH_2$ functional groups.[150]

involves covalent functionalization followed by metalation and photochemical attachment of organometallic complexes to the aromatic components of the struts. Although the H_2 uptake data in the materials have not been reported, their open metal sites might lead to enhanced isosteric heat of H_2 adsorption.

Lin and co-workers used (*R*)-6,6′-dichloro-2,2′-dihydroxy-1,1′-binaphthyl-4,4′-bipyridine (L) as a chiral bridging ligand containing orthogonal functional groups to make a MOF, $[Cd_3Cl_6L_3]\cdot 4DMF\cdot 6MeOH\cdot 3H_2O$,[328] The two pyridyl functional groups were linked with metal ions to form extended networks, whereas the orthogonal chiral 2,2′-dihydroxy secondary functional groups remained free and they were available for introduction of additional metal ions by postsynthetic modification using $Ti(O^iPr)_4$.

Yaghi and co-workers prepared a metalated ligand [4,7-bis(4-carboxylphenyl)-1,3-dimethylbenzimidazol-2-ylidene](pyridyl)-palladium(II) iodide and then assembled it into an IRMOF, which was denoted as IRMOF-77, $[Zn_4O(C_{28}H_{21}I_2N_3O_4Pd)_3]$ (Figure 37a).[329] They also reported a MOF with open 2,2′-bpy coordination sites, [Al(OH)(bpydc)] (MOF-253), synthesized from 2,2′-bipyridine-5,5′-dicarboxylic acid (H_2bpydc; Figure 37b).[330] Because of the accessibility of the chelating bpy units in MOF-253, they could insert $PdCl_2$ and $Cu(BF_4)_2$ in the MOF by soaking the MOF solid in acetonitrile solutions of $PdCl_2$ and $Cu(BF_4)_2$ respectively, which afforded MOF-253·*x*$PdCl_2$ (*x* = 0.08, 0.83) and MOF-253·0.97$Cu(BF_4)_2$.

In combining covalent and coordinate covalent postsynthetic modification, the MOF is covalently bound to a chelating group, and then metalated. Hupp, Nguyen, and co-workers synthesized the Zn-pillared paddle-wheel MOF, Zn_2(TCPB)(DPG) (TCPB = 1,2,4,5-tetrakis(4-carboxyphenyl)-benzene, and DPG = *meso*-1,2-bis(4-pyridyl)-1,2-ethanediol) and then reacted it with succinic anhydride (Figure 38).[331] The diols in the MOF readily reacted with succinic anhydride, resulting in a ring opened product having free carboxylic acid groups. The free carboxylic groups could be further modified by immersion in aqueous solution of $CuCl_2$.

Yaghi and co-workers reacted the amine-functionalized framework $[(Zn_4O)_3(BDC\text{-}NH_2)_3(BTB)_4]$, UMCM-1-$NH_2$ with 2-pyridinecarboxaldehyde to obtain the covalently bound iminopyridine chelate derivative $(Zn_4O)_3(BDC\text{-}C_6H_5N_2)_3(BTB)_4$, which was reacted with $PdCl_2(CH_3CN)_2$ to result the metal-complexed MOF $(Zn_4O)_3(BDC\text{-}C_6H_5N_2PdCl_2)_3(BTB)_4$ (Figure 39).[332]

Kaye and Long revealed that the benzene rings in $[Zn_4O(BDC)_3]$ (IRMOF-1) can be fully loaded with $Cr(CO)_3$ groups to afford $Zn_4O[(bdc)Cr(CO)_3]_3$.[70] The decarbonylated framework with three open coordination sites per metal was prepared by heating at 200 °C under a flow of nitrogen for 5 h, and low-pressure N_2 and H_2 adsorption measurements were performed at 298 K. It adsorbed fewer than 0.2 molecules of H_2 per formula unit of MOF at 298 K due to the aggregation of Cr atoms. Gentle photolysis conditions enabled substitution of a single CO ligand per metal by N_2 and H_2 to give $Zn_4O[(bdc)Cr(CO)_2(N_2)]_3$ and $Zn_4O[(bdc)Cr(CO)_2(H_2)]_3$ (Figure 40), respectively, which was characterized by infrared spectroscopy. Considering the H_2 binding energy for $[(C_6H_6)Cr(CO)_2(H_2)]$ and $[(C_6H_5Me)Cr(CO)_2(H_2)]$, the H_2 binding energy for $Zn_4O[(bdc)Cr(CO)_2(H_2)]_3$ was expected to be 60−70 kJ mol^{-1}.[272]

Table 11. Hydrogen Uptake Properties of a Series of MOFs (IRMOF-3, UMCM-1-NH_2, and DMOF-1-NH_2) upon Postsynthetic Modification[150]

compound	conversion	H_2 uptake, wt%[a]	Q_{st}[b] kJ mol^{-1}
IRMOF-3	N/A	1.52 ± 0.02	5.3 ± 0.3
IRMOF-3-AMP-a	32%	1.73	5.3
IRMOF-3-AMP-b	44%	1.73	5.7
IRMOF-3-AMP-c	70%	1.68	6.0
IRMOF-3-URPh	41 ± 5%	1.54 ± 0.06	5.7 ± 0.3
IRMOF-3-AM-5	86 ± 5%	1.21 ± 0.02	5.7 ± 0.3
UMCM-1-NH_2	N/A	1.35 ± 0.05	4.6 ± 0.4
UMCM-1-AMPh	76 ± 1%	1.54 ± 0.04	5.2 ± 0.2
DMOF-1-NH_2	N/A	2.08 ± 0.01	5.6
DMOF-1-AMPh	63 ± 1%	1.69 ± 0.05	7.0 ± 0.1

[a] Gravimetric uptake at 77 K and 1 atm. [b] Heat of H_2 adsorption at zero coverage was calculated by using a virial equation.

4.2.2. Control of Pore Size and Functionalization of MOFs. As seen in Figure 19, some MOFs have high room temperature H_2 storage capacities even though they have relatively small surface areas and do not contain open metal sites (see the region marked by the yellow circle in Figure 19). This indicates that increasing the surface area and creating open metal sites cannot guarantee a high H_2 storage capacity at room temperature. Small pore size is also necessary to achieve high room temperature H_2 uptake, since the small pore enables the overlap of energy potentials between the opposing walls, leading to higher interaction energy with the H_2 molecules.[333,334] Two MOFs of M(HBTC)(4,4′-bpy) (M = Ni and Co) showed high H_2 storage capacities at 298 K and 70 bar, 1.20 wt % (Ni) and 0.96 wt % (Co), even though their BET surface areas were relatively low, 1590 $m^2\ g^{-1}$ (Ni) and 887 $m^2\ g^{-1}$ (Co).[89] The room temperature H_2 storage capacity of Ni(HBTC)(4,4′-bpy) is the highest among the MOFs reported so far. The frameworks have small pores: nonlinear honeycomb channels with only 5 Å at the narrowest and 8 Å at the widest spacing, and rectangular channels of size 7 Å × 6 Å.

The primitive cubic MOF, $[Co_3(NDC)_3(dabco)]$, based on trinuclear pinwheel motifs is another example having high H_2

dx.doi.org/10.1021/cr200274s |*Chem. Rev.* 2012, 112, 782–835

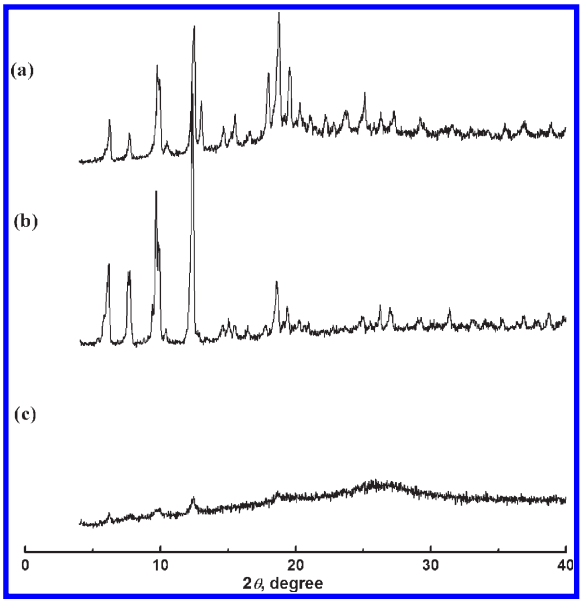

Figure 43. The PXRD patterns of SNU-5 having open metal sites.[76] (a) As-synthesized, (b) SNU-5 prepared by drying at 170 °C under a vacuum for 24 h, and (c) SNU-5 after exposure to air for 24 h.

sorption (0.89 wt % at 298 K and 17.2 bar). The high H_2 uptake is attributed to the combination of relatively high surface area (BET, 1502 $m^2 g^{-1}$) and narrow channels (4.5 Å).[187]

Control of interpenetration (or catenation) is one of the effective ways to adjust pore size. The 3D interpenetrating framework [Cu(hfipbb)(H_2hfipbb)$_{0.5}$] (H_2hfipbb = 4,4′-(hexafluoroisopropylidene)bis(benzoic acid)) contains two types of pores, small pores of ca. 3.5 Å × 3.5 Å size and large pores of 5.1 Å × 5.1 Å size.[197] At room temperature and 48 atm, it can adsorb about 1 wt % of H_2.

Lin and co-workers reported that 4-fold interpenetrating networks based Zn_4O clusters generated 3D channels of less than 5 Å. These materials showed BET surface areas of only 396 $m^2 g^{-1}$ and 502 $m^2 g^{-1}$, but they adsorbed 1.12 wt % and 0.98 wt % of H_2 at room temperature and 48 bar.[216]

As introduced in section 3.5, the chemical environment of the pore surface as well as the pore size can be tuned by functionalization of MOFs, which can enhance the hydrogen adsorption. Yaghi and co-workers prepared isoreticular structures from modified BDC with different functional groups. These structures include IRMOF-1, IRMOF-2 with -Br, IRMOF-3 with -NH_2, IRMOF-6 with C_2H_4, and IRMOF-20 with thieno[3,2-*b*]thiophene. They expected that the electronic character of the organic linkers might affect the amount of hydrogen uptake in the IRMOF.[61] Contrary to expectations, IRMOFs having different functional groups showed quite similar H_2 adsorption capacities (12−15 mg g^{-1}) at 77 K and 1 bar (Figure 41). Although the functionalized IRMOFs (IRMOF-3 and -6) have slightly enhanced H_2 uptake capacities up to 25% that of the unfunctionalized IRMOF-1, they are not attributed to the electronic effect of the functional groups. It is rather due to the reduction of pore size by the pendant groups: 9.6−9.8 Å for IRMOF-2, -3, and -6, compared to 12.1 Å of IRMOF-1. The observations were corroborated with some computational studies. According to second-order Møller−Plesset (MP2) calculations,[335] the H_2 molecule should be located above the center of the functionalized aromatic ring for optimal interaction geometry. The interaction energy could be enhanced by 15% by electron-donating groups such as amino and methyl group. The −Br substituent is a weak electron-withdrawing group and decreases the interaction energy between H_2 and the phenyl ring because of the stronger direct interaction between H_2 and Br since Br has greater polarizability than the phenyl ring.

Cohen et al. have tuned the H_2 adsorption properties of MOFs by postsynthetic modification.[150] They reacted NH_2-MOFs such as IRMOF-3, DMOF-1-NH_2, and UMCM-1-NH_2 with anhydrides or isocyanates to obtain amide groups (Figure 42). This type of postsynthetic modification could change the pore properties of the MOFs and alter not only the hydrogen uptake capacities but also the heats of the H_2 adsorption. The degree of conversion of the functional group (ranging from 32% to 76%) was controlled by reaction time. The resulting IRMOF-3-AMPh, IRMOF-3-URPh, and UMCM-1-AMPh exhibited enhanced H_2 storage capacities up to 1.73 wt %, 1.54 wt %, and 1.54 wt %, respectively, compared to those of IRMOF-3 (1.51 wt %) and UMCM-1-NH_2 (1.35 wt %). In addition, it was observed that the H_2 adsorption capacity and the heat of H_2 adsorption are higher for MOFs having aromatic ring substituents than those with alkyl chain substituents. The results support the hypothesis that the optimal interaction geometry between H_2 and the MOF is with the H_2 molecule located at the center of the phenyl ring. The hydrogen uptake capacities and the isosteric heats of the functionalized MOFs are summarized in Table 11.

5. TECHNIQUES AND METHODS FOR HYDROGEN SORPTION EXPERIMENTS

5.1. Preparation and Handling

It has been reported that the gas sorption properties of MOFs are significantly affected by the preparation and handling methods of as-synthesized samples, such as reaction temperature and reaction time during solvothermal synthesis. For example, it was reported that N_2 and H_2 uptake capacities of MOF-5, which was desolvated by guest-exchange with methylene chloride followed by evacuation at room temperature, depend on the reaction temperature, reaction time, and the type of solvent used in the solvothermal synthesis.[31]

The structural stability of MOFs against water vapor adsorption is an important issue for potential applications of MOFs in the gas storage because complete removal of H_2O from industrial gas resources is quite difficult. Unfortunately, the structure of some MOFs such as MOF-5,[31] MOF-177,[336] and SNU-5[76] were partially dissociated upon exposure to air as evidenced by the PXRD patterns (Figure 43), resulting in a significant decrease in the gas sorption capacities.

Li and Yang measured H_2O vapor adsorption isotherm at 298 K for MOF-177 to test the stability of MOF-177 upon H_2O adsorption. MOF-177 adsorbed up to ∼10 wt % H_2O, and ∼65% of the adsorbed H_2O could not be desorbed readily at room temperature. Therefore, trace amount of H_2O present in the hydrogen sources should be removed, and the MOFs should be handled with great care not to be exposed to air in order to achieve maximum H_2 storage capacities.

5.2. Activation Methods

In general, as-synthesized MOFs include the solvent molecules, from which the MOFs are synthesized, in the pores and channels. For applications of MOFs as porous materials, it is necessary to remove guest solvent molecules from the pores of the MOF without the loss of porosity, a process termed "activation".

dx.doi.org/10.1021/cr200274s |*Chem. Rev.* 2012, 112, 782–835

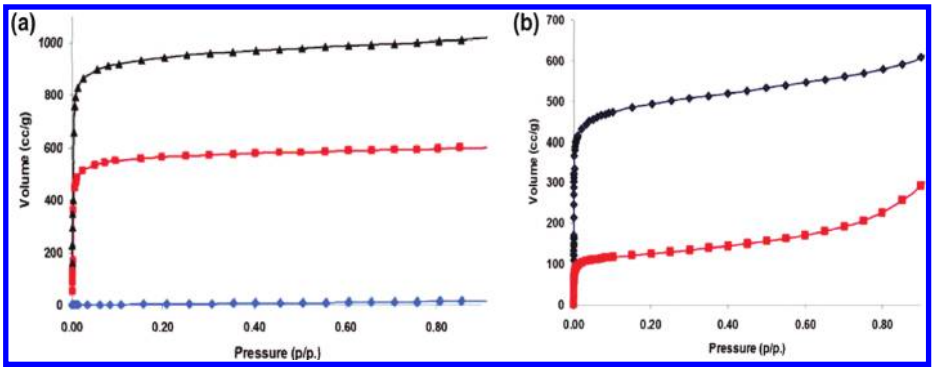

Figure 44. (a) The N_2 isotherms of IRMOF-3 at 77 K, after SCD activation (top), after the exchange with $CHCl_3$ followed by evacuation at 25 °C (middle), and conventional activation at 100 °C (bottom). (b) The N_2 isotherms of IRMOF-16 at 77 K, after SCD activation (top) and after exchange with $CHCl_3$ followed by activation at 25 °C (bottom). Reproduced with permission from ref 339. Copyright 2009 American Chemical Society.

In general, MOFs are activated by (1) heat-evacuation method based on the thermogravimetry data or (2) exchange of guest molecules with lower boiling point solvent followed by room temperature evacuation or heat-evacuation. When activating a MOF by guest exchange followed by evacuation, one must keep in mind that guest exchange often transforms the structure of the MOF, which depends on the type of solvent. In particular, the solvent molecules that form hydrogen bonds with MOF frameworks change the structure significantly,[337,338] and the desolvated structures are still affected by the guest-exchanged structures. Therefore, the choice of solvent to exchange with the guest solvent molecules of the as-synthesized sample is important and the potential structural changes caused by the guest exchange should be examined by powder X-ray diffraction data. Once the guest solvent molecules in the MOFs are exchanged with a low-boiling solvent, the MOF can be activated by room temperature evacuation, heat evacuation, or treatment with supercritical CO_2.

Unfortunately, the heat-evacuation method sometimes results in collapsed framework structures. In particular, MOFs with large pores (mesopores) are susceptible to incomplete activation, which leads to partial or even complete loss of porosity. Yaghi and co-workers reported that MOFs maintained their porosity in the absence of guests when they were activated by exchanging the guest solvent molecules with a lower boiling point solvent followed by evacuation under relatively mild conditions.[59]

Supercritical processing has been employed in aerogel fabrication to prevent collapse of the pores resulting from the elimination of surface tension upon removal of the solvent.[339] In supercritical CO_2 activation, the sample is treated through many cycles of the introduction of supercritical CO_2, commonly at 40 °C and 200 atm, followed by venting at 1 atm. Hupp and co-workers demonstrated that MOFs activated by the supercritical CO_2 drying (SCD) method adsorbed significantly greater amounts of gases than those activated by evacuation methods; thus SCD could be utilized as a potential activation method.[339] They reported the results on four MOFs that were comprised of dicarboxylate organic ligands and Zn_4O clusters as nodes. The MOFs exhibited instability under most activation conditions. As shown in Figure 44, the SCD method increases the internal surface areas of the MOFs compared with the other methods such as (a) thermal evacuation of the solvent used in the synthesis (DMF or DEF), a "conventional activation" method, and (b) guest exchange with liquid solvents with lower boiling points (e.g., DMF ↔ $CHCl_3$; DEF ↔ THF) followed by evacuation at moderate temperatures. For example, when IRMOF-3 was activated by the conventional heat-evacuation method and by the room-temperature evacuation method after the guest solvent was exchanged with $CHCl_3$, the surface areas obtained were 10 $m^2\ g^{-1}$ and 1800 $m^2\ g^{-1}$, respectively. However, when it was activated by supercritical CO_2, the N_2 accessible surface area became 2850 $m^2\ g^{-1}$. IRMOF-16 showed no porosity when it was activated through conventional methods, but the surface area became 470 $m^2\ g^{-1}$ when it was evacuated at room temperature after the solvent exchange. When IRMOF-16 was activated by SCD, it showed the surface area of 1910 $m^2\ g^{-1}$ (Figure 44b). The significant increase of the surface area through the supercritical CO_2 activation was explained by the inhibition of collapse of interparticle mesopores during the SCD activation.

Lin et al. reported that MOFs that had breathing properties adsorbed much higher amounts of gases when they were activated by a freeze-drying method compared to those activated by room temperature- or heat-evacuation methods.[340] They applied the freeze-drying method to activate MOFs that were constructed from tetracarboxylic acid and Cu_2 paddle-wheel units. The MOFs had breathing properties as evidenced by PXRD patterns. In the freeze-drying experiment, the guest solvent molecules with high boiling point were exchanged with benzene, which was subsequently removed by sublimation under a vacuum at temperatures below its freezing point. Higher internal surface areas and H_2 uptake capacities were obtained for the freeze-dried samples compared to those activated by the conventional activation method, since bypass of the liquid phase eliminated the detrimental effect where surface tension induces the mesopore collapse.

However, the compounds utilized by Hupp and Lin contained coordinated solvent molecules at the metal centers, and it was not fully characterized whether the coordinated solvent molecules were removed or not during the activation, something which must affect the gas sorption properties. In addition, there was no clear experimental evidence showing how the framework structure changed depending on the activation methods.

Recently, Suh and co-workers revealed by complete single-crystal X-ray analyses that the *guest-free* structures of a MOF are determined not only by the activation methods but also by temperature.[173] They synthesized a doubly interpenetrated Zn_4O-type MOF having PdF_2-net structure, SNU-77, from the solvothermal reaction of an extended carboxylic acid H_3TCBPA and $Zn(NO_3)_2 \cdot 6H_2O$ in DMA. Desolvated samples of SNU-77 exhibit high surface area (BET, 3670 $m^2\ g^{-1}$), high pore volume (1.52 $cm^3\ g^{-1}$), and exceptionally high uptake

dx.doi.org/10.1021/cr200274s |*Chem. Rev.* 2012, 112, 782–835

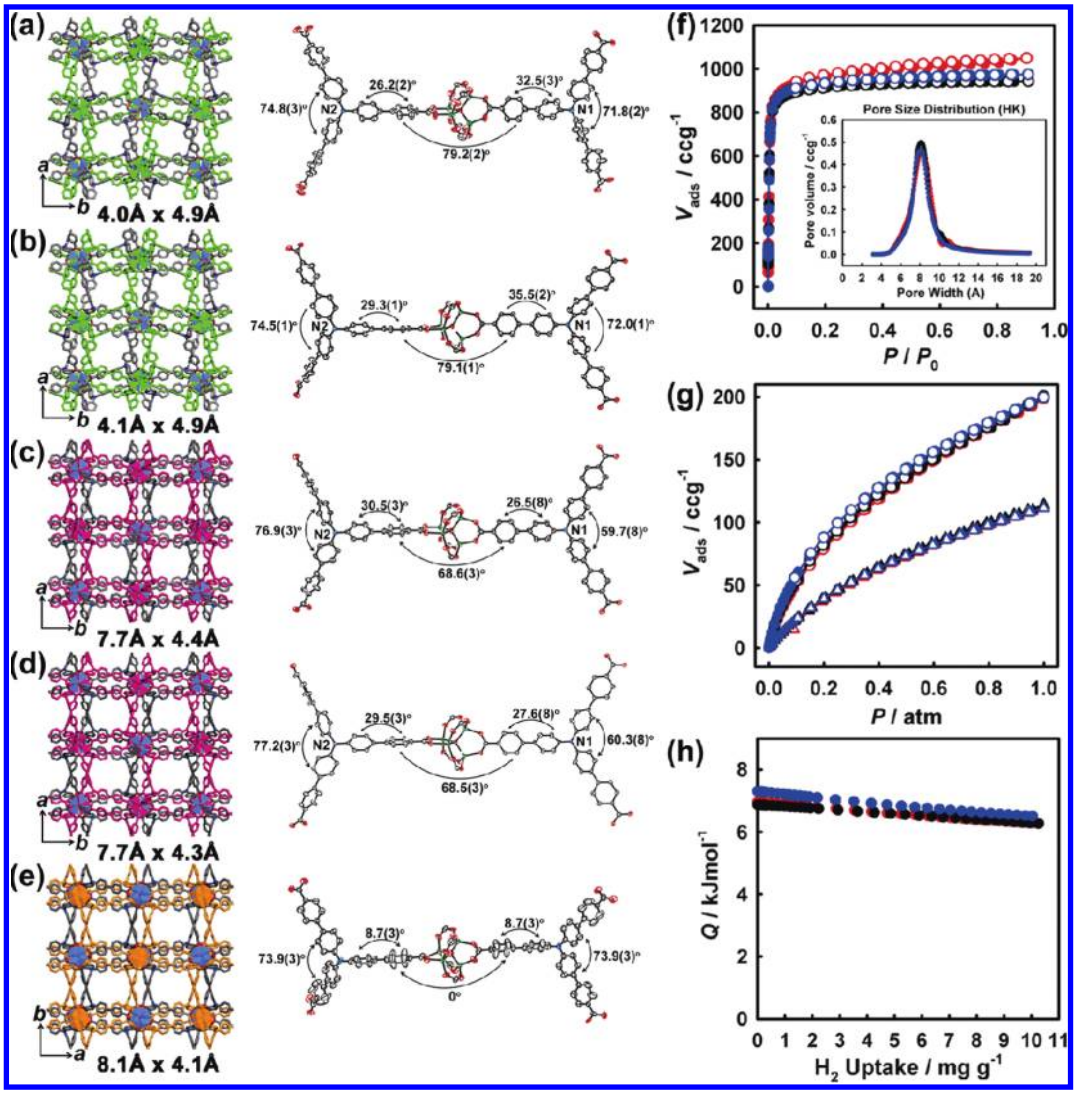

Figure 45. X-ray crystal structures of (a) SNU-77, (b) SNU-77′, (c) SNU-77R, (d) SNU-77S, and (e) SNU-77H. Doubly interpenetrated networks are represented in two different colors. The numbers below each structure represent the effective aperture size. (f) N_2 gas sorption isotherms at 77 K (Inset: pore-size distributions estimated by the Horvath−Kawazoe method), (g) H_2 gas sorption isotherms at 77 K (circles) and 87 K (triangles), and (h) isosteric heats of H_2 adsorption, for SNU-77R (black), SNU-77S (blue), and SNU-77H (red). Filled shapes: adsorption; open shapes: desorption. Reproduced with permission from ref 173. Copyright 2011 WILEY-VCH Verlag GmbH & Co. KGaA, Weinheim.

capacities for N_2, H_2, O_2, CO_2, and CH_4 gases. They activated the MOF by various activation methods such as room temperature evacuation, supercritical CO_2 drying, and high temperature evacuation. During these activation processes, SNU-77 underwent single-crystal to single-crystal transformations to afford single crystals of SNU-77R, SNU-77S, and SNU-77H, respectively (Figure 45). These *guest-free* MOFs exhibited different fine structures at room temperature, with different pore shapes and pore window sizes differing by several angstroms (Å's). Although their cell dimensions changed only slightly and Zn_4O units were located at similar positions, the organic ligands underwent rotational motion and changed the dihedral angles between the phenyl rings of the ligand. The variable-temperature synchrotron X-ray single-crystal analyses reveal that the guest-free structure is affected also by the temperature change. Interestingly, despite the different fine structures, SNU-77R, SNU-77S, and SNU-77H show similar gas sorption properties. The authors explained this phenomenon by the nonbreathing nature of the MOF as well as by the additional temperature-induced structural transformation that provided similar fine structures at the cryogenic gas sorption temperature. The results together with the reports by Hupp and Lin suggest that MOFs which collapse upon thermal evacuation or highly flexible MOFs, which exhibit a breathing effect will show increased gas sorption capacities when activated by supercritical CO_2 or by freeze-drying method compared to the thermal evacuation methods.

Suh's group proved this by preparation of a highly flexible MOF, which showed significantly increased surface area and gas sorption capacities on supercritical CO_2 treatment rather than evacuation methods.[259] They prepared a flexible non-interpenetrated MOF constructed from Cu(II) paddle-wheel units and tetrakis[4-(carboxyphenyl)oxamethyl]methane acid (H_4TCM). They activated the MOF by supercritical CO_2, which afforded [Cu_2(TCM)] (SNU-21S), and by the heat-evacuation method, which provided [Cu_2(TCM)] (SNU-21H). Both activation methods removed the coordinated solvent molecules from

dx.doi.org/10.1021/cr200274s |*Chem. Rev.* 2012, 112, 782–835

the metal centers as well as the guest solvent molecules included in the pores. SNU-21S showed greater gas sorption capacities than SNU-21H. The Langmuir surface area and pore volume of SNU-21S were 905 $m^2 g^{-1}$ and 0.31 $cm^3 g^{-1}$, respectively, while those of SNU-21H were 695 $m^2 g^{-1}$ and 0.25 $cm^3 g^{-1}$. In addition, the H_2 uptake capacity and isosteric heat of the H_2 adsorption were higher in SNU-21S than in SNU-21H.

It must be quite difficult to prove whether the supercritical CO_2 treatment of MOFs would remove even the coordinated solvent molecules or not. In general, the MOFs with open metal sites pick up water molecules from the air as soon as they are exposed to air, and thus even if the method generates open metal sites, the handling of the sample, such as taking the sample out of the drying apparatus and transferring it to a gas sorption apparatus might involve exposure to air to result in the MOFs without open metal sites. Despite these difficulties, it has been reported that the coordinated solvent molecules were removed from SNU-21S[259] and NU-100[28] by the supercritical CO_2 drying method. In any case, the supercritical drying method is definitely milder than the heat-evacuation method. However, we cannot say clearly whether supercritical CO_2 treatment can always remove the coordinated solvent molecules or not until more data are accumulated to confirm this.

5.3. Gravimetric versus Volumetric Measurements

To characterize MOFs as H_2 storage materials, the H_2 uptake isotherms should be measured accurately during H_2 adsorption and desorption. There are two different methods for this measurement: gravimetric and volumetric. In the gravimetric method, the increased mass of the adsorbed H_2 in a MOF is directly estimated by using a highly sensitive microbalance.[334] The mass of the adsorbed H_2 decreases when high pressure is applied to the system, due to its buoyancy, and this weight loss is calculated using the skeletal volume of the MOF's framework and the density of H_2.[45] In the volumetric method, however, the pressure change of H_2 by the adsorption (or desorption) is measured in a closed chamber having a constant volume.[334] The volume of the adsorbed H_2 in the MOF is then calculated by subtracting the volume of H_2 in the free space from the total volume of dosed H_2.

The major disadvantage of the gravimetric method is that any H_2O impurity can lead to a significant error because the weight of a H_2O molecule is equal to the weight of nine H_2 molecules.[341] Even though the concentration of the H_2O impurity in H_2 is as low as several ppm, the sample is usually kept in a H_2 flow for a certain period of time to determine the weight change. As a result, the sample can adsorb a significant amount of H_2O, particularly when a small amount of sample is used during prolonged measurements.

On the contrary, the volumetric method determines the pressure change of H_2 during the adsorption (or desorption) in a closed chamber. As a result, the adsorption of H_2O can lead to a much lower error in the H_2 uptake capacity. The significant disadvantage of the volumetric method is the inherent errors caused by the indirect determination of the adsorbed quantities. The main sources of errors of this technique are the error in the determination of the pressure cell and adsorption cell volumes, the error in the pressure and temperature measurements, the error from the leakage of gas at high pressure, the error in the sample mass, and the error from the equation of state.[342] For ease of operation and availability of instrumentation, however, the volumetric method is more favorable in most cases discussed above.[34]

Yaghi and co-workers compared the H_2 sorption isotherms of MOF-177 measured by both volumetric and gravimetric methods at 77 K to establish the importance of calibrating gas adsorption instrumentation prior to evaluating the H_2 storage capacities.[45] The isotherms obtained by the volumetric method saturated at close to 60 bar with maximum excess amounts of 75 mg g^{-1} at 77 K. Gravimetric measurement provided a similar profile to the volumetric isotherm with an excess uptake capacity of 73 mg g^{-1} at a saturation pressure of 50 bar. They explained that the small difference between volumetric and gravimetric uptake is attributed to the difference in the apparent surface area of MOF-177 samples. The lower saturation pressure in the gravimetric measurements compared to that determined by volumetric measurements may be attributed to differences in the buoyancy correction made by He gas. Buoyancy correction cannot be made for the volume of adsorbed H_2 in the gravimetric measurement, which leads to an underestimation of H_2 uptake in the high pressure region.

5.4. Physical Methods for Characterization of Hydrogen-MOF Interaction

It is important to analyze carefully how the H_2 molecules interact with a framework so that one can modify the weakly interacting part of the framework with the strongly interacting functional groups. To find interaction sites of the MOF that are active toward H_2 molecules and to understand the mechanism of the interaction, neutron diffraction, inelastic neutron scattering, and infrared spectroscopy have been used.

5.4.1. Neutron Powder Diffraction. Neutron diffraction has been employed to find the exact position of light H_2 or D_2 molecules in a framework, since neutrons strongly scatter the nuclei of ^1H and ^2H, while X-ray is insensitive to such nuclei. To study the H_2 adsorption in a MOF, the neutron diffraction pattern of the guest-free framework as well as those patterns at various D_2-loading are obtained. The structure is then refined by using Fourier difference maps to locate the exact positions of D_2.

Yildirim and Hartman used neutron diffraction to find the adsorption sites in MOF-5.[343] The fully deuterated samples of MOF-5 were prepared and samples were finely ground in order to eliminate the effects of preferred orientation, and then adsorption experiments were conducted at 3.5 K. The first adsorption sites were near the center of the three ZnO_3 triangular faces, of which there are four such sites for each tetrahedral Zn_4O cluster. The second adsorption sites are at the top of the ZnO_3 triangles. The next two sites are occupied nearly equally as H_2 loading increases. The sites are just above the two oxygens and the top of the hexagonal linkers. The structural refinement indicates that these four adsorption sites are almost completely occupied to yield a 6.8 wt % H_2 uptake. This demonstrates that the metal-oxide cluster units are the main adsorption sites for H_2 at low temperature and high pressure. The adsorbed H_2 molecules form nanoclusters with intermolecular distances of 3.0 Å and the potential H_2 uptake is as high as 11 wt %.

Neutron powder diffraction studies were conducted by Long et al. on Mn-BTT at 3.5 K.[48] The strongest adsorption site at low loading was 2.27 Å from the Mn^{2+} ions, and the second binding site was a sodalite-like cage created by the chloride ion and the tetrazolate rings. The second sites adsorbed up to 48 H_2 molecules per formula unit, and they were fully occupied as the H_2 loading increases. The next strongest adsorption site was

dx.doi.org/10.1021/cr200274s |Chem. Rev. 2012, 112, 782–835

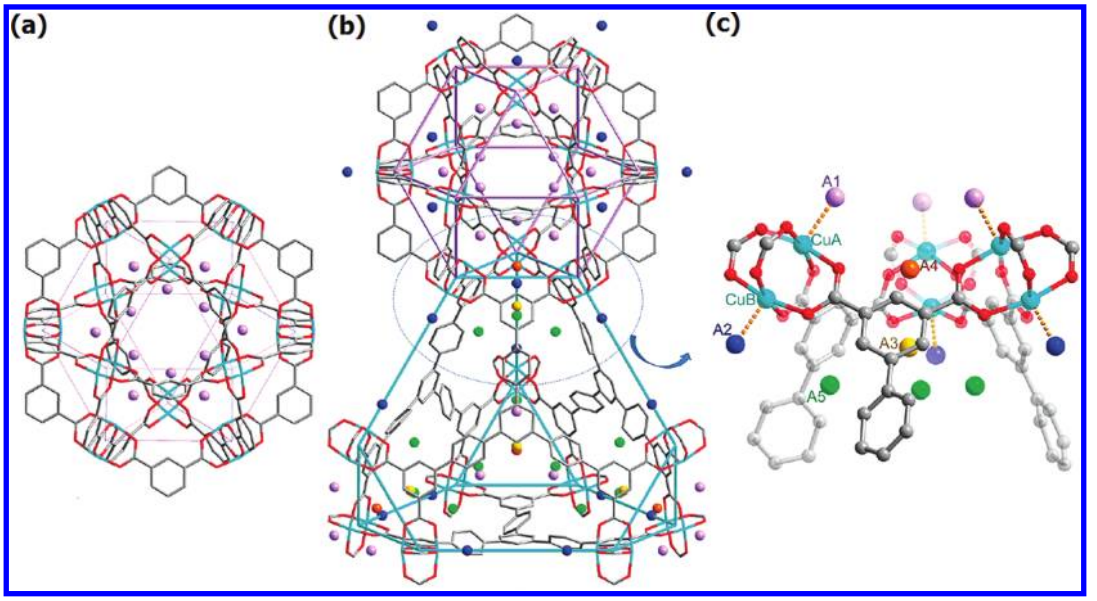

Figure 46. Views for the adsorbed D_2 positions in the desolvated sample of NOTT-112: (a) D_2 positions in the cuboctahedral cage at D_2 loading of $0.5D_2$/Cu; (b) D_2 positions in the cage A and cage B at D_2 loading of 2.0 D_2/Cu; (c) view of five D_2 positions (A1, A2, A3, A4, and A5) at 2.0 D_2/Cu; gray, carbon; red, oxygen; turquoise, copper. The D_2 positions are represented by colored spheres: A1, lavender; A2, blue; A3, yellow; A4, orange; A5, green. Reproduced with permission from ref 275. Copyright 2010 American Chemical Society.

situated inside the large framework cavity. The fourth site was located inside the smaller cavities and near carbon atoms of the tetrazolate ring. This work also confirmed that the open metal sites were one of the important factors for the creation of MOF for H_2 storage.

Kepert et al. reported the D_2 adsorption sites in HKUST-1 that has accessible Cu(II) sites.[288] The Rietveld analyses for the D_2 loaded sample showed six D_2 adsorption sites. The first adsorption site was at the open Cu(II) site of the paddle-wheel unit. The site was located 2.39 Å from the Cu atom, indicating a strong interaction between the H_2 molecule and the Cu(II). The distance is greater than that of σ-bonded η^2-dihydrogen complexes of group 6 metal ions. The next binding site was 3.29 Å from the benzene ring of BTC, and the third binding site was located 3.88 Å from the six BTC oxygen atoms and 3.90 Å from the three BTC carbon atoms. The remaining adsorption sites were located near the benzene carbon atoms and the carboxylate carbon atoms as well as the oxygen atoms. This also confirms that the open metal sites in the MOFs are important for H_2 storage.

Zhou et al. have also performed neutron diffraction studies to find the H_2 adsorption site in the rare earth MOF, Y(BTC)-$(H_2O)\cdot 4.3H_2O$.[245] The desolvated sample showed H_2 uptake capacities of 1.57 wt % at 77 K and 1 atm, and 2.1 wt % at 77 K and 10 bar. Powder neutron diffraction data upon dosing D_2 gas were measured at 4 K. Rietveld analyses indicated four different adsorption sites. Interestingly, the first adsorption site was near the BTC linkers instead of the metal centers. The H_2 adsorption site was 3.7 Å from the benzene rings and 4.27 Å from the exposed Y^{3+} ions. As H_2 loading increased, the site reached near-saturation and other sites were also occupied with H_2. The second site was located in the pores at a distance of 3.6 Å from the benzene ring and 3.9 Å from the open Y^{3+} ion. The third site was about 2.96 Å from the six BTC oxygen atoms and 4.3 Å from the Y^{3+} ions. The fourth adsorption was comparatively very weaker and located at 3.23 Å from the two BTC carboxylate oxygen atoms and 3.31 Å from two BTC carboxylate carbon atoms. This result demonstrates that an optimal pore size of about 6 Å enhances the interaction between the framework and H_2 molecules rather than the presence of open metal sites, giving a new direction in the synthesis of MOFs optimized for H_2 storage.

In situ neutron diffraction experiments have been conducted on MIL-53 (Cr) in order to identify the preferred adsorption sites as well as the mechanism of H_2 (deuterium) adsorption in the framework.[344] A fully deuterated sample of MIL-53 was used to eliminate the large incoherent background of the protons in the neutron diffraction experiment. The data for the powder samples collected at 10 K indicated that the sites near the Cr−O cluster were occupied first and then the site near the blunt corner. At higher loading, the D_2 molecules occupied the sides of the benzene rings, and the central part of the framework was occupied when D_2 adsorption reached saturation. The H_2 site occupations at various stages of loading were also measured at 25−140 K and 2 bar, and the results showed that the preferred site was independent of the temperature. The adsorption capacity reached saturation (5.5 wt %) at low temperature (below the freezing point of H_2), but many sites were still unoccupied because of the limited space and the van der Waals repulsions between the H_2 molecules.

Yildirim et al. revealed the H_2 adsorption sites in ZIF-8 at 3.5 K.[345] Contrary to MOFs, the strongest H_2 adsorption site was close to the C═C bond of the imidazolate organic linker. The other adsorption sites were at the center of the channel. This suggests that to increase the H_2 adsorption capacity, one must modify the organic linker instead of the central metal atom.

Powder neutron diffraction experiments were conducted at 4 K on Cu-BTT.[273] The framework showed a H_2 uptake capacity of 2.42 wt % at 77 K and 900 Torr. The diffraction data indicated that H_2 adsorption occurred 2.47 Å from the exposed Cu^{2+} ions. As the H_2 loading increased, the site occupancy reached about 93%. The next strong site also had similar binding energy as the

dx.doi.org/10.1021/cr200274s |*Chem. Rev.* 2012, 112, 782–835

first site and was situated ca. 3.46 Å from the framework's Cl^- ions and within van der Waals contact with the tetrazolate rings. The other sites were located near the tetrazolate and the benzene rings.

The NPD measurement of NOTT-112 indicated that there were differences in the H_2−Cu(II) interaction among the exposed Cu(II) sites.[275] NOTT-112 has rht topology consisting of cuboctahedral cages (Figure 46). NPD studies were performed on the framework with different degrees of loading (0.5, 1.0, 1.5, and 2.0 D_2 per Cu). On loading 0.5 D_2 per Cu, the strongest site was near CuA (2.23 Å) and the second site was near CuB (2.41 Å) (Figure 46). It was found that 85% of the D_2 from the first dosing coordinates to CuA. The presence of CuA inside the cuboctahedral cage increases the CuA−D_2 interaction, while CuB is located outside the cage. On higher loading, sites A3 (near phenyl ring), A4, A5 start to be occupied. This is the first report showing the differences of the adsorption sites that are chemically equivalent.

According to above results reported by various research groups, the strongest adsorption sites are the open transition metal sites, although the strongest binding site for H_2 depends on the type of MOF. In the absence of open metal sites, the organic linkers become dominant binding sites for H_2 molecules.

5.4.2. Inelastic Neutron Scattering. Inelastic neutron scattering (INS) spectroscopy can be used to get information about the number of individual binding sites when H_2 molecules are loaded in a MOF. In INS, the energy transfer from neutrons to the host is measured. In a H_2 molecule, the lowest rotational transition from ortho (parallel ^1H spins) to para form (antiparallel ^1H spins) occurs at 14.7 meV. This transition is highly influenced by the chemical environment around the H_2 molecule. INS spectroscopy detects the change in the nuclear spin transition for the H_2 molecule, which provides fine details about the chemical environment of the adsorbed H_2 molecule. During the measurement, the sample is degassed and cooled to 15 K and a blank INS spectrum is measured. Then a measured amount of H_2 is loaded to the container and the sample is warmed to a temperature between 40 and 100 K to allow the H_2 to be adsorbed by the sample. Then the sample is cooled to 15 K and the INS spectrum is measured.

Yaghi et al. have used INS spectroscopy to find the specific H_2 binding sites in the series of IRMOF such as IRMOF-1, IRMOF-8, IRMOF-11, and MOF-177.[346] All of these MOFs are chemically similar and the relatively stronger adsorption sites are located near the carboxylate group and then near the $[Zn_4O]$ cluster units. The binding of H_2 at the inorganic cluster sites is affected by the nature of the organic linker and is strongest in IRMOF-11, coincident with the adsorption isotherm data. In MOFs, the sites on organic linkers have lower binding energies but a much greater capacity for H_2 loading. The results demonstrate the importance of the organic linker for H_2 storage in the MOFs.

Cheetham and co-workers have used INS spectra to analyze the H_2 sorption sites in a Ni MOF, $NaNi_3(OH)(SIP)_2$ [SIP = 5-sulfoisophthalate].[230] The INS spectra revealed that the first H_2 sorption sites were the unsaturated Ni^{2+} sites on the activated framework, where H_2 molecules were adsorbed via chemisorption. On higher H_2 loading, H_2 molecules were adsorbed on other parts by weak physisorption.

Zhou and co-workers have used INS spectroscopy to study and compare the binding sites in catenated and noncatenated frameworks.[242] The INS spectra of the two frameworks appear to be similar due to the similar chemical compositions. The INS spectra of both isomers indicate that the initial site of the H_2 adsorption is the open Cu center of the paddle-wheel SBU. The H_2 interaction with the organic linker increases as the H_2 loading increases. The interaction of H_2 with the organic linker in the catenated framework is stronger than the noncatenated framework, indicating that catenation favors H_2 adsorption by offering a higher number of effective H_2 binding sites.

5.4.3. Variable Temperature Infrared Spectroscopy. IR spectroscopy can be used to track the change in the H_2 molecules on adsorption at the active site of the MOFs. Normally, the H_2 molecule is IR inactive, but it becomes IR active when it is adsorbed on the MOF surface. The H−H bond becomes polarized and the H−H stretching mode is shifted to a lower frequency. The shifts observed for the different interaction sites are large because of the single bond perturbation in H_2. Therefore, the different adsorption sites can be easily identified, even if they have very similar interaction energies. That is, the different adsorption sites provide distinctly different IR peaks for the adsorbed molecule and the shift in the IR frequency depends on the strength of the binding site, and the binding energy of any specific site can be easily measured.

Variable-temperature infrared spectroscopy was used to verify the H_2−framework interaction in MOF-5 at 15 K.[347] Two doublets, at 4088−4093 and 4175−4181 cm^{-1}, were used to characterize the interaction. On H_2 adsorption in the MOF, the above bands were broadened and blue-shifted. New peaks appeared at 4110−4150 cm^{-1} and a doublet at 4112 and 4121 cm^{-1} dominated at low H_2 loading. With increasing the H_2 pressure, a new band at 4130 cm^{-1} became predominant. The binding enthalpies estimated for the low- and high-pressure sites were 7.4 and 3.5 kJ mol^{-1}, respectively.

By using IR spectroscopy, the interactions between H_2 and the HKUST-1 framework were studied.[348] As the temperature was decreased under an H_2 pressure of 50 mbar, parallel growth of two bands at 4097 and 4090 cm^{-1} was observed, indicating the *ortho*- and *para*-H_2 adsorption on Cu^{2+} sites. The adsorption energy was about 10 kJ mol^{-1} for the system.

Chabal and co-workers also detected the H_2 binding sites in various MOFs at 300 K and high pressures (27−55 bar) by using IR spectroscopy.[349] The study revealed that the organic linkers were weakly perturbed upon incorporation of guest molecules and that the H_2 stretch mode was red-shifted. With a structure of type $M(bdc)(ted)_{0.5}$ (ted = triethylenediamine), H_2 interacts with the benzene ring instead of the metal centers. The perturbation of H_2 molecules depends on the sensitivity of the binding sites. The H_2 perturbation increases linearly with increasing the H_2 pressure, and the IR intensity varies depending on the number of benzene rings interacting with the H_2 molecules.

6. CONCLUSION AND PROSPECTS

As reviewed in this article, MOFs have versatile structures, high surface areas, and high pore volumes, and thus can be regarded as good candidate materials for H_2 storage. There are many MOFs that have high H_2 adsorption capacities at low temperatures, typically at 77 or 87 K. The highest H_2 storage capacity reported so far is 99.5 mg g^{-1} at 77 K and 56 bar for NU-100. However, the high H_2 capacities of MOFs at cryogenic temperatures dramatically decrease as the temperature increases to room temperature. This is because the H_2 adsorption in MOFs is weak physisorption and the interaction energies between the H_2 molecules and frameworks are very low.

The H_2 adsorption capacities at 77 K and high pressures (up to 100 atm) have a qualitative relationship with the surface areas of MOFs: as surface area increases, the H_2 capacity at 77 K also increases. To increase the surface areas of MOFs, various strategies have been employed, such as using polycarboxylate ligands as organic building blocks, elongation of the ligands, creation of catenated frameworks, and employing mixed ligands in the synthesis of MOFs. MOFs constructed from hexacarboxylic acid have higher surface areas and pore volumes than those from corresponding di-, tri-, or tetracarboxylates and display relatively high H_2 storage capacities. Despite a relatively low isosteric heat of H_2 adsorption, the MOFs constructed from hexacarboxylic acid and with open copper sites have the highest excess H_2 uptake capacity at 77 K reported to date. MOFs synthesized from the extended organic building blocks provide increased surface areas but tend to interpenetrate or collapse after removal of guest solvent molecules, leading to a reduced surface area or even a nonporous structure.

In order to apply a MOF as a H_2 gas storage material, the MOF should store large amounts of H_2 at ambient temperature. The DOE targets that should be achieved by 2017 are 5.5 wt % and 45 g L^{-1} at −40−60 °C under the maximum delivery pressure of 100 atm. In order to achieve this, the framework should have a high H_2 adsorption enthalpy. Theoretical calculations have predicted that the material should have a 15−25 kJ mol^{-1} of isosteric heat of H_2 adsorption in order to store H_2 gas at ca. 30 bar and to release at ca. 1.5 bar,[170] but most of the porous MOFs reported so far have isosteric heat of the H_2 adsorption in the range of 5−12 kJ mol^{-1}.

To increase the interaction energy between H_2 molecules and MOFs surface, also known as Q_{st}, various methods have been employed such as generating open metal sites, constraining pore size, catenation, ligand functionalization, alkali metal ion or alkaline-earth metal ion inclusion, doping with metal ions, and embedding MOFs with Pd or Pt nanoparticles.

Creating open metal sites at the metal cluster nodes or in the organic linkers definitely increases the isosteric heat of H_2 adsorption, which may lead to improved H_2 storage at room temperature. The highest isosteric heat of H_2 adsorption reported so far is 15 kJ mol^{-1} for a Co(II) MOF where every Co(II) site contains an open metal site together with a Co−Co distance appropriate for the side-on interaction with a H_2 molecule.[168] In an effort to increase the isosteric heat of H_2 adsorption, one may also design and synthesize new MOFs by using the functional ligands having open metal sites such as porphyrins or macrocyclic complexes, which has never been proven to have good H_2 storage capacity. Another approach to increase the isosteric heat of H_2 adsorption is to constrain pore size. However, the relationship between pore sizes and surface areas of MOFs reported so far shows that MOFs with smaller pores have smaller surface areas and MOFs with larger pores have larger surface area. Therefore, more studies should be done for optimization of pore size and surface area. It is a challenge to generate a high concentration of open metal sites in a MOF and achieve the ideal case such that each metal binds more than one H_2 molecule.

Even though there has been no systematic study, initial studies reveal that catenation enhances room temperature H_2 storage capacities of MOFs.[242,243] Recent reports demonstrated that the degree of catenation can even be controlled by the design of molecular building blocks and the template molecules.

There have also been extensive efforts to increase the isosteric heat of H_2 adsorption in high surface area MOFs through postsynthetic modifications. Contrary to expectations, the incorporation of small metal ions with high charge density in the MOF could only slightly increase the isosteric heat of H_2 adsorption. This is because the solvent molecules bound to the introduced metal ions could not be removed by activation. In this respect, it is worthwhile trying the following approach: searching for suitable metal ions that can dope the MOFs without coordinating solvent molecules or developing MOFs that have extraordinary high thermal stability so that metal-doped MOFs can be activated at a high temperature without collapsing the frameworks. DFT-PBE calculations have shown that the binding energies to H_2 molecules are 21.9, 34.6, and 46.5 kJ mol^{-1} for Sc, Ti, and V in MOFs, respectively.[350] Therefore, one may synthesize MOFs constructed of these metal ions and then generate open metal sites to see their effects on H_2 storage.

The embedding of Pd or Pt nanoparticles definitely enhances room temperature H_2 storage, but problems arise from the reduced pore volume and surface area caused by blocking of the pores by the embedded nanoparticles, in addition to their sensitivity toward air.[134] However, doping MOFs with catalysts is still an effective approach to increase hydrogen storage capacities at ambient temperature because H_2 adsorption in MOFs promoted by metal-catalysts will take place by atomic hydrogen instead of molecular hydrogen, which will provide a high adsorption enthalpy much greater than 20 kJ mol^{-1}.

To achieve high H_2 storage at room temperature in a MOF, the MOF should have not only a high isosteric heat of H_2 adsorption but also a very high surface area and pore volume. There have been some MOFs with comparatively large isosteric heats of adsorption; however, their surface areas and the pore volumes were too low to store a large amount of H_2 gas.[134,235,351] A synthetic strategy should be developed to construct a MOF incorporating a highly interacting surface while generating a large surface area with low dead volume.

One must keep in mind that the discovery of a MOF with a large surface area and high H_2 adsorption energy at room temperature does not guarantee that it will be applied as a H_2 storage material. If a MOF is to be used in industry, it must be stable in the general working conditions. It should be comparatively inert toward moisture, air, and other gas impurities. Many MOFs, in particular, Zn(II)-carboxylate based MOFs, are unstable on contacting with the slightest amount of moisture in air and tend to adsorb much less amounts of H_2 gas once exposed to moisture, since weak metal-carboxylate bridges in the MOFs are easily dissociated by moisture.

For MOFs containing open metal sites, the exposure to moisture results in coordinating the water molecules from air, which leads to reduced H_2 uptake. Some MOFs are also decomposed in the presence of moisture due to the unstable SBUs. Most commonly reported MOFs are unstable to acids and bases and decompose immediately.[352] Recent research shows that ZIFs are relatively stable toward moisture and other harsh conditions, compared to the MOFs prepared from carboxylic acids. The stability may also depend on the metal ions employed in the synthesis of the MOFs, and therefore one has to find the right metal based MOFs. MOFs constructed of various metal ions belonging to group 1 through group 4 as well as other transition metal ions that have not been commonly used should be prepared, and their stabilities against moisture should be examined. Recently, it has been shown that MOFs synthesized from the ligands containing hydrophobic functional groups[353,354] and those with postsynthetically introduced hydrophobic functional groups enhance water resistance.[355] Therefore, when designing MOFs, one must keep in mind that strong metal−ligand bonds

should be made so that the MOF can be stable against moisture and also be thermally stable for complete desolvation to generate open metal sites without the collapse of the framework. One should also try to reduce the total cost of production of MOFs in a bulk scale synthesis by using readily available raw materials, instead of employing ligands that require a multistep organic synthesis.

To develop MOFs as H_2 storage materials that meet the U.S. DOE targets for an on-board hydrogen system, a serious challenge is still present in the design and synthesis of the MOF materials. We may expect that highly stable MOFs having a large surface area and pore volume, together with many open metal sites and embedded catalysts for hydrogen spillover, would provide some positive results for H_2 storage at ambient temperature.

AUTHOR INFORMATION

Corresponding Author

*Telephone: +82 2 880 7760; fax: +82 2 886 8516; e-mail: mpsuh@snu.ac.kr.

BIOGRAPHIES

Myunghyun Paik Suh is professor of Department of Chemistry at Seoul National University. She received her B.S. at Seoul National University (1971) and Ph.D. at the University of Chicago (1976), and she started her career as an assistant professor at the Seoul National University in 1977. Her current research interest is the development of energy and environment related materials based on coordination chemistry and nanoscience. She is a member of the Korean Academy of Science and Technology and has received the Korean Science Award offered by the President of Korea.

Hye Jeong Park received her B.S. (2006) and M.S. (2008) degrees in chemistry from Seoul National University. She is currently a Ph.D. student in inorganic chemistry at Seoul National University under the guidance of Prof. Myunghyun Paik Suh. Her research is focused on the design and synthesis of porous crystalline materials and their application in gas storage and separation as well as crystal dynamics.

Thazhe Kootteri Prasad received his Ph.D. in Chemistry in 2008 from the University of Hyderabad, India, under the guidance of Prof. M. V. Rajasekharan. In 2008, he joined the group of Prof. Myunghyun Paik Suh at Seoul National University as a post-doctoral researcher. From 2010 to 2011 he worked with Prof. Andrea Cornia at University of Modena and Reggio Emilia, Italy, researching single molecule based magnets. He is currently in Suh's lab, working on the porous materials suitable for sensing and gas storage applications.

Dae-Woon Lim received his B.S. (2009) degree in chemistry from DanKook University in Korea. He is currently a Ph.D. student at Seoul National University, working on porous materials and nanocomposites for hydrogen storage under the guidance of Prof. Myunghyun Paik Suh.

ACKNOWLEDGMENT

This work was supported by National Research Foundation of Korea (NRF) Grants funded by the Korean Government (MEST) (Nos. 2010-0029651 and 2011-0001341).

LIST OF ABBREVIATIONS

abtc	1,1′-azobenzene-3,3′,5,5′-tetracarboxylate
abtt	5,5′,5″-(2-aminobenzene-1,3,5-triyl)tris(ethyne-2,1-diyl)triisophthalic acid
acac	acetylacetonate

adc	9,10-anthracenedicarboxylate
abdc	4,4′-azobenzenedicarboxylate
adip	5,5′-(9,10-anthracenediyl)diisophthalate
aobtc	azoxybenzene-3,3′,5,5′-tetracarboxylate
APS	3-aminopropyltrialkoxysilane
azd	1,3-azulenedicarboxylate
BBC	4,4′,4″-[benzene-1,3,5-trily tris(benzene-4,1-diyl)]-tribenzoate
BDC	benzene-1,4-dicarboxylate
bdcppi	*N*,*N*′-bis(3,5-dicarboxyphenyl)pyromellitic diimide
bddc/bdi	5,5′-(buta-1,3-diyne-1,4-diyl)diisophthalate
BDP	1,4-benzenedi(4′-pyrazolyl)
BDT	1,4-benzeneditetrazolate
bdpb	1,3-bis(3,5-dicarboxylphenylethynyl)benzene
BHB	3,3′,3″,5,5′,5″-benzene-1,3,5-triyl-hexabenzoate
bhtc	biphenyl-3,4′,5-tricarboxylate
bpdc	4,4′-biphenyldicarboxylate
bpe	1,2-bis(4-pyridyl)ethane
BPnDC	4,4′-benzophenone dicarboxylate
bpta	3,6-di(4-pyridyl)-1,2,4,5-tetrazine
bptc	1,1′-biphenyl-3,3′,5,5′-tetracarboxylate
bpy	bipyridine
bpydc	2,2′-bipyridyl-5,5′-dicarboxylate
bpytc	4,4′-bipyridine-2,6,2′,6′-tetracarboxylate
Brbdc	2-bromobenzene-1,4-dicarboxylate
btatb	4,4′,4″,4‴-benzene-1,2,4,5-tetrayltetrabenzoate (same as TCPB)
BTDD	bis(1H-1,2,3-triazolo[4,5-b],-[4′,5′-i])dibenzo[1,4]-dioxin
BTB	4,4′,4″-benzene-1,3,5-triyl-tribenzoate
BTC	benzene-1,3,5-tricarboxylate
BTE	4,4′,4″-[benzene-1,3,5-triyl-tris(ethyne-2,1-diyl)]tribenzoate
btei	5,5′,5″-benzene-1,3,5-triyltris(1-ethynyl-2-isophthalate)
BTT	1,3,5-benzenetristetrazolate
btti	5,5′,5″-(benzene-1,3,5-triyl-tris(biphenyl-4,4′-diyl))triisophthalate
cdc	1,12-dicarboxyl-1,12-dicabra-closo-dodecarborane
CF_3Py	4-(α,α,α-trifluoromethyl)pyridine
CMOF	chiral metal−organic framework
cnc	4-carboxycinnamate
cyclam	1,4,8,11-tetraazacyclotetradecane
dabco	1,4-diazabicyclo[2.2.2]octane
dbdc	1,2-dihydrocyclobutabenzene-3,6-dicarboxylate
dcbBn	6,6′-dichloro-2,2′-dibenzyloxy-1,1′-binaphthyl-4,4′-dibenzoate
dccptp	3,5-dicyano-4-(4-carboxyphenyl)-2,2′:6,4″-terpyridine
dcdEt	6,6′-dichloro-2,2′-diethoxy-1,1′-binaphthyl-4,4′-dibenzoate
DEF	diethylformamide
DETA	diethylenetriamine
dhtp	2,5-dihydroxyterephthalate
diPyNI	*N*,*N*′-di-(4-pyridyl)-1,4,5,8-naphthalenetetracarboxydiimide
diPyTz	3,6-di(4-pyridyl)-1,2,4,5-tetrazine (same as bpta)
DMF	dimethylformamide
DMOF	1,4-diazabicyclo[2.2.2]octane−MOF
dobdc	2,5-dioxido-1,4-benzenedicarboxylate
DPG	meso-1,2-bis(4-pyridyl)-1,2-ethanediol
dpt	3,6-di(4-pyridyl)-1,2,4,5-tetrazine (same as bpta)
ebdc	5,5′-(1,2-ethynediyl)bis(1,3-benzenedicarboxylate)
ED	ethylene diamine
EMC	entatic metal centers
EtPy	4-ethylpyridine
hfipbb	4,4′-(idene hexafluoroisopropylidene)-dibenzoate
fma	fumarate
F-pymo	5-fluoropyrimidin-2-olate
2F-4-TBA	2-fluoro-4-(1H-tetrazole-5-yl)benzoate
GCMC	Grand Canonical Monte Carlo
HKUST	Hong Kong University of Science and Technology
hpdc	4,5,9,10-tetrahydropyrene-2,7-dicarboxylate
HPP	1,3,4,6,7,8-hexahydro-2H-pyrimido[1,2-a]pyrimidine
ICP	inductively coupled plasma
IM	imidazolates
ImDC	4,5-imidazoledicarboxylate
IN	isonicotinate
INS	inelastic neutron scattering
IRMOF	isoreticular metal−organic framework
mdip	5,5′-methylene diisophthalate
MeIM	1-methylimidazole
MePy	4-methylpyridine
MIL	material from Institut Lavoisier
mna	mercaptonicotinate
MOF	metal-organic framework
MTB	methanetetrabenzoate
NDC	naphthalenedicarboxylate
NH_2-bdc	2-aminobenzene-1,4-dicarboxylate
NP	nanoparticle
NPD	neutron powder diffraction
NTB	4,4′,4″-nitrilotrisbenzoate
ntbd	4′,4″,4‴-nitrilotribiphenyl-3,5-dicarboxylate
ntc	naphthalene-1,4,5,8-tetracarboxylate
ntei	5,5′,5″-(4,4′,4″-nitrilotris(benzene-4,1-diyl)tris(ethyne-2,1-diyl))triisophthalate
NU	Northwestern University
ox	oxalate
oxdc	oxidiacetate
PBA	4-(4-pyridyl) benzoate
pbpc	pyridine-3,5-bis(phenyl-4-carboxylate)
PCN	porous coordination network
pda	*p*-phenylenediacylate
pdc	pyridinedicarboxylate
peip	5-(pyridin-3-ylethynyl)isophthalate
PmDC	4,6-pyrimidinedicarboxylate
pmip	5-[(pyridin-3-ylmethyl)amino]isophthalate
PMTB	diphenylmethane-3,3′,5,5′-tetrakis(3,5-bisbenzoate)
ppz	piperazine
ptei	5,5′-((5′-(4-((3,5-dicarboxyphenyl)ethynyl)phenyl)-[1,1′:3′,1″-terphenyl]-4,4″-diyl)-bis(ethyne-2,1-diyl))diisophthalate
pydc	pyrene-2,7-dicarboxylate
pyen	5-methyl-4-oxo-1,4-dihydropyridine-3-carbaldehyde
pymc	2-pyrimidinecarboxylate
pymo	pyrimidinolate
pyrdc	pyrene-2,7-dicarboxylate
qptc	quaterphenyl-3,3‴,5,5‴-tetracarboxylate
Q_{st}	isosteric heats of H_2 adsorption
RPM	robust porphyrinic material
sbtc	*trans*-stilbene-3,3′,5,5′-tetracarboxylate
SCD	supercritical CO_2 drying
SIP	5-sulfoisophthalate
SNU	Seoul National University

dx.doi.org/10.1021/cr200274s |*Chem. Rev.* 2012, 112, 782–835

TATB	4,4′,4″-s-triazine-2,4,6-triyltribenzoate
4-TBA	4-(1H-tetrazole-5-yl)benzoate
tbbdc	5-*tert*-butyl-1,3-benzenedicarboxylate
tbip	5-*t*-butyl isophthalate
tbtt	5,5′,5″-(2,4,6-trimethylbenzene-1,3,5-triyl)tris(ethyne-2,1-diyl)triisophthalate
TCBPA	tris(4-carboxybiphenyl)amine
TCM	tetrakis[4-(carboxyphenyl)-oxamethyl]methane
TCPB	1,2,4,5-tetrakis(4-carboxyphenyl)-benzene
TCPBDA	*N*,*N*,*N*′,*N*′-tetrakis(4-carboxyphenyl)biphenyl-4,4′-diamine
TDC	thiophene-2,5-dicarboxylate
tftpa	tetra-fluoroterephthalate
tcpdep	3,3′,5,5′-tetra(4-carboxyphenyl)-2,2′-diethoxylbiphenyl
TCPPDA	*N*,*N*,*N*′,*N*′-tetrakis(4-carboxyphenyl)-1,4-phenylenediamine
T^2DC	thieno[3,2-b]thiophene-2,5-dicarboxylate
ted	triethylenediamine
tfbdc	tetrafluoroterephthalate
THF	tetrahydrofuran
tmbdc	tetramethylterephthalate
TPB-3tz	1,3,5-tri-p-(tetrazol-5-yl)phenylbenzene
TPT-3tz	2,4,6-tri-p-(tetrazol-5-yl)phenyl-s-triazine
4,4′-tpcb	*rctt*-tetrakis (4-pyridyl)cyclobutane
3-tpt	2,4,6-tri(3-pyridyl)-1,3,5-triazine
4-tpt	2,4,6-tri(4-pyridyl)-1,3,5-triazine
tptc	terphenyl-3,3″,5,5″-tetracarboxylate
TPyP	5,10,15,20,-tetra-4-pyridyl-21*H*,23*H*-porphyrine
trz	1,2,4-triazolate
ttdc	thieno[3,2-b]thiophen-2,5-dicarboxylate
ttei	5,5′,5″-(((benzene-1,3,5-triyltris(ethyne-2,1-diyl))tris(benzene-4,1-diyl))tris-(ethyne-2,1-diyl))triisophthalate
ttpm	tetrakis(4-tetrazolylphenyl)methane
TUDMOF	Technical University of Dresden metal−organic framework
Tz	3,5-bis(trifluoromethyl)-1,2,4-triazolate
Tzc	tetrazolate-5-carboxylate
TZI	5-tetrazolylisophthalate
UMCM	University of Michigan crystalline material
UTSA	University of Texas at San Antonio
ViPy	4-vinylpyridine
ZIF	zeolitic imidazolate framework

REFERENCES

(1) http://www1.eere.energy.gov/hydrogenandfuelcells/ storage/current_technology.html.
(2) Sakintuna, B.; Lamari-Darkrimb, F.; Hirscher, M. *Int. J. Hydrogen Energy* **2007**, *32*, 1121.
(3) Schuth, F.; Bogdanovic, B.; Felderhoff, M. *Chem. Commun.* **2004**, 2249.
(4) Orimo, S.; Nakamori, Y.; Eliseo, J. R.; Züttel, A.; Jensen, C. M. *Chem. Rev.* **2007**, *107*, 4111.
(5) Grochala, W.; Edwards, P. P. *Chem. Rev.* **2004**, *104*, 1283.
(6) Christensen, C. H.; Sørensen, R. Z.; Johannessen, T.; Quaade, U. J.; Honkala, K.; Elmøe, T. D.; Køhler, R.; Nørskov, J. K. *J. Mater. Chem.* **2005**, *15*, 4106.
(7) Hugle, T.; Hartl, M.; Lentz, D. *Chem.—Eur. J.* **2011**, *17*, 10184.
(8) Alcaraz, G.; Sabo-Etienne, S. *Angew. Chem., Int. Ed.* **2010**, *49*, 7170.
(9) Hamilton, C. W.; Baker, R. T.; Staubitz, A.; Manners, I. *Chem. Soc. Rev.* **2009**, *38*, 279.
(10) Zhang, Y.-H. P. *Int. J. Hydrogen Energy* **2010**, *35*, 10334.
(11) Struzhkin, V. V.; Militzer, B.; Mao, W. L.; Mao, H.-k.; Hemley, R. J. *Chem. Rev.* **2007**, *107*, 4133.
(12) Chen, J.; Wu, F. *Appl. Phys. A: Mater. Sci. Process.* **2004**, *78*, 989.
(13) McKeown, N. B.; Budd, P. M. *Chem. Soc. Rev.* **2006**, *35*, 675.
(14) Cheng, H.-M.; Yang, Q.-H.; Liu, C. *Carbon* **2001**, *39*, 1447.
(15) Baughman, R. H.; Zakhidov, A. A.; de Heer, W. A. *Science* **2002**, *297*, 787.
(16) Strobel, R.; Garche, J.; Moseley, P. T.; Jorissen, L.; Wolf, G. *J. Power Sources* **2006**, *159*, 781.
(17) Yang, J.; Sudik, A.; Wolverton, C.; Siegel, D. J. *Chem. Soc. Rev.* **2010**, *39*, 656.
(18) Morris, R. E.; Wheatley, P. S. *Angew. Chem., Int. Ed.* **2007**, *47*, 4966.
(19) van den Berg, A. W. C.; Arean, C. O. *Chem. Commun.* **2008**, 668.
(20) David, W. I. F. *Faraday Discuss.* **2011**, *151*, 399.
(21) Fakioglu, E.; Yurum, Y.; Veziroglu, T. N. *Int. J. Hydrogen Energy* **2004**, *29*, 1371.
(22) Jena, P. *J. Phys. Chem. Lett.* **2011**, *2*, 206.
(23) Cohen, R. L.; Wernick, J. H. *Science* **1981**, *214*, 1081.
(24) Schlapbach, L.; Züttel, A. *Nature* **2001**, *414*, 353.
(25) Everett, D. H. *Pure Appl. Chem.* **1972**, *31*, 577.
(26) Burwell, R L, Jr. *Pure Appl. Chem.* **1976**, *46*, 71.
(27) Calvert, J. G. *Pure Appl. Chem.* **1990**, *62*, 2167.
(28) Farha, O. K.; Yazaydin, A. O.; Eryazici, I.; Malliakas, C. D.; Hauser, B. G.; Kanatzidis, M. G.; Nguyen, S. T.; Snurr, R. Q.; Hupp, J. T. *Nat. Chem.* **2010**, *2*, 944.
(29) Furukawa, H.; Ko, N.; Go, Y. B.; Aratani, N.; Choi, S. B.; Choi, E.; Yazaydin, A. O.; Snurr, R. Q.; O'Keeffe, M.; Kim, J.; Yaghi, O. M. *Science* **2010**, *329*, 424.
(30) Rosi, N. L.; Eckert, J.; Eddaoudi, M.; Vodak, D. T.; Kim, J.; O'Keeffe, M.; Yaghi, O. M. *Science* **2003**, *300*, 1127.
(31) Kaye, S. S.; Dailly, A.; Yaghi, O. M.; Long, J. R. *J. Am. Chem. Soc.* **2007**, *129*, 14176.
(32) Sculley, J.; Yuan, D.; Zhou, H.-C. *Energy Environ. Sci.* **2011**, *4*, 2721.
(33) Lin, X.; Champness, N. R.; Schröder, M. *Top. Curr. Chem.* **2010**, *293*, 35.
(34) Hu, Y. H.; Zhang, L. *Adv. Mater.* **2010**, *22*, E117.
(35) Ma, S.; Zhou, H.-C. *Chem. Commun.* **2010**, *46*, 44.
(36) Han, S. S.; Mendoza-Cortes, J. L.; Goddard, W. A. *Chem. Soc. Rev.* **2009**, *38*, 1460.
(37) Murray, L. J.; Dincă, M.; Long, J. R. *Chem. Soc. Rev.* **2009**, *38*, 1294.
(38) Dincă, M.; Long, J. R. *Angew. Chem., Int. Ed.* **2008**, *47*, 6766.
(39) Lin, X.; Jia, J.; Hubberstey, P.; Schröder, M.; Champness, N. R. *CrystEngComm* **2007**, *9*, 438.
(40) Lowell, S.; Shields, J. E.; Thomas, M. A.; Thommes, M. *Characterization of Porous Solids and Powders Surface Area, Pore Size and Density*; Springer (originally by Kluwer Academic Publishers): New York, 2004.
(41) Marsh, H. *Carbon* **1987**, *25*, 49.
(42) Walton, K. S.; Snurr, R. Q. *J. Am. Chem. Soc.* **2007**, *129*, 8552.
(43) Duren, T.; Millange, F.; Férey, G.; Walton, K. S.; Snurr, R. Q. *J. Phys. Chem. C* **2007**, *111*, 15350.
(44) Salem, M. M. K.; Braeuer, P.; Szombathely, M. v.; Heuchel, M.; Harting, P.; Quitzsch, K.; Jaroniec, M. *Langmuir* **1998**, *14*, 3376.
(45) Furukawa, H.; Miller, M. A.; Yaghi, O. M. *J. Mater. Chem.* **2007**, *17*, 3197.
(46) Sircar, S. *Ind. Eng. Chem. Res.* **1999**, *38*, 3670.
(47) Myers, A. L.; Calles, J. A.; Calleja, G. *Adsorption* **1997**, *3*, 107.
(48) Dincă, M.; Dailly, A.; Liu, Y.; Brown, C. M.; Neumann, D. A.; Long, J. R. *J. Am. Chem. Soc.* **2006**, *128*, 16876.
(49) Czepirski, L.; Jagiello, J. *Chem. Eng. Sci.* **1989**, *44*, 797.
(50) R program http://www.R-project.org.
(51) Cole, J. H.; Everett, D. H.; Marshall, C. T.; Paniego, A. R.; Powl, J. C; Rodriguez-Reinoso, F. *J. Chem. Soc. Faraday Trans.* **1974**, *70*, 2154.

(52) Yang, R. T. *Gas Separation by Adsorption Process*; Butterworth: Boston, 1997.
(53) Cahill, C. L.; de Lilla, D. T.; Frisch, M. *CrystEngComm* **2007**, *9*, 15.
(54) Wang, Y.; Cheng, P.; Chen, J.; Liao, D.-Z.; Yan, S.-P. *Inorg. Chem.* **2007**, *46*, 4530.
(55) Shultz, A. M.; Farha, O. K.; Hupp, J. T.; Nguyen, S. T. *J. Am. Chem. Soc.* **2009**, *131*, 4204.
(56) Chen, B.; Liang, C.; Yang, J.; Contreras, D. S.; Clancy, Y. L.; Lobkovsky, E. B.; Yaghi, O. M.; Dai, S. *Angew. Chem., Int. Ed.* **2006**, *45*, 1390.
(57) Park, H. J.; Suh, M. P. *Chem.—Eur. J.* **2008**, *14*, 8812.
(58) O'Keeffe, M.; Yaghi, O. M. *Chem. Rev.* **2012**, DOI: 10.1021/cr200205j.
(59) Eddaoudi, M.; Kim, J.; Rosi, N.; Vodak, D.; Wachter, J.; O'Keeffe, M.; Yaghi, O. M. *Science* **2002**, *295*, 469.
(60) Rowsell, J. L. C.; Millward, A. R.; Park, K. S.; Yaghi, O. M. *J. Am. Chem. Soc.* **2004**, *126*, 5666.
(61) Rowsell, J. L. C.; Yaghi, O. M. *J. Am. Chem. Soc.* **2006**, *128*, 1304.
(62) Wong-Foy, A. G.; Matzger, A. J.; Yaghi, O. M. *J. Am. Chem. Soc.* **2006**, *128*, 3494.
(63) Müller, M.; Turner, S.; Lebedev, O. I.; Wang, Y.; Tendeloo, G. v.; Fischer, R. A. *Eur. J. Inorg. Chem.* **2011**, *25*, 1878.
(64) Esken, D.; Zhang, X.; Lebedev, O. I.; Schröder, F.; Fischer, R. A. *J. Mater. Chem.* **2009**, *19*, 1314.
(65) Müller, M.; Hermes, S.; Khler, K.; van den Berg, M. W. E.; Muhler, M.; Fischer, R. A. *Chem. Mater.* **2008**, *20*, 4576.
(66) Schröder, F.; Esken, D.; Cokoja, M.; van den Berg, M. W. E.; Lebedev, O. I.; Tendeloo, G. V.; Walaszek, B.; Buntkowsky, G.; Limbach, H.-H.; Chaudret, B.; Fischer, R. A. *J. Am. Chem. Soc.* **2008**, *130*, 6119.
(67) Han, S.; Wei, Y.; Valente, C.; Lagzi, I.; Gassensmith, J. J.; Coskun, A.; Stoddart, J. F.; Grzybowski, B. A. *J. Am. Chem. Soc.* **2010**, *132*, 16358.
(68) Liu, B.; Shioyama, H.; Akita, T.; Xu, Q. *J. Am. Chem. Soc.* **2008**, *130*, 5390.
(69) Li, Y.; Yang, R. T. *J. Am. Chem. Soc.* **2006**, *128*, 726.
(70) Kaye, S. S.; Long, J. R. *J. Am. Chem. Soc.* **2008**, *130*, 806.
(71) Chae, H. K.; Siberio-Perez, D. Y.; Kim, J.; Go, Y.; Eddaoudi, M.; Matzger, A. J.; O'Keeffe, M.; Yaghi, O. M. *Nature* **2004**, *427*, 523.
(72) Koh, K.; Wong-Foy, A. G.; Matzger, A. J. *J. Am. Chem. Soc.* **2009**, *131*, 4184.
(73) Chui, S. S. Y.; Lo, S. M. F.; Charmant, J. P. H; Orpen, A. G.; Williams, I. D. *Science* **1999**, *283*, 1148.
(74) Zhou, W.; Wu, H.; Yildirim, T. *J. Am. Chem. Soc.* **2008**, *130*, 15268.
(75) Lin, X.; Telepeni, I.; Blake, A. J.; Dailly, A.; Brown, C. M.; Simmons, J. M.; Zoppi, M.; Walker, G. S.; Thomas, K. M.; Mays, T. J.; Hubberstey, P.; Champness, N. R.; Schröder, M. *J. Am. Chem. Soc.* **2009**, *131*, 2159.
(76) Lee, Y.-G.; Moon, H. R.; Cheon, Y. E.; Suh, M. P. *Angew. Chem., Int. Ed.* **2008**, *47*, 7741.
(77) Ma, B.- Q.; Mulfort, K. L.; Hupp, J. T. *Inorg. Chem.* **2005**, *44*, 4912.
(78) Park, H. J.; Cheon, Y. E.; Suh, M. P. *Chem.—Eur. J.* **2010**, *16*, 11662.
(79) Horike, S.; Matsuda, R.; Tanaka, D.; Matsubara, S.; Mizuno, M.; Endo, K.; Kitagawa, S. *Angew. Chem., Int. Ed* **2006**, *45*, 7226.
(80) Chen, B.; Ma, S.; Hurtado, E. J.; Lobkovsky, E. B.; Zhou, H. C. *Inorg. Chem.* **2007**, *46*, 8490.
(81) Henke, S.; Fischer, R. A. *J. Am. Chem. Soc.* **2011**, *133*, 2064.
(82) Férey, G.; Mellot-Draznieks, C.; Serre, C.; Millange, F.; Dutour, J.; Surble, S.; Margiolaki, I. *Science* **2005**, *309*, 2040.
(83) Férey, G.; Serre, C.; Mellot-Draznieks, C.; Millange, F.; Surble, S.; Dutour, J.; Margiolaki, I. *Angew. Chem., Int. Ed.* **2004**, *43*, 6296.
(84) Latroche, M.; Suble, S.; Serre, C.; Mellot-Draznieks, C.; Llewellyn, P. L.; Lee, J.-H.; Chang, J.-S.; Jhung, S. H.; Férey, G. *Angew. Chem., Int. Ed.* **2006**, *45*, 8227.
(85) Liu, Y.; Eubank, J. F.; Cairns, A. J.; Eckert, J.; Kravtsov, V. C.; Luebke, R.; Eddaoudi, M. *Angew. Chem., Int. Ed.* **2007**, *46*, 3278.
(86) Zheng, S.-T.; Bu, J.-T.; Li, Y.; Wu, T.; Zuo, F.; Feng, P.; Bu, X. *J. Am. Chem. Soc.* **2010**, *132*, 17062.
(87) Yang, S. H.; Lin, X.; Blake, A. J.; Walker, G. S.; Hubberstey, P.; Champness, N. R.; Schröder, M. *Nat. Chem.* **2009**, *1*, 487.
(88) Ma, S.; Zhou, H.-C. *J. Am. Chem. Soc.* **2006**, *128*, 11734.
(89) Li, Y.; Xie, L.; Liu, Y.; Yang, R.; Li, X. *Inorg. Chem.* **2008**, *47*, 10372.
(90) Mallick, A.; Saha, S.; Pachfule, P.; Roy, S.; Banerjee, R. *J. Mater. Chem.* **2010**, *20*, 9073.
(91) Senkovska, I.; Kaskel, S. *Eur. J. Inorg. Chem.* **2006**, *20*, 4564.
(92) Cheon, Y.-E.; Park, J.; Suh, M. P. *Chem. Commun.* **2009**, *45*, 5436.
(93) Gedrich, K.; Senkovska, I.; Klein, N.; Stoeck, U.; Henschel, A.; Lohe, M. R.; Baburin, I. A.; Mueller, U.; Kaskel, S. *Angew. Chem. Int. Ed.* **2010**, *49*, 8489.
(94) Lee, Y. E.; Jang, S. Y.; Suh, M. P. *J. Am. Chem. Soc.* **2005**, *127*, 6374.
(95) Suh, M. P.; Cheon, Y. E.; Lee, E. Y. *Chem.—Eur. J.* **2007**, *13*, 4208.
(96) Tian, Y.-Q.; Cai, C.-X.; Ji, Y.; You, X.-Z.; Peng, S.-M.; Lee, G.-H. *Angew. Chem., Int. Ed.* **2002**, *41*, 1384.
(97) Tian, Y.-Q.; Cai, C.-X.; Ren, X.-M.; Duan, C.-Y.; Xu, Y.; Gao, S.; You, X.-Z. *Chem.—Eur. J.* **2003**, *9*, 5673.
(98) Tian, Y.-Q.; Chen, Z.-X.; Weng, L.-H.; Guo, H.-B.; Gao, S.; Zhao, D.-Y. *Inorg. Chem.* **2004**, *43*, 4631.
(99) Tian, Y.-Q.; Zhao, Y.-M.; Chen, Z.-X.; Zhang, G.-N.; Weng, L.-H.; Zhao, D.-Y. *Chem.—Eur. J.* **2007**, *13*, 4146.
(100) Park, K. S.; Ni, Z.; Cote, A. P.; Choi, J. Y.; Huang, R.; Uribe-Romo, F. J.; Chae, H. K.; O'Keeffe, M.; Yaghi, O. M. *Proc. Natl. Acad. Sci. U.S.A.* **2006**, *103*, 10186.
(101) Banerjee, R.; Phan, A.; Wang, B.; Knobler, C.; Furukawa, H.; O'Keeffe, M.; Yaghi, O. M. *Science* **2008**, *319*, 939.
(102) Wang, B.; Côté, A. P.; Furukawa, H.; O'Keeffe, M.; Yaghi, O. M. *Nature* **2008**, *453*, 207.
(103) Hayashi, H.; Côté, A. P.; Furukawa, H.; O'Keeffe, M.; Yaghi, O. M. *Nat. Mater.* **2007**, *6*, 501.
(104) Phan, A.; Doonan, C.; Uribe-Romo, F. J.; Knobler, C. B.; O'keeffe, M.; Yaghi, O. M. *Acc. Chem. Res.* **2009**, *43*, 58.
(105) Choi, H. J.; Dincă, M.; Long, J. R. *J. Am. Chem. Soc.* **2008**, *130*, 7848.
(106) Aromi, G.; Barrios, L. A.; Gamez, P. *Coord. Chem. Rev.* **2011**, *255*, 485.
(107) Demessence, A.; D'Alessandro, D. M.; Foo, M. L.; Long, J. R. *J. Am. Chem. Soc.* **2009**, *131*, 8784.
(108) Yang, C.; Wang, X.; Omary, M. A. *J. Am. Chem. Soc.* **2007**, *129*, 1545.
(109) Zhang, J.-P.; Chen, X.-M. *J. Am. Chem. Soc.* **2008**, *130*, 6010.
(110) Zhang, J.-P.; Lin, Y.-Y.; Huang, X. -C.; Chen, X.-M. *J. Am. Chem. Soc.* **2005**, *127*, 5495.
(111) Zhu, A.-X.; Lin, J.-B.; Zhang, J.-P.; Chen, X.-M. *Inorg. Chem.* **2009**, *48*, 3882.
(112) Dincă, M.; Long, J. R. *J. Am. Chem. Soc.* **2007**, *129*, 11172.
(113) Dincă, M.; Dailly, A.; Tsay, C.; Long, J. R. *Inorg. Chem.* **2008**, *47*, 11.
(114) Dincă, M.; Yu, A. F.; Long, J. R. *J. Am. Chem. Soc.* **2006**, *128*, 8904.
(115) Chun, H.; Dybtsev, D. N.; Kim, H.; Kim, K. *Chem.—Eur. J.* **2005**, *11*, 3521.
(116) Park, H. J.; Suh, M. P. *Chem. Commun.* **2010**, *46*, 610.
(117) Koh, K.; Wong-Foy, A. G.; Matzger, A. J. *Angew. Chem., Int. Ed.* **2008**, *47*, 677.
(118) Koh, K.; Wong-Foy, A. G.; Matzger, A. J. *J. Am. Chem. Soc.* **2010**, *132*, 15005.
(119) Pichon, A.; Lazuen-Garay, A.; James, S. L. *CrystEngComm* **2006**, *8*, 211.
(120) Liu, Y.; Kravtsov, V. Ch.; Beauchamp, D. A.; Eubank, J. F.; Eddaoudi, M. *J. Am. Chem. Soc.* **2005**, *127*, 7266.
(121) Xiang, S.; Huang, J.; Li, L.; Zhang, J.; Jiang, L.; Kuang, X.; Su, C.-Y. *Inorg. Chem.* **2011**, *50*, 1743.

(122) Eubank, J. F.; Wojtas, L.; Hight, M. R.; Bousquet, T.; Kravtsov, V. Ch.; Eddaoudi, M. *J. Am. Chem. Soc.* 2011, *133*, 17532–17535.
(123) Das, M. C.; Xu, H; Xiang, S.; Zhang, Z.; Arman, H. D.; Qian, G.; Chen, B. *Chem.—Eur. J.* **2011**, *17*, 7817.
(124) Nouar, F.; Eubank, J. F.; Bousquet, T.; Wojtas, L.; Zaworotko, M. J.; Eddaoudi, M. *J. Am. Chem. Soc.* **2008**, *130*, 1833.
(125) Suh, M. P.; Moon, H. R. *Adv. Inorg. Chem.* **2007**, *59*, 39.
(126) Suh, M. P.; Cheon, Y. E.; Lee, E. Y. *Coord. Chem. Rev.* **2008**, *252*, 1007.
(127) Lee, E. Y.; Suh, M. P.; Ko, J. W.; Choi, H. J. *J. Am. Chem. Soc.* **2002**, *124*, 10976.
(128) Choi, H. J.; Suh, M. P. *J. Am. Chem. Soc.* **2004**, *126*, 15844.
(129) Lee, E. Y.; Suh, M. P. *Angew. Chem., Int. Ed.* **2004**, *43*, 2798.
(130) Moon, H. R.; Kim, J. H.; Suh, M. P. *Angew. Chem., Int. Ed.* **2005**, *44*, 1261.
(131) Suh, M. P.; Moon, H. R.; Lee, E. Y.; Jang, S. Y. *J. Am. Chem. Soc.* **2006**, *128*, 4710.
(132) Cheon, Y. E.; Suh, M. P. *Chem.—Eur. J.* **2008**, *14*, 3961.
(133) Moon, H. R.; Suh, M. P. *Eur. J. Inorg. Chem.* **2010**, *24*, 3795.
(134) Cheon, Y. E.; Suh, M. P. *Angew. Chem., Int. Ed.* **2009**, *48*, 2899.
(135) Choi, H. J.; Suh, M. P. *J. Am. Chem. Soc.* **1998**, *120*, 6309.
(136) Choi, H. J.; Suh, M. P. *Angew. Chem., Int. Ed.* **1999**, *38*, 1405.
(137) Ko, J. W.; Min, K. S.; Suh, M. P. *Inorg. Chem.* **2002**, *41*, 2151.
(138) Suh, M. P.; Choi, H. J.; So, S. M.; Kim, B. M. *Inorg. Chem.* **2003**, *42*, 676.
(139) Kim, H.; Suh, M. P. *Inorg. Chem.* **2005**, *44*, 810.
(140) Reguera, L.; Krap, C. P.; Balmaseda, J.; Reguera, E. *J. Phys. Chem. C* **2008**, *112*, 15893.
(141) Kaye, S. S.; Long, J. R. *Chem. Commun.* **2007**, *43*, 4486.
(142) Culp, J. T.; Matranga, C.; Smith, M.; Bittner, E. W.; Bockrath, B. *J. Phys. Chem. B* **2006**, *110*, 8325.
(143) Culp, J. T.; Natesakhawat, S.; Smith, M. R.; Bittner, E.; Matranga, C.; Bockrath, B. *J. Phys. Chem. C* **2008**, *112*, 7079.
(144) Kaye, S. S.; Long, J. R. *J. Am. Chem. Soc.* **2005**, *127*, 6506.
(145) Kaye, S. S.; Long, J. R. *Catal. Today* **2007**, *120*, 311.
(146) Reguera, L.; Balmaseda, J.; Krap, C. P.; Avila, M.; Reguera, E. *J. Phys. Chem. C* **2008**, *112*, 17443.
(147) Chapman, K. W.; Southon, P. D.; Weeks, C. L.; Kepert, C. J. *Chem. Commun.* **2005**, *41*, 3322.
(148) Mulfort, K. L.; Farha, O. K.; Stern, C. L.; Sarjeant, A. A.; Hupp, J. T. *J. Am. Chem. Soc.* **2009**, *131*, 3866.
(149) Nouar, F.; Eckert, J.; Eubank, J. F.; Forster, P.; Eddaoudi, M. *J. Am. Chem. Soc.* **2009**, *131*, 2864.
(150) Wang, Z.; Tanabe, K. K.; Cohen, S. M. *Chem.—Eur. J.* **2010**, *16*, 212.
(151) Mulfort, K. L.; Hupp, J. T. *J. Am. Chem. Soc.* **2007**, *129*, 9604.
(152) Zlotea, C.; Campesi, R.; Cuevas, F.; Leroy, E.; Dibandjo, P.; Volkringer, C.; Loiseau, T.; Férey, G.; Latroche, M. *J. Am. Chem. Soc.* **2010**, *132*, 2991.
(153) Hoskins, B. F.; Robson, R. *J. Am. Chem. Soc.* **1990**, *112*, 1546.
(154) Wang, Z.; Cohen, S. M. *J. Am. Chem. Soc.* **2007**, *129*, 12368.
(155) Wang, Z.; Cohen, S. M. *Chem. Soc. Rev.* **2009**, *38*, 1315.
(156) Tanabe, K. K.; Cohen, S. M. *Chem. Soc. Rev.* **2011**, *40*, 498.
(157) Hwang, Y. K.; Hong, D.-Y.; Chang, J.-S.; Jhung, S. H.; Seo, Y.-K.; Kim, J.; Vimont, A.; Daturi, M.; Serre, C.; Férey, G. *Angew. Chem., Int. Ed.* **2008**, *47*, 4144.
(158) Meilikhov, M.; Yusenko, K.; Esken, D.; Turner, S.; Tendeloo, G. V.; Fischer, R. A. *Eur. J. Inorg. Chem.* **2010**, 3701.
(159) Farha, O. K.; Mulfort, K. L.; Hupp, J. T. *Inorg. Chem.* **2008**, *47*, 10223.
(160) Costa, J. S.; Gamez, P.; Black, C. A.; Roubeau, O.; Teat, S. J.; Reedijk *Eur. J. Inorg. Chem.* **2008**, 1551.
(161) Kawamichi, T.; Kodama, T.; Kawano, M.; Fujita, M. *Angew. Chem., Int. Ed.* **2008**, *47*, 8030.
(162) Ingleson, M. J.; Barrio, J. P.; Guilbaud, J.-B.; Khimyak, Y. Z.; Rosseinsky, M. J. *Chem. Commun.* **2008**, *44*, 2680.
(163) Morris, W.; Doonan, C. J.; Furukawa, H.; Banerjee, R.; Yaghi, O. M. *J. Am. Chem. Soc.* **2008**, *130*, 12626.
(164) Burrows, A.; Frost, C.; Mahon, M.; Richardson, C. *Angew. Chem., Int. Ed.* **2008**, *47*, 8482.
(165) Jones, S. C.; Bauer, C. A. *J. Am. Chem. Soc.* **2009**, *131*, 12516.
(166) Goto, Y.; Sato, H.; Shinkai, S.; Sada, K. *J. Am. Chem. Soc.* **2008**, *130*, 14354.
(167) Gadzikwa, T.; Farha, O. K.; Malliakas, C. D.; Kanatzidis, M. G.; Hupp, J. T.; Nguyen, S. T. *J. Am. Chem. Soc.* **2009**, *131*, 13613.
(168) Cheon, Y. E.; Suh, M. P. *Chem. Commun.* **2009**, *45*, 2296.
(169) Lochan, R. C.; Head-Gordon, M. *Phys. Chem. Chem. Phys.* **2006**, *8*, 1357.
(170) Bhatia, S. K.; Myers, A. L. *Langmuir* **2006**, *22*, 1688.
(171) Frost, H.; Duren, T.; Snurr, R. Q. *J. Phys. Chem. B* **2006**, *110*, 9565.
(172) Frost, H.; Snurr, R. Q. *J. Phys. Chem. C* **2007**, *111*, 18794.
(173) Park, H. J.; Lim, D.-W.; Yang, W. S.; Oh, T.-R.; Suh, M. P. *Chem.—Eur. J.* **2011**, *17*, 7251.
(174) Sumida, K.; Hill, M. R.; Horike, S.; Dailly, A.; Long, J. R. *J. Am. Chem. Soc.* **2009**, *131*, 15120.
(175) Rood, J. A.; Noll, B. C.; Henderson, K. W. *Inorg. Chem.* **2006**, *45*, 5521.
(176) Férey, G.; Latroche, M.; Serre, C.; Millange, F.; Loiseau, T.; Percheron-Guegan, A. *Chem. Commun.* **2003**, *24*, 2976.
(177) Loiseau, T.; Lecroq, L.; Volkringer, C.; Marrot, J.; Férey, G.; Haouas, M.; Taulelle, F.; Bourrelly, S.; Llewellyn, P. L.; Latroche, M. *J. Am. Chem. Soc.* **2006**, *128*, 10223.
(178) Perles, J.; Iglesias, M.; Martín-Luengo, M.-Á.; Monge, M. Á.; Ruiz-Valero, C.; Snejko, N. *Chem. Mater.* **2005**, *17*, 5837.
(179) Ibarra, I. A.; Yang, S.; Lin, X.; Blake, A. J.; Rizkallah, P. J.; Nowell, H.; Allan, D. R.; Champness, N. R.; Hubberstey, P. *Chem. Commun.* **2011**, *47*, 8304.
(180) Dybtsev, D. N.; Chun, H.; Yoon, S. H.; Kim, D.; Kim, K. *J. Am. Chem. Soc.* **2004**, *126*, 32.
(181) Jia, J.; Lin, X.; Wilson, C.; Blake, A. J.; Champness, N. R.; Hubberstey, P.; Walker, G.; Cussen, E. J.; Schröder, M. *Chem. Commun.* **2007**, *43*, 840.
(182) Chen, B.; Ma, S.; Hurtado, E. J.; Lobkovsky, E. B.; Liang, C.; Zhu, H.; Dai, S. *Inorg. Chem.* **2007**, *46*, 8705.
(183) Lee, J. Y.; Li, J.; Jagiello, J. *J. Solid State Chem.* **2005**, *178*, 2527.
(184) Humphrey, S. M.; Chang, J.-S.; Jhung, S. H.; Yoon, J. W.; Wood, P. T. *Angew. Chem., Int. Ed.* **2007**, *46*, 272.
(185) Zhu, L.-G.; Xiao, H.-P. *Z. Anorg. Allg. Chem.* **2008**, *634*, 845.
(186) Takei, T.; Kawashima, J.; Ii, T.; Maeda, A.; Hasegawa, M.; Kitagawa, T.; Ohmura, T.; Ichikawa, M.; Hosoe, M.; Kanoya, I. *Bull. Chem. Soc. Jpn.* **2008**, *81*, 847.
(187) Chun, H.; Jung, H.; Koo, G.; Jeong, H.; Kim, D.-K. *Inorg. Chem.* **2008**, *47*, 5355.
(188) Lee, J. Y.; Pan, L.; Kelly, S. P.; Jagiello, J.; Emge, T. J.; Li, J. *Adv. Mater.* **2005**, *17*, 2703.
(189) Chang, Z.; Zhang, D.-S.; Hu, T.-L.; Bu, X.-H. *Cryst. Growth Des.* **2011**, *11*, 2050.
(190) Jiang, G.; Wu, T.; Zheng, S.-T.; Zhao, X.; Lin, Q.; Bu, X.; Feng, P. *Cryst. Growth Des.* **2011**, *11*, 3713.
(191) Ma, S.; Wang, X.-S.; Manis, E. S.; Collier, C. D.; Zhou, H.-C. *Inorg. Chem.* **2007**, *46*, 3432.
(192) Noguchi, D.; Tanaka, H.; Kondo, A.; Kajiro, H.; Noguchi, H.; Ohba, T.; Kanoh, H.; Kaneko, K. *J. Am. Chem. Soc.* **2008**, *130*, 6367.
(193) Yang, W.; Lin, X.; Jia, J.; Blake, A. J.; Wilson, C.; Hubberstey, P.; Champness, N. R.; Schröder, M. *Chem. Commun.* **2008**, *44*, 359.
(194) Chen, B.; Ma, S.; Zapata, F.; Fronczek, F. R.; Lobkovsky, E. B.; Zhou, H.-C. *Inorg. Chem.* **2007**, *46*, 1233.
(195) Navarro, J. A. R.; Barea, E.; Salas, J. M.; Masciocchi, N.; Galli, S.; Sironi, A.; Ania, C. O.; Parra, J. B. *Inorg. Chem.* **2006**, *45*, 2397.
(196) Navarro, J. A. R.; Barea, E.; Rodríguez-Diéguez, A.; Salas, J. M.; Ania, C. O.; Parra, J. B.; Masciocchi, N.; Galli, S.; Sironi, A. *J. Am. Chem. Soc.* **2008**, *130*, 3978.

(197) Pan, L.; Sander, M. B.; Huang, X.; Li, J.; Smith, M.; Bittner, E.; Bockrath, B.; Johnson, J. K. *J. Am. Chem. Soc.* **2004**, *126*, 1308.
(198) Lee, J. Y.; Olson, D. H.; Pan, L.; Emge, T. J.; Li, J. *Adv. Funct. Mater.* **2007**, *17*, 1255.
(199) Zhou, W.; Wu, H.; Hartman, M. R.; Yildirim, T. *J. Phys. Chem. C* **2007**, *111*, 16131.
(200) Chen, B.; Ma, S.; Zapata, F.; Lobkovsky, E. B.; Yang, J. *Inorg. Chem.* **2006**, *45*, 5718.
(201) Pan, L.; Parker, B.; Huang, X.; Olson, D. H.; Lee, J. Y.; Li, J. *J. Am. Chem. Soc.* **2006**, *128*, 4180.
(202) Krawiec, P.; Kramer, M.; Sabo, M.; Kunschke, R.; Fröde, H.; Kaskel, S. *Adv. Eng. Mater.* **2006**, *8*, 293.
(203) Hulvey, Z.; Sava, D. A.; Eckert, J.; Cheetham, A. K. *Inorg. Chem.* **2011**, *50*, 403.
(204) Lin, X.; Blake, A. J.; Wilson, C.; Sun, X. Z.; Champness, N. R.; George, M. W.; Hubberstey, P.; Mokaya, R.; Schröder, M. *J. Am. Chem. Soc.* **2006**, *128*, 10745.
(205) Xue, M.; Ma, S.; Jin, Z.; Schaffino, R. M.; Zhu, G.-Z.; Lobkovsky, E. B.; Qiu, S.-L.; Chen, B. *Inorg. Chem.* **2008**, *47*, 6825.
(206) Ma, L.; Lee, J. Y.; Li, J.; Lin, W. *Inorg. Chem.* **2008**, *47*, 3955.
(207) Sun, D.; Ke, Y.; Collins, D. J.; Lorigan, G. A.; Zhou, H.-C. *Inorg. Chem.* **2007**, *46*, 2725.
(208) Ma, S.; Wang, X.-S.; Collier, C. D.; Manis, E. S.; Zhou, H.-C. *Inorg. Chem.* **2007**, *46*, 8499.
(209) Barman, S.; Furukawa, H.; Blacque, O.; Venkatesan, K.; Yaghi, O. M.; Berke, H. *Chem. Commun.* **2010**, *46*, 7981.
(210) Panella, B.; Hirscher, M.; Pütter, H.; Müller, U. *Adv. Funct. Mater.* **2006**, *16*, 520.
(211) Panella, B.; Hirscher, M. *Adv. Mater.* **2005**, *17*, 538.
(212) Sabo, M.; Henschel, A.; Fröde, H.; Klemm, E.; Kaskel, S. *J. Mater. Chem.* **2007**, *17*, 3827.
(213) Dailly, A.; Vajo, J. J.; Ahn, C. C. *J. Phys. Chem. B* **2006**, *110*, 1099.
(214) Kim, H.; Das, S.; Kim, M. G.; Dybtsev, D. N.; Kim, Y.; Kim, K. *Inorg. Chem.* **2011**, *50*, 3691.
(215) Sun, D.; Collins, D. J.; Ke, Y.; Zuo, J.-L.; Zhou, H.-C. *Chem.—Eur. J.* **2006**, *12*, 3768.
(216) Kesanli, B.; Cui, Y.; Smith, M. R.; Bittner, E. W.; Bockrath, B. C.; Lin, W. *Angew. Chem., Int. Ed.* **2005**, *44*, 72.
(217) Park, H.; Britten, J. F.; Mueller, U.; Lee, J. Y.; Li, J.; Parise, J. B. *Chem. Mater.* **2007**, *19*, 1302.
(218) Han, D.; Jiang, F.-L.; Wu, M.-Y.; Chen, L.; Chen, Q.-X.; Hong, M.-C. *Chem. Commun.* **2011**, *47*, 9861.
(219) Fang, Q.-R.; Zhu, G.-S.; Xue, M.; Zhang, Q.-L.; Sun, J.-Y.; Guo, X.-D.; Qiu, S.-L.; Xu, S.-T.; Wang, P.; Wang, D.-J.; Wei, Y. *Chem.—Eur. J.* **2006**, *12*, 3754.
(220) Navarro, J. A. R.; Barea, E.; Salas, J. M.; Masciocchi, N.; Sironi, S.; Galli, A.; Ania, C. O.; Parra, J. B. *J. Mater. Chem.* **2007**, *17*, 1939.
(221) Yang, C.; Wang, X.; Omary, M. A. *J. Am. Chem. Soc.* **2007**, *129*, 15454.
(222) Fang, Q.-R.; Zhu, G.-S.; Jin, Z.; Ji, Y.-Y.; Ye, J.-W.; Xue, M.; Yang, H.; Wang, Y.; Qiu, S.-L. *Angew. Chem., Int. Ed.* **2007**, *46*, 6638.
(223) Sava, D. F.; Kravtsov, V. C.; Nouar, F.; Wojtas, L.; Eubank, J. F.; Eddaoudi, M. *J. Am. Chem. Soc.* **2008**, *130*, 3768.
(224) Gu, X.; Lu, Z.-H.; Xu, Q. *Chem. Commun.* **2010**, *46*, 7400.
(225) Zheng, S.-T.; Bu, J. J.; Wu, T.; Chou, C.; Feng, P.; Bu, X. *Angew. Chem., Int. Ed.* **2011**, *50*, 8858.
(226) Ma, S.; Wang, X.-S.; Yuan, D.; Zhou, H.-C. *Angew. Chem., Int. Ed.* **2008**, *47*, 4130.
(227) Sumida, K.; Brown, C. M.; Herm, Z. R.; Chavan, S.; Bordiga, S.; Long, J. R. *Chem. Commun.* **2011**, *47*, 1157.
(228) Moon, H. R.; Kobayashi, N.; Suh, M. P. *Inorg. Chem.* **2006**, *45*, 8672.
(229) Yoon, J. H.; Choi, S. B.; Oh, Y. J.; Seo, M. J.; Jhon, Y. H.; Lee, T.-B.; Kim, D.; Choi, S.-H.; Kim, J. *Catal. Today* **2007**, *120*, 324.
(230) Forster, P. M.; Eckert, J.; Heiken, B. D.; Parise, J. B.; Yoon, J. W.; Jhung, S. H.; Chang, J. S.; Cheetham, A. K. *J. Am. Chem. Soc.* **2006**, *128*, 16846.
(231) Dietzel, P. D. C.; Panella, B.; Hirscher, M.; Blom, R.; Fjellvåg, H. *Chem. Commun.* **2006**, *42*, 959.
(232) Liu, X.; Oh, M.; Lah, M. S. *Inorg. Chem.* **2011**, *50*, 5044.
(233) Liu, X.; Oh, M.; Lah, M. S. *Cryst. Growth Des.* 2011, *11*, 5064–5071.
(234) Liu, Y.; Kabbour, H.; Brown, C. M.; Neumann, D. A.; Ahn, C. C. *Langmuir* **2008**, *24*, 4772.
(235) Chen, B.; Zhao, X.; Putkham, A.; Hong, K.; Lobkovsky, E. B.; Hurtado, E. J.; Fletcher, A. J.; Thomas, K. M. *J. Am. Chem. Soc.* **2008**, *130*, 6411.
(236) Farha, O. K.; Spokoyny, A. M.; Mulfort, K. L.; Hawthorne, M. F.; Mirkin, C. A.; Hupp, J. T. *J. Am. Chem. Soc.* **2007**, *129*, 12680.
(237) Jia, J.; Lin, X.; Blake, A. J.; Champness, N. R.; Hubberstey, P.; Shao, L.; Walker, G. S.; Wilson, C.; Schröder, M. *Inorg. Chem.* **2006**, *45*, 8838.
(238) Sumida, K.; Her, J.-H.; Dincă, M.; Murray, L. J.; Schloss, J. M.; Pierce, C. J.; Thompson, B. A.; FitzGerald, S. A.; Brown, C. M.; Long, J. R. *J. Phys. Chem. C* **2011**, *115*, 8414.
(239) Surblé, S.; Millange, F.; Serre, C.; Düren, T.; Latroche, M.; Bourrelly, S.; Llewellyn, P. L.; Férey, G. *J. Am. Chem. Soc.* **2006**, *128*, 14889.
(240) Choi, S. B.; Seo, M. J.; Cho, M.; Kim, Y.; Jin, M. K.; Jung, D.-Y.; Choi, J.-S.; Ahn, W.-S.; Rowsell, J. L. C.; Kim, J. *Cryst. Growth Des.* **2007**, *7*, 2290.
(241) Sun, D.; Ma, S.; Ke, Y.; Collins, D. J.; Zhou, H.-C. *J. Am. Chem. Soc.* **2006**, *128*, 3896.
(242) Ma, S.; Eckert, J.; Forster, P. M.; Yoon, J. W.; Hwang, Y. K.; Chang, J.-S.; Collier, C. D.; Parise, J. B.; Zhou, H.-C. *J. Am. Chem. Soc.* **2008**, *130*, 15896.
(243) Zhou, H.-C.; Ma, S. Q.; Sun, D. F.; Ambrogio, M.; Fillinger, J. A.; Parkin, S. *J. Am. Chem. Soc.* **2007**, *129*, 1858.
(244) Wong-Foy, A. G.; Lebel, O.; Matzger, A. J. *J. Am. Chem. Soc.* **2007**, *129*, 15740.
(245) Luo, J.; Xu, H.; Liu, Y.; Zhao, Y.; Daemen, L. L.; Brown, C.; Timofeeva, T. V.; Ma, S.; Zhou, H.-C. *J. Am. Chem. Soc.* **2008**, *130*, 9626.
(246) Kramer, M.; Schwarz, U.; Kaskel, S. *J. Mater. Chem.* **2006**, *16*, 2245.
(247) Guo, X.; Zhu, G.; Li, Z.; Sun, F.; Yang, Z.; Qiu, S. *Chem. Commun.* **2006**, *42*, 3172.
(248) Zhang, P.; Li, B.; Zhao, Y.; Meng, X.; Zhang, T. *Chem. Commun.* **2011**, *47*, 7722.
(249) Chen, B.; Ockwig, N. W.; Millward, A. R.; Contreras, D. S.; Yaghi, O. M. *Angew. Chem., Int. Ed.* **2005**, *44*, 4745.
(250) Lin, X.; Jia, J.; Zhao, X.; Thomas, K. M.; Blake, A. J.; Walker, G. S.; Champness, N. R.; Hubberstey, P.; Schröder, M. *Angew. Chem., Int. Ed.* **2006**, *45*, 7358.
(251) Yang, S. H.; Lin, X.; Dailly, A.; Blake, A. J.; Hubberstey, P.; Champness, N. R.; Schröder, M. *Chem.—Eur. J.* **2009**, *15*, 4829.
(252) Wang, X. S.; Ma, S. Q.; Rauch, K.; Simmons, J. M.; Yuan, D. Q.; Wang, X. P.; Yildirim, T.; Cole, W. C.; Lopez, J. J.; de Meijere, A.; Zhou, H.-C. *Chem. Mater.* **2008**, *20*, 3145.
(253) Wang, X.-S.; Ma, S.; Forster, P. M.; Yuan, D.; Eckert, J.; López, J. L.; Murphy, B. J.; Parise, J. B.; Zhou, H.-C. *Angew. Chem., Int. Ed.* **2008**, *47*, 7263.
(254) Ma, S.; Simmons, J. M.; Sun, D.; Yuan, D.; Zhou, H. −C. *Inorg. Chem.* **2009**, *48*, 5263.
(255) Sun, D.; Ma, S.; Simmons, J. M.; Li, J.-R.; Yuan, D.; Zhou, H.-C. *Chem. Commun.* **2010**, *46*, 1329.
(256) Zhuang, W.; Ma, S.; Wang, X.-S.; Yuan, D.; Li, J.-R.; Zhao, D.; Zhou, H.-C. *Chem. Commun.* **2010**, *46*, 5223.
(257) Zhao, D.; Yuan, D.; Yakovenko, A.; Zhou, H.-C. *Chem. Commun.* **2010**, *46*, 4196.
(258) Xue, M.; Zhu, G.; Li, Y.; Zhao, X.; Jin, Z.; Kang, E.; Qiz, S. *Cryst. Growth Des.* **2008**, *8*, 2478.
(259) Kim, T. K.; Suh, M. P. *Chem. Commun.* **2011**, *47*, 4258.
(260) Prasad, T. K.; Hong, D. H.; Suh, M. P. *Chem.—Eur. J.* **2010**, *16*, 14043.
(261) Zheng, B.; Liang, Z.; Li, G.; HuO, Q.; Liu, Y. *Cryst. Growth Des.* **2010**, *10*, 3405.

(262) Sun, D.; Ke, Y.; Mattox, T. M.; Ooro, B. A.; Zhou, H.-C. *Chem. Commun.* **2005**, *41*, 5447.
(263) Yan, Y.; Blake, A. J.; Lewis, W.; Barnett, S. A.; Dailly, A.; Champness, N. R.; Schröder, M. *Chem.—Eur. J.* **2011**, *17*, 11162.
(264) Guo, Z.; Wu, H.; Srinivas, G.; Zhou, Y.; Xiang, S.; Chen, Z.; Yang, Y.; Zhou, W.; O'Keeffe, M.; Chen, B. *Angew. Chem., Int. Ed.* **2011**, *50*, 3178.
(265) Yuan, D.; Zhao, D.; Sun, D.; Zhou, H.-C. *Angew. Chem., Int. Ed.* **2010**, *49*, 5357.
(266) Yan, Y.; Yang, S.; Blake, A. J.; Lewis, W.; Poirier, E.; Barnett, S. A.; Champness, N. R.; Schröder, M. *Chem. Commun.* **2011**, *47*, 9995.
(267) Yuan, D.; Zhao, D.; Zhou, H.-C. *Inorg. Chem.* 2011, *50*, 10528–10530.
(268) Yan, Y.; Lin, X.; Yang, S.; Blake, A. J.; Dailly, A.; Champness, N. R.; Hubberstey, P.; Schröder, M. *Chem. Commun.* **2009**, *45*, 1025.
(269) Hong, S.; Oh, M.; Park, M.; Yoon, J. W.; Chang, J. −S.; Lah, M. S. *Chem. Commun.* **2009**, *45*, 5397.
(270) Tan, C.; Yang, S.; Champness, N. R.; Lin, X.; Blake, A. J.; Lewis, W.; Schröder, M. *Chem. Commun.* **2011**, *47*, 4487.
(271) Sumida, K.; Horike, S.; Kaye, S. S.; Herm, Z. R.; Queen, W. L.; Brown, C. M.; Grandjean, F.; Long, G. J.; Anne, D.; Long, J. R. *Chem. Sci.* **2010**, *1*, 184.
(272) Dincă, M.; Long, J. R. *Chem.—Eur. J.* **2008**, *14*, 10280.
(273) Dincă, M.; Han, W. S.; Liu, Y.; Dailly, A.; Brown, C. M.; Long, J. R. *Angew. Chem., Int. Ed.* **2007**, *46*, 1419.
(274) Denysenko, D.; Grzywa, M.; Tonigold, M.; Streppel, B.; Krkljus, I.; Hirscher, M.; Mugnaioli, E.; Kolb, U.; Hanss, J.; Volkmer, D. *Chem. Eur. J.* **2011**, *17*, 1837.
(275) Yan, Y.; Telepeni, I.; Yang, S.; Lin, X.; Kockelmann, W.; Dailly, A.; Blake, A. J.; Lewis, W.; Walker, G. S.; Allan, D. R.; Barnett, S. A.; Champness, N. R.; Schröder, M. *J. Am. Chem. Soc.* **2010**, *132*, 4092.
(276) Zhao, D.; Yuan, D. Q.; Sun, D. F.; Zhou, H. C. *J. Am. Chem. Soc.* **2009**, *131*, 9186.
(277) *Metal-Organic Frameworks: Design and Application*; MacGillivray, L. R., Ed.; Wiley: Hoboken, NJ, 2010.
(278) Rosi, N. L.; Eddaoudi, M.; Kim, J.; O'Keeffe, M.; Yaghi, O. M. *Angew. Chem., Int. Ed.* **2002**, *41*, 294.
(279) Batten, S. R. *CrystEngComm* **2001**, *3*, 67.
(280) Batten, S. R.; Robson, R. *Angew. Chem., Int. Ed.* **1998**, *37*, 1460.
(281) Farha, O. K.; Malliakas, C. D.; Kanatzidis, M. G.; Hupp, J. T. *J. Am. Chem. Soc.* **2010**, *132*, 950.
(282) Zhang, J.; Wojtas, L.; Larsen, R. W.; Eddaoudi, M.; Zaworotko, M. J. *J. Am. Chem. Soc.* **2009**, *131*, 17040.
(283) Shekhah, O.; Wang, H.; Paradinas, M.; Ocal, C.; Schupbach, B.; Terfort, A.; Zacher, D.; Fischer, R. A.; Woll, C. *Nat. Mater.* **2009**, *8*, 481.
(284) Rowsell, J. L.; Yaghi, O. M. *Angew. Chem., Int. Ed.* **2005**, *44*, 4670.
(285) Kanoo, P.; Matsuda, R.; Higuchi, M.; Kitagawa, S.; Maji, T. K. *Chem. Mater.* **2009**, *21*, 5860.
(286) Ryan, P.; Broadbelt, L. J.; Snurr, R. Q. *Chem. Commun.* **2008**, *44*, 4132.
(287) Bae, Y.-S.; Snurr, R. Q. *Microporous Mesoporous Mater.* **2010**, *132*, 300.
(288) Peterson, V. K.; Liu, Y.; Brown, C. M.; Kepert, C. J. *J. Am. Chem. Soc.* **2006**, *128*, 15578.
(289) Xiao, B.; Wheatley, P. S.; Zhao, X.; Fletcher, A. J.; Fox, S.; Rossi, A. G.; Megson, I. L.; Bordiga, S.; Regli, L.; Thomas, K. M.; Morris, R. E. *J. Am. Chem. Soc.* **2007**, *129*, 1203.
(290) S.; Deng, W.-Q.; Goddard, W. A. *Angew. Chem., Int. Ed.* **2007**, *46*, 6289.
(291) Dincă, M.; Long, J. R. *J. Am. Chem. Soc.* **2005**, *127*, 9376.
(292) Liu, Y.; Kravtsov, V. C.; Larsen, R.; Eddaoudi, M. *Chem. Commun.* **2006**, *42*, 1488.
(293) Mulfort, K. L.; Hupp, J. T. *Inorg. Chem.* **2008**, *47*, 7936.
(294) Mulfort, K. L.; Wilson, T. M.; Wasielewski, M. R.; Hupp, J. T. *Langmuir* **2009**, *25*, 503.
(295) Blomqvist, A.; Araffljo, C. M.; Srepusharawoot, P.; Ahuja, R. *Proc. Natl. Acad. Sci. U.S.A.* **2007**, *104*, 20173.
(296) Han, S. S.; Goddard, W. A. *J. Am. Chem. Soc.* **2007**, *129*, 8422.
(297) Han, S. S.; Goddard, W. A. *J. Phys. Chem. C* **2008**, *112*, 13431.
(298) Han, S. S.; Choi, S.-H.; Goddard, W. A. *J. Phys. Chem. C* **2011**, *115*, 3507.
(299) Mavrandonakis, A.; Klopper, W. *J. Phys. Chem. C* **2008**, *112*, 11580.
(300) Dalach, P.; Frost, H.; Snurr, R. Q.; Ellis, D. E. *J. Phys. Chem. C* **2008**, *112*, 9278.
(301) Mavrandonakis, A.; Tylianakis, E.; Stubos, A. K.; Froudakis, G. E. *J. Phys. Chem. C* **2008**, *112*, 7290.
(302) Huang, B.; Lee, H.; Duan, W.; Ihm, J. *Appl. Phys. Lett.* **2008**, *93*, 63107.
(303) Choi, Y. J.; Lee, J. W.; Choi, J. H.; Kang, J. K. *Appl. Phys. Lett.* **2008**, *92*, 173102.
(304) Himsl, D.; Wallacher, D.; Hartmann, M. *Angew. Chem., Int. Ed.* **2009**, *48*, 4639.
(305) Klontzas, E.; Mavrandonakis, A.; Tylianakis, E.; Froudakis, G. E. *Nano Lett.* **2008**, *8*, 1572.
(306) Botas, J. A.; Calleja, G.; Sánchez-Sánchez, M.; Orcajo, M. G. *Langmuir.* **2010**, *26*, 5300.
(307) Srinivas, S. T.; Rao, P. K. *J. Catal.* **1994**, *148*, 470.
(308) Li, Y.; Yang, R. T. *J. Am. Chem. Soc.* **2006**, *128*, 8136.
(309) Liu, Y.-Y.; Zeng, J.-L.; Zhang, J.; Xu, F.; Sun, L.-X. *Int. J. Hydrogen. Energy.* **2007**, *32*, 4005.
(310) Wang, L.; Stuckert, N. R.; Chen, H.; Yang, R. T. *J. Phys. Chem. C* **2011**, *115*, 4793.
(311) Proch, S.; Herrmannsdofer, J.; Kempe, R.; Kern, C.; Jess, A.; Seyfarth, L.; Senker, J. *Chem.—Eur. J.* **2008**, *14*, 8204.
(312) Liu, Y. Y.; Zhang, J.; Zeng, J. L.; Chu, H. L.; Xu, F.; Sun, L. X. *Chin. J. Catal.* **2008**, *29*, 655.
(313) Kosal, M. E.; Chou, J.-H.; Wilson, S. R.; Suslick, K. S. *Nat. Mater.* **2002**, *1*, 118.
(314) Zimmer, B.; Hutin, M.; Bulach, V.; Hosseini, M. W.; Cian, A. D.; Kyritsakas, N. *New. J. Chem.* **2002**, *26*, 1532.
(315) Deiters, E.; Bulach, V.; Hosseini, M. W. *Chem. Commun.* **2005**, 3906.
(316) Kuhn, E.; Bulach, V.; Hosseini, M. W. *Chem. Commun.* **2008**, 5104.
(317) Ohmura, T.; Usuki, A.; Fukumori, K.; Ohta, T.; Ito, M.; Tatsumi, K. *Inorg. Chem.* **2006**, *45*, 7988.
(318) Alkordi, M. H.; Liu, Y. L.; Larsen, R. W.; Eubank, J. F.; Eddaoudi, M. *J. Am. Chem. Soc.* **2008**, *130*, 12639.
(319) Chen, L.; Yang, Y.; Jiang, D. L. *J. Am. Chem. Soc.* **2010**, *132*, 9138.
(320) Farha, O. K.; Shultz, A. M.; Sarjeant, A. A.; Nguyen, S. T.; Hupp, J. T. *J. Am. Chem. Soc.* **2011**, *133*, 5652.
(321) Song, F.; Wang, C.; Falkowski, J. M.; Ma, L.; Lin, W. *J. Am. Chem. Soc.* **2010**, *132*, 15390.
(322) Kitaura, R.; Onoyama, G.; Sakamoto, H.; Matsuda, R.; Noro, S.; Kitagawa, S. *Angew. Chem., Int. Ed.* **2004**, *43*, 2684.
(323) Wu, H.-B.; Wang, Q.-M. *Angew. Chem., Int. Ed.* **2009**, *48*, 7343.
(324) Sakamoto, H.; Matsuda, R.; Bureekaew, S.; Tanaka, D.; Kitagawa, S. *Chem.—Eur. J.* **2009**, *15*, 4985.
(325) Roesky, P. W.; Bhunia, A.; Lan, Y.; Powell, A. K.; Kureti, S. *Chem. Commun.* **2011**, *47*, 2035.
(326) Shultz, A. M.; Farha, O. K.; Adhikari, D.; Sarjeant, A. A.; Hupp, J. T.; Nguyen, S. T. *Inorg. Chem.* **2011**, *50*, 3174.
(327) Shultz, A. M.; Sarjeant, A. A.; Farha, O. K.; Hupp, J. T.; Nguyen, S. T. *J. Am. Chem. Soc.* **2011**, *133*, 13252.
(328) Wu, C.-D.; Hu, A.; Zhang, L.; Lin, W. *J. Am. Chem. Soc.* **2005**, *127*, 8940.
(329) Oisaki, K.; Li, Q.; Furukawa, H.; Czaja, A. U.; Yaghi, O. M. *J. Am. Chem. Soc.* **2010**, *132*, 9262.
(330) Bloch, E. D.; Britt, D.; Lee, C.; Doonan, C.; Uribe-Romo, F. J.; Furukawa, H.; Long, J. R.; Yaghi, O. M. *J. Am. Chem. Soc.* **2010**, *132*, 14382.

(331) Gadzikwa, T.; Farha, O. K.; Mulfort, K. L.; Hupp, J. T.; Nguyen, S. T. *Chem. Commun.* **2009**, *45*, 3720.
(332) Doonan, C. J.; Morris, W.; Furukawa, H.; Yaghi, O. M. *J. Am. Chem. Soc.* **2009**, *131*, 9492.
(333) Everett, D. H.; Powl, J. C. *J. Chem. Soc., Faraday Trans.* **1976**, *72*, 619.
(334) Zhao, D.; Yan, D.; Zhou, H.-C. *Energy Environ. Sci.* **2008**, *1*, 225.
(335) Hubner, O.; Gloss, A.; Fichtner, M.; Klopper, W. *J. Phys. Chem. A* **2004**, *108*, 3019.
(336) Li, Y.; Yang, R. T. *Langmuir* **2007**, *23*, 12937.
(337) Millange, F.; Serre, C.; Guillou, N.; Férey, G.; Walton, R. I. *Angew. Chem., Int. Ed.* **2008**, *47*, 4100.
(338) Dybtsev, D. N.; Yutkin, M. P.; Samsonenko, D. G.; Fedin, V. P.; Nuzhdin, A. L.; Bezrukov, A. A.; Bryliakov, K. P.; Talsi, E. P.; Belosludov, R. V.; Mizuseki, H.; Kawazoe, Y.; Subbotin, O. S.; Belosludov, V. R. *Chem.—Eur. J.* **2010**, *16*, 10348.
(339) Nelson, A. P.; Farha, O. K.; Mulfort, K. L.; Hupp, J. T. *J. Am. Chem. Soc.* **2009**, *131*, 458.
(340) Ma, L.; Jin, A.; Xie, Z.; Lin, W. *Angew. Chem., Int. Ed.* **2009**, *48*, 9905.
(341) Broom, D. P. *Int. J. Hydrogen Energy* **2007**, *32*, 4871.
(342) Belmabkhout, Y.; Frere, M.; Weireld, G. D. *Meas. Sci. Technol.* **2004**, *15*, 848.
(343) Yildirim, T.; Hartman, M. R. *Phys. Rev. Lett.* **2005**, *95*, 215504.
(344) Mulder, F. M.; Assfour, B.; Huot, J.; Dingemans, T. J.; Wagemaker, M.; Ramirez-Cuesta, A. J. *J. Phys. Chem. C* **2010**, *114*, 10648.
(345) Wu, H.; Zhou, W.; Yildirm, T. *J. Am. Chem. Soc.* **2007**, *129*, 5314.
(346) Roswell, J. L. C.; Eckert, J.; Yaghi, O. M. *J. Am. Chem. Soc.* **2005**, *127*, 14904.
(347) Bordiga, S.; Vitillo, J.; Ricchiardi, G.; Regli, L.; Cocina, D.; Zecchina, A.; Arstad, B.; Bjorgen, M.; Hafizovic, J.; Lillerud, K. P. *J. Phys. Chem. B* **2005**, *109*, 18237.
(348) Bordiga, S.; Regli, L.; Bonino, F.; Groppo, E.; Lamberti, C.; Xiao, B.; Wheatley, P. S.; Morris, R. E.; Zecchina., A. *Phys. Chem. Chem. Phys.* **2007**, *9*, 2676.
(349) Nijem, N.; Veyan, J.-F.; Kong, L.; Li, K.; Pramanik, S.; Zhao, Y.; Li, J.; Langreth, D.; Chabal, Y. J. *J. Am. Chem. Soc.* **2010**, *132*, 1654.
(350) Sun, Y. Y.; Kim, Y. H.; Zhang, S. B. *J. Am. Chem. Soc.* **2007**, *129*, 12606.
(351) Vitillo, J. G.; Regli, L.; Chavan, S.; Ricchiardi, G.; Spoto, G.; Dietzel, P. D. C.; Bordiga, S.; Zecchina, A. *J. Am. Chem. Soc.* **2008**, *130*, 8386.
(352) Kang, I. J.; Khan, N. A.; Haque, E.; Jhung, S. H. *Chem. Eur. J.* **2011**, *17*, 6437.
(353) Ma, D.; Li, Y.; Li, Z. *Chem. Commun.* **2011**, *47*, 7377.
(354) Wu, T.; Shen, L.; Luebbers, M.; Hu, C.; Chen, Q.; Ni, Z.; Masel, R. I. *Chem. Commun.* **2010**, *46*, 6120.
(355) Nguyen, J. G.; Cohen, S. M. *J. Am. Chem. Soc.* **2010**, *132*, 4560.